Type dependent retinal ganglion cell degeneration in glaucoma

Jingyi Gao

Beijing, China.

B.A., Vassar College, 2017

A Dissertation presented to the Graduate Faculty of the University of Virginia in Candidacy for the Degree of Doctor of Philosophy

Department of Biology

University of Virginia

July, 2022

Abstract

Glaucoma is a leading cause of blindness afflicting more than 70 million people worldwide. It is characterized by damage to RGCs that ultimately leads to the death of the cells and vision loss. The diversity of RGC subtypes has been appreciated for decades, and studies, including ours, have shown that RGCs degenerate and die in a type-specific manner in rodent models of glaucoma. The type-specific loss of RGCs results in differential damage to visual and non-visual functions. One type of RGC, the intrinsically photosensitive retinal ganglion cell (ipRGC), expressing the photopigment melanopsin, serves a broad array of non-visual responses to light. Since its discovery, six subtypes of ipRGCs have been described, each contributing to various image forming and non-image forming functions, such as circadian photoentrainment, the pupillary light reflex, the photic control of mood and sleep, and visual contrast sensitivity. The subtype-specific degeneration of ipRGCs and possible associated behavioral changes in animal models and glaucoma patients are reviewed in Chapter 1 of this thesis (to be submitted to *Frontiers in Cellular Neuroscience*).

Moreover, to examine the link between subtype-specific ipRGC survival and behavioral deficits in glaucoma, chronic ocular hypertension (OHT) was induced in mice by laser photocoagulation and survival of ipRGC subtypes was characterized. Specifically, I observed that ipRGC subtypes are differentially affected following chronic OHT. While M4 ipRGCs involved in pattern vision, are susceptible to chronic OHT. By contrast, M1 ipRGCs projecting to the suprachiasmatic nuclei (SCN) to regulate circadian rhythmicity, exhibit no cell loss. The cell loss of these subtypes correlates with behavioral observations: though mice with chronic OHT experience reduced contrast sensitivity and visual acuity, circadian re-entrainment and circadian rhythmicity are largely not disrupted in OHT mice. These findings are described in Chapter 2 (published in *Journal of Comparative Neurology*). These findings provide insight into glaucoma-induced visual behavioral deficits and their underlying mechanisms, which is useful for formulating

potential treatments of glaucoma.

Also important for glaucoma management is early intervention as glaucomatous damage is irreversible with the current treatments. Therefore, detecting RGC damages at the earliest stages is essential, though it continues to be a clinical challenge. Taking advantage of visible-light optical coherence tomography fibergraphy (vis-OCTF), we were able to non-invasively track early morphological changes of damaged RGC axon bundles in mice in vivo. Specifically, four parameters: lateral width, axial thickness, cross-sectional area, and the shape of individual bundles were characterized by vis-OCTF. And we found an early axon bundle swelling at 3-days post optic nerve crush, which correlated with about 15% RGC loss, and bundle thinning at 9-days post ONC that correlated with about 60% RGC loss. The morphological transformation of RGC axon bundles monitored by vis-OCTF could serve as a sensitive biomarker for RGC loss, which can be translated to clinical uses in the future. These findings are described in Chapter 3 of this thesis (to be submitted to *eLife*).

Current treatments for glaucoma include drugs and surgeries that alleviate the abnormally elevated IOP, which only slows down, but cannot stop or reverse disease progression, emphasizing the need to better understand glaucoma pathogenesis for future drug development. In Chapter 4 of this thesis, I provide a discussion on the pathogenesis of glaucoma. I propose that RGC loss in glaucoma can be viewed as two separate stages: An initial axonal damage caused by an imbalance of the translaminar pressure gradient (between intraocular pressure and the cerebrospinal fluid pressure). And a secondary soma degeneration caused by impeded trophic support and neuroinflammation. Moreover, I analyze how different RGC types may be differentially affected by various mechanisms contributing to RGC death in glaucoma. For example, the axon collaterals of M1 ipRGCs, may offer protection to these cells in glaucoma as these collaterals do not pass the optic nerve head region and therefore are spared from mechanical and metabolic damage with IOP elevation. Moreover, they may also provide extra target derived trophic support to M1 ipRGCs in glaucoma, etc. With the help of single cell omic technologies, the protective and detrimental molecular pathways underlying type dependent RGC damage can be characterized comprehensively, making the identification of high potential clinical targets possible.

Acknowledgement

I would first like to thank my supervisor, Dr. Xiaorong Liu, whose advice and expertise was invaluable to me at every stage of my PhD studies. She was always patient and encouraging when I needed suggestions, both on research and on life, especially during the tough time of pandemic. Lab parties at your house was always fun and relax. This thesis would not have been possible without you.

I would also like to thank my committee members. Dr. Ignacio Provencio, who conveyed an enthusiasm for science and gave me many great and detailed advice on various research projects and writings. Dr. Christopher Deppmann, who was always supportive and available for discussions. Dr. Eli Zunder, for his patient help on CyTOF when I embarked on my very first project. Dr. John Campbell, for his constructive discussions and support.

I am also very grateful to my colleagues in the Liu lab and Cang lab and collaborators in the biology department. I need to thank Mingna Liu, who was always reliable and ready to help when I came across problems with my experiments. Hui Chen, for help with all computer problems I encountered. Marta Grannonico, for help with experiments, useful discussions, as well as hugs when graduate life got a bit tougher than usual. Elise Savier, for patiently teaching me many experiments, giving constructive advice on research, and helping to organize all those hotpots/food parties that were highlights of many weekends. Kara McHaney, for help with experiments and animal keeping. Chuiwen Li, Yuanming Liu, and Chen Chen, for always ready to help with research and life and for cheering every small accomplishments I made. I also want to thank other lab members in the Liu and Cang lab, James Cole, Pedro Magno, Victor DePiero, Rolf Skyberg and Jenny Fu, for making the lab such a supportive and friendly space.

I would also like to thank my flute teacher Dr. Kelly Sulick, who was always enthusiastic and encouraging in my music endeavors, adding a colorful part to my graduate life. I need to thank all my friends in Charlottesville and in many parts of the world, for always ready to listen when I need them and for sharing with me their stories. Finally, I need to thank my family for their unconditional love and for being there whenever I need.

Table of Contents

Chapter 1 Introduction: Subtype dependent degeneration of intrinsically photosensitive retinal ganglion cells in glaucoma

Introduction

Glaucoma is a group of eye diseases that affects more than 70 million people worldwide and causes 10% of those afflicted to be bilaterally blind, making it one of the main causes of blindness (Li et al., 2014; Quigley & Broman, 2006). The pathogenesis of glaucoma is poorly understood, although elevated intraocular pressure (IOP) is one of the main risk factors for glaucoma. Rodent models of glaucoma have thus been developed to mimic this aspect of glaucoma using surgical methods or genetic tools to induce IOP elevation with differing severities and durations (Feng, Chen, et al., 2013; Rangarajan et al., 2011; Sappington et al., 2010; Thomson et al., 2020). Studies, including ours, have shown the gradual degeneration of retinal ganglion cells (RGCs) in a cell type-dependent manner in mouse glaucoma models (reviewed by Ou et al., 2016 and Puyang et al., 2015). A subclass of RGCs, the intrinsically photosensitive retinal ganglion cells (ipRGCs), has drawn a lot of attention for its resistance to insult and disease (Gao et al., 2022; Cui et al., 2015). The defining feature of ipRGCs is that they express melanopsin (Provencio et al., 1998; Provencio et al., 2000; Provencio et al., 2002). They can be classified into six types, M1 through M6, that serve a broad array of visual and non-visual responses to light (reviewed by Do, 2019). These responses include but are not limited to the photoentrainment of circadian rhythms (Panda et al., 2002; Ruby et al., 2002), the pupillary light reflex (Lucas et al., 2003), and the acute photic suppression of melatonin biosynthesis (Panda et al., 2003). This review is focused on the type-specific ipRGC loss and the consequences on visual and non-visual effects of light with glaucoma development and progression.

Rodent and Primate ipRGCs

Since their discovery, a plethora of studies have been published on ipRGCs, and we now know that this group of cells is heterogeneous (Do, 2019). In rodents, ipRGCs specifically labeled with melanopsin antisera have cell bodies located in both the ganglion cell layer (GCL) and inner nuclear layer (INL), with dendrites stratifying in the OFF sublamina of the inner plexiform layer (IPL) (Baver et al., 2008; Provencio et al., 2002). These cells were named M1 ipRGCs (M1s), and M1s with somata located to the INL were named displaced M1 ipRGCs (dM1s) (Berson et al., 2010; Gao et al., 2022). Retrograde tracing showed that the majority of the suprachiasmatic nucleus (SCN)-projecting RGCs are M1s and dM1s (Baver et al., 2008). M1s can be divided further into two populations based on expression of Brn3b, a transcription factor expressed in RGCs (Chen et al., 2011). The Brn3b-negative M1s innervate the SCN exclusively, while the Brn3b-positive M1s innervate other brain targets such as the olivary pretectal nucleus (OPN) (Chen et al., 2011; Do, 2019; Hattar et al., 2002). M1s are mainly involved in the nonimage-forming functions such as circadian photoentrainment, the pupillary light reflex, and the photic regulation of sleep (Do, 2019; Duda et al., 2020; Lucas et al., 2003; Panda et al., 2003; Ruby et al., 2002; Semo et al., 2014).

A second type of more faintly labeled ipRGC with dendrites stratifying in the ON sublamina of the IPL were named M2 ipRGCs (Baver et al., 2008). Although a small percentage of SCN innervation come from the M2s, suggesting their involvement in circadian functions, M2s also project to the dorsal lateral geniculate nucleus (dLGN), a principal target of RGCs in the thalamus that is important for image-forming vision (Ecker et al., 2010). M1s and M2s constitute a fraction of the total RGC population in mouse retina exhibiting a density of about 50-70 cells/mm^2 (**see Tables 1 and 4**) (Berson et al., 2010; Gao et al., 2022; Hughes et al., 2013; Jain et al., 2012). A third type of ipRGCs, the M3s, (Berson et al., 2010; Ecker et al., 2010) have dendrites stratifying in both ON and OFF sublaminae of the IPL, with somata more closely resembling those of M2s than M1s in size and labeling intensity (Schmidt et al., 2011). However, the M3 population is extremely sparse, representing less than 10% of ipRGCs labeled with melanopsin antisera. Furthermore, it does not tile the retina in a regular mosaic causing some to question whether this population meets the criteria for a true RGC type (Sanes & Masland, 2015).

More ipRGC types were identified using a Cre-based knock-in mouse line that expresses Cre recombinase in place of the melanopsin gene (*Opn4*) open reading frame (Ecker et al., 2010). When crossed with a cre-dependent human placental alkaline phosphatase reporter mouse line, approximately 2058 ± 141 cells per retina were found to express melanopsin, a larger number than previously described using standard immunostaining methods (**See table 1**). An additional ipRGC type, the M4 ipRGC, also known as the ON alpha cell, was labeled in this line (Ecker et al., 2010). The M4s have larger somata and dendritic arbors than the M1s, M2s, and M3s and, like the M2s, have dendrites exclusively stratifying in the ON sublamina of the IPL. M4s express a lower level of melanopsin (Berson et al., 2010; Estevez et al., 2012; Gao et al., 2022; Schmidt et al., 2014; Sonoda, Okabe, et al., 2020) and show lower intrinsic photosensitivity in single-cell electrophysiological recordings compared to M1s (Estevez et al., 2012; Hu et al., 2013). Retrograde tracing confirmed that M4s projects to the superior colliculus (SC) and dLGN, suggesting these cells are involved in image-forming vision (Cang et al., 2018; Zhao et al., 2014; (Estevez et al., 2012). The density of M4s in the mouse retina is about 50 cells/mm^2, slightly lower than the M1 and M2s (see **Tables 1** and **4).**

Also labeled in Cre-based knock-in mouse lines is the M5 ipRGC type (Ecker et al., 2010; Hughes et al., 2013; Sonoda, Okabe, et al., 2020; Stabio et al., 2018). M5s have compact and highly branched dendrites stratifying in the ON sublamina of the IPL. They exhibit chromatic opponency and project heavily to the dLGN and vLGN, suggesting their involvement in image-forming vision. One last type, the M6 ipRGC, was identified in pigmented Cdh3-GFP BAC transgenic mice (Quattrochi et al., 2019). They have bistratified dendrites and small somata distinguishable from other ipRGCs. Like the M5s, they express a very low level of melanopsin and project to the dLGN, suggesting they likely contribute to the image-forming vision. As methods to selectively label these cells are limited, the density of M5s and M6s are not clear.

ipRGCs also have been identified in other mammals such as the tree shrew (Johnson et al., 2019), whale (Ruzafa et al., 2022), and primates (Esquiva et al., 2017; Hannibal et al., 2017; Liao et al., 2016; Mure et al., 2019; Nasir-Ahmad et al., 2019). Adult human eyes contain about 4000 to 7500 cells immunolabeled with the anti-melanopsin antisera (See **Table 2** and **Table 4**). Four types of ipRGCs have been identified based on morphological features. Two of the identified types correlate with the murine M1 and M2 ipRGCs. However, about half of the human M1s have their soma located to the INL instead of the GCL (Esquiva et al., 2017; Liao et al., 2016; Nasir-Ahmad et al., 2019). In another study, the human M1s were subdivided into four different subtypes: the giant M1s (GM1s) which have large somata located to the GCL and large dendritic fields, the M1s which have smaller soma in the GCL and smaller dendrites fields than the GM1s, and displaced versions of the M1s and GM1s (Hannibal et al., 2017). The intrinsic photosensitivity of human M1s has also been confirmed using multielectrode array recording (Mure et al., 2019).

The human M2s are monostratified and have their highly branched dendrites terminating in the inner border (ON sublamina) of the IPL. Their somata are located in the GCL and are significantly larger than the M1 somata (Liao et al., 2016; Nasir-Ahmad et al., 2019). They are less sensitive to light compared to the M1s (Mure et al., 2019). The human counterpart of mouse M3s have bistratified dendrites and are distributed mainly in the inferior and nasal aspects of the retina (Hannibal et al., 2017; Liao et al., 2016; Nasir-Ahmad et al., 2019). In one study, however, M3s were found to form a regular mosaic (Esquiva et al., 2017). Finally, the human M4s, have dendrites located in the ON sublamina of the IPL (Hannibal et al., 2017), though at a slightly greater depth compared to the M2s, similar to that observed in the mouse retina (Estevez et al., 2012). To date, no human M5 or M6 ipRGCs have been identified, which may be due to the limited access to samples and inadequate sensitivity of the techniques used to label ipRGCs.

Central targets of ipRGCs have been described in macaque (Hannibal et al., 2014). Using anterograde tracing and pituitary adenylate cyclase-activating polypeptide (PACAP) immunostaining, Hannibal *et al.* (2014) found that macaque ipRGCs project to the SCN, LGN, SC, and other brain areas. It is likely that like the mouse ipRGCs, primate ipRGCs contribute to both image-forming and nonimage-forming vision. More studies are needed to elucidate how each type of primate ipRGCs contributes to the variety of functions.

Nonuniform Distribution of ipRGCs Subtypes

Studies are inconsistent on whether ipRGC distribution is uniform across the retina (Honda et al., 2019) (Hughes et al., 2013; Quattrochi et al., 2019; Sonoda, Okabe, et al., 2020). Hughes *et al.* (2013) showed that total ipRGCs (M1 to M5) labeled in the *Opn4*$^{Cre+/-}$*;EYFP*$^{+/+}$ mouse line exhibited a uniform density, but M1 and M2 ipRGC subtypes labeled by melanopsin antisera showed a superior-inferior gradient (see **Table 3**). The M4 and M5 cells exhibited the reverse gradient, where significantly higher density was found in the inferior retina (Hughes et al., 2013). However, we found a significantly higher density of total ipRGCs in the temporal versus the nasal retina ($p < 0.001$, *student's t-test*) , and in the inferior versus the superior retina ($p < 0.001$, *student's t-test, unpublished data,* **Table 3**). We also noticed a significantly higher density of displaced M1s in the superior ($p < 0.01$, *student's t-test*) and temporal retina ($p < 0.001$, *student's t-test, unpublished data*). M4 cells are also found to be more densely distributed in the temporal than nasal retina ($p < 0.001$, *student's t-test*) , but not in the superior retina ($p = 0.08$, *student's t-test, unpublished data*). Our results are in agreement with other studies that show M4s more densely populate the superior-temporal retina in mice (Bleckert et al., 2014; Sonoda, Okabe, et al., 2020).

The distribution of ipRGCs also varies across the retina of the tree shrew *Tupaia belangeri*, a protoprimate, where ipRGCs show highest density in the ventral-temporal retina (Johnson et al., 2019). Moreover, different ipRGC types have different spatial arrangement; while the bistratified ipRGCs were highest in the temporal retina, the dopaminergic ipRGCs were more uniformly distributed. In human retina, ipRGC density and dendritic morphology also differ depending on retinal location (Hannibal et al., 2017; Nasir-Ahmad et al., 2019). While M1s show the highest density in the temporal retina, GM1s, M2 and M4s are more densely distributed in the nasal retina. In fact, M2s and M4s are absent in the peripheral region of the temporal retina (Hannibal et al., 2017). The higher density of M2 cells in the nasal retina was confirmed by another study (Nasir-Ahmad et al., 2019).

The differential distribution of human ipRGCs may have biological significance as localized illumination of different regions of the retina shows different effectiveness in melatonin suppression (Glickman et al., 2003; Rüger et al., 2005). In mice, the opsin gradients in the retina correlate with the spectral tuning of ipRGC types (Hughes et al., 2013). Alternatively, strain differences could account for the non-uniform distribution of ipRGCs. The total number of ipRGCs between albino Swiss and C57BL/6 mice are similar, but ipRGCs are more densely distributeed in the temporal retina in C57BL/6, while they are more abundant in the superior retina of albino mice (Valiente-Soriano et al., 2014). More work remains needed to characterize the spatial distribution of ipRGCs and the attendant behavioral functions.

ipRGC Degeneration in Glaucoma

The survival of ipRGCs has been examined in various rodent glaucoma models and in glaucoma patients, but results remain equivocal (Ahmadi et al., 2020; Ciulla et al., 2019; De Zavalía et al., 2011; Drouyer et al., 2008; Duan et al., 2015; Feigl et al., 2011; Gao et al., 2022; Gracitelli et al., 2014; Kankipati et al., 2011; Kelbsch et al., 2016; Kuze et al., 2017; La Morgia et al., 2010; Li et al., 2006; Vidal-Sanz et al., 2017; Wang et al., 2013). Some studies suggest that ipRGCs suffer less degeneration than general RGC population. For example, Li et al. (2006) induced continuous IOP elevation for four months through laser photocoagulation of the episcleral veins of rat eyes. They found that although the general SC-projecting RGCs suffered about a 24% cell loss, M1 ipRGC density and dendritic architecture remained stable (Li et al., 2006). In our recently published study (Gao et al., 2022), mild IOP elevation was induced for more than three months in the mouse retina by laser photocoagulation of the trabecular meshwork. Cell loss of panRGCs and ipRGC types was quantified at 6-8 months post-laser surgery (Gao et al., 2022). The ipRGCs labeled by melanopsin antisera suffered 16% cell loss, while the general population of RGCs suffered a significantly greater 25-32% cell loss (See **Table 4**). Other rodent studies suggest ipRGCs degenerate in a similar pattern and at a similar rate as the general RGC population. In rats, short term IOP elevation was induced for about two weeks and ipRGCs were found to degenerate substantially, similar to the general RGC population (Valiente-Soriano, Nadal-Nicolás, et al., 2015). When IOP elevation was induced for 10 weeks by injection of chondroitin sulfate into the anterior chamber of the eye of rats, a significant 50% reduction in melanopsin expression was found, while the expression level of the general RGC marker Thy-1 suffered a comparable 45% reduction (De Zavalía et al., 2011). This result, however, could be interpreted as that melanopsin protein expression itself fluctuates following IOP elevation (Nadal-Nicolás et al., 2015; Vidal-Sanz et al., 2017). Interestingly, in Thy1-CFP-DBA/2J mice, a genetic model of glaucoma with a progressive IOP elevation starting from 2 months of age until 11 months when it plateaus, the general RGCs suffered a 33% cell loss, while the ipRGCs (likely M1s) suffered a significantly greater 60% cell loss at 14 months of age (**Table 4**) (Zhang et al., 2013).

The differences in the above findings may be due to the variability in the severity and duration of IOP elevation induced in the different models of glaucoma. In addition, type-specific survival of ipRGCs may contribute to the differences observed in general ipRGC survival. For example, we showed that M4s and M2s suffered a 25% and 23% cell loss, but the density of M1s and displaced M1s remained stable. Accordingly, we observed impacts on visual parameters such as contrast sensitivity and acuity but no major effects on circadian photoentrainment (Gao et al., 2022). Another study investigated the projection of RGC axons to various brain targets and found a loss of retinal fibers afferent to the SCN in a rat model of glaucoma in which IOP elevation was induced for four months by repeated laser treatment of the episcleral veins (Drouyer et al., 2008). Apart from changes in ipRGC axons, the ipRGC dendrites also underwent substantial remodeling (El-Danaf & Huberman, 2015)(Zhang et al., 2013). While variations in study design may obscure a generalized understanding of ipRGC degeneration in the context of glaucoma, they may offer insights in clinical glaucoma where patients also suffered from different degrees of IOP elevation and varied rates of deterioration of visual and non-visual functions.

The underlying pathogenesis of ipRGC loss remains to be understood. One hypothesis is that elevated IOP can cause mechanical stress on the lamina cribrosa beneath the optic nerve head (ONH), where the axons bundles exit the eye (Bellezza et al., 2000; Calkins, 2012; Chidlow et al., 2011; Levin, 2001; Quigley et al., 1981; Weinreb et al., 2014). This stress leads to disruption of axonal transport, as well as disorganization of microtubules and neurofilaments at the ONH, causing metabolic stress for the RGCs (Burgoyne, 2011; Calkins, 2012; Howell et al., 2013). These initial insults to axons eventually are transmitted to the somata, leading to apoptotic degeneration of the RGC cell bodies (Howell et al., 2013; Quigley, 2016). Therefore, experimental models that induce damage to RGC axons may share similarities with glaucoma models, even without IOP elevation. ipRGCs have been found to survive better than general RGCs in the optic nerve crush (ONC) and optic nerve axotomy (ONA) models. In mice, one month post-optic nerve transection (Robinson & Madison, 2004), panRGCs labeled by Tuj1 suffered 88% cell loss while ipRGCs (likely M1s) suffered only a 58% cell loss. Results from mouse ONC models also agreed with the results from the rat otic nerve transection model. At 14- and 28- days post ONC, the survival of panRGCs and ipRGCs were examined using immunostaining methods (Duan et al., 2015). While the general RGC population suffered 80% and 90% cell loss at 14- and 28- days post-ONC, respectively (see **Table 4**), M1s suffered only 30% and 60% cell loss, respectively. The M4s demonstrated even higher survival rates than the M1s, with only 20% and 40% cell loss, respectively. The M2s, on the other hand, were almost all absent. The same result was confirmed in another study using single cell RNA-seq techniques (Tran et al., 2019). All ipRGCs were found to be resistant to degeneration at 14- days post-ONC, with M4s showing the highest survival rate among all ipRGCs (Tran et al., 2019).

Though an elevated IOP is associated with majority of glaucoma cases, some patients do not exhibit elevated IOP (Weinreb et al., 2014; Weinreb & Tee Khaw, 2004), suggesting that factors other than IOP elevation contribute to glaucoma disease progression (Calkins, 2012; Wang et al., 2020). Some glaucoma patients show downregulation of glutamate transporters (Naskar et al., 2000). The GLAST KO mouse model is devoid of a transporter of aspartate and glutamate and exhibits progressive loss of RGCs and axon bundles in the absence IOP elevation (Honda et al., 2019). In these mice, when half of the general RGC population had degenerated, only 10% of ipRGCs (M1s and M2s) were lost. Moreover, alpha RGCs, a group that contains M4s, also showed excellent resistance to degeneration, suffering only a 4% cell loss.

Studies that directly address ipRGC survival in human glaucoma cases are lacking. To date, only one group examined ipRGCs survival in human glaucoma patients and age-matched controls (Obara et al., 2016). They found that while almost all RGCs labeled by the pan RGC marker rbpms (Rodriguez et al., 2014) were gone in severe glaucoma patients, ipRGCs only suffered about a 50% loss. Interestingly, while ipRGCs in the GCL suffered a substantial 88% cell loss, no significant cell loss was found in the ipRGCs with somata in the INL, suggesting human displaced M1s cells are more resistant to glaucomatous damage than non-displaced M1s. In addition, mitochondrial dysfunction and retinal ganglion degeneration are observed in Leber hereditary optic neuropathy (LHON) and Kjer type dominant optic atrophy (DOA). One study examined the cell loss within the general RGC population and ipRGCs in post-mortem retinas from these visually impaired patients (La Morgia et al., 2010). They found that although most RGCs have degenerated in the three patients examined ranging from a 74% to 98% loss, only about half of the ipRGCs were lost (see **Table 4**).

ipRGC survival in glaucoma patients can also be examined indirectly. Employing a receptor silent substitution paradigm, one study compared the electrophysiological responses of ipRGCs in glaucoma patients to normal subjects and found that the amplitude of ipRGC responses of glaucoma patients was greatly reduced compared to those of the controls (Kuze et al., 2017). As glaucomatous human retinas are difficult to acquire and study, protoprimate models of glaucoma have been established (Burgoyne, 2015). For example, tree shrews are evolutionary intermediates to primates and rodents with a diurnal visual system similar to primates (Zhou et al., 2015); (Van Hooser et al., 2013). An experimental tree shrew glaucoma model has been developed that induces IOP elevation through microbead injection into the eye (Samuels et al., 2018). Three ipRGC subtypes have been identified in the tree shrew retina that share morphological traits with the primate ipRGCs (Johnson et al., 2019). It will be of interest to examine their survival under elevated IOP, and the findings may offer insights to how primate/human ipRGCs respond to the insult of glaucoma.

ipRGC Related Behavioral Changes in Glaucoma

It is known that the majority of retinal afferents to the SCN, arises from M1 ipRGCs (Baver et al., 2008), suggesting they contribute to circadian photoentrainment (Jones et al., 2015). Indeed, it also is known that Brn3b-negative M1s are sufficient for circadian photoentrainment (Chen et al., 2011). When ipRGCs projecting to non-SCN and non-IGL (intergeniculate leaflet) brain targets are ablated (Rupp et al., 2019), mice retained circadian photoentrainment, while other functions, such as the pupillary light reflex and contrast sensitivity, showed deficits. Moreover, the M1 electrophysiological profiles are tuned to transmit accurate visual signals to the SCN (Stinchcombe et al., 2021). Therefore, M1 cell loss may lead to deficits in photoentrainment, which has been reported in several studies using rodent glaucoma models (De Zavalía et al., 2011; Drouyer et al., 2008). Rats with bilaterally elevated IOP showed reduced retinal fibers to the SCN (Drouyer et al., 2008). While they retain the ability to re-entrain to shifted light-dark (LD) cycles, the number of days required to establish a stable phase of activity was significantly longer than the control rats. Moreover, the stability of the phase of activity onset was somewhat variable relative to the start of the dark period (Drouyer et al., 2008). Similarly, another group found reduced melanopsin expression and reduced ipRGC density after IOP elevation in rats that were able to entrain to shifted LD cycle, but with a delayed phase angle of activity onset (De Zavalía et al., 2011).

As degeneration of ipRGCs including M1s are also observed in human glaucoma patients (Obara et al., 2016) and in optic neuropathy (La Morgia et al., 2010), dysregulation of circadian rhythmicity was seen in primary open angle glaucoma (POAG) patients. Higher sleep disturbances, lower average sleep time, lower sleep efficiency and higher arousal are observed in glaucoma patients (Gracitelli, Duque-Chica, et al., 2015; Wang et al., 2013) and the ratio of patients with sleep disorders increases with greater visual field impairment (Ayaki et al., 2016; Wang et al., 2013). Normally, light stimulation suppresses melatonin production, a process that heavily relies on ipRGCs. However, in glaucomatous mice, blue light exposure is unable to reduce pineal melatonin levels (De Zavalía et al., 2011). Decreased melatonin secretion was also seen in human glaucoma patients (La Morgia et al., 2010; Ma et al., 2018; Yoshikawa et al., 2020). Moreover, in advanced an glaucoma group, no significant nocturnal melatonin suppression is apparent after bright light exposure (Pérez-Rico et al., 2010). Together these studies suggest a possible positive correlation between M1 cell loss and non-visual deficits in glaucoma.

However, in normal tension glaucoma (NTG) patients, sleep quality as measured by the Pittsburgh Sleep Quality Index did not differ significantly from controls (Ahmadi et al., 2020). This difference may be caused by the severity of the disease in the subjects selected. Moreover, in our recently published study (Gao et al., 2022), we found that mice M1s are resistant to degeneration after sustained mild IOP elevation generated by laser photocoagulation of the trabecular meshwork. However, while no significant deficit in circadian re-entrainment is seen in bilaterally lasered mice, re-entrainment is accelerated when these mice are subjected to a six-hour phase advance of a relatively bright LD cycle. Mice subjected to a shift of a dimmer LD cycle do not show this accelerated re-entrainment. Acceleration of re-entrainment to a shift in a bright LD cycle reflects a change in basic underlying parameters of the circadian system in the glaucomatous mice. The SCN is a hierarchical structure that maintains and regulates circadian rhythmicity through the coordination of its many autonomous cellular oscillators (Antle & Silver, 2005; Paul et al., 2009; Welsh et al., 2010). The desynchrony between these cellular oscillators may lead to a change in the rate of circadian entrainment. For example, administration of vasoactive intestinal peptide (VIP) before an LD cycle shift increases desynchrony among the individual cellular oscillators resulting in a dampening of the amplitude of the composite SCN rhythm. This reduced amplitude facilitates the perturbation of phase necessary for re-entrainment. As such, the more dampened the amplitude, the more quickly the SCN can re-entrain its phase to a shifted LD cycle. (An et al., 2013). Therefore, we hypothesize that reduced or changed inputs to the SCN, either through the alteration of the direct photic input from the retina or changes in inputs from other nuclei in the brain, may cause desynchrony between these oscillators and alter their phase distribution, ultimately leading to the subtle changes in re-entrainment that we observed in our surgical glaucoma model. Even though the M1 cell density did not change in our glaucoma mice (Gao et al., 2022) , the synaptic input from them could be reduced or even enhanced. For example, reduced ipRGC axonal inputs to SCN has been observed in a rat glaucoma model (Drouyer et al., 2008). Arbor shrinkage (Zhang et al., 2013) and change in dendritic complexity (El-Danaf & Huberman, 2015) have also been noticed in mice models of glaucoma. Interestingly, in aging dystrophic rat retina, the ipRGC cell count is reduced, although the total number of melanopsin-positive dendritic processes remains the same, suggesting a compensatory remodeling and expansion of the ipRGC dendrites in disease (Vugler et al., 2008). Taken together, changes in ipRGC morphology, function, and axonal projections may exert subtle effects on the direct photic input to the SCN. In addition, the expression level of melanopsin has been found to decrease or fluctuate in glaucoma animal models (De Zavalía et al., 2011; Vidal-Sanz et al., 2017). This may affect circadian entrainment, as melanopsin null animals exhibit reduced phase-shifting responses (Panda et al., 2002; Ruby et al., 2002; Wang et al., 2022).

Glaucoma may also affect the master circadian clock through indirect pathways as the SCN receives afferents from multiple regions in the brain (Abrahamson & Moore, 2001; Yuan et al., 2018). Specifically, Grippo *et al.* (2017) found that dopaminergic neurons in the ventral tegmental area (VTA) project to the SCN and their activation accelerates photoentrainment in mice (Grippo et al., 2017). Moreover, a recently published study found that the VTA of mice receives inputs from the preoptic area that in turn receives direct inputs from M1s (Zhang et al., 2021), a pathway involved in the regulation of non-rapid eye movement (NREM) sleep. Therefore, change in M1 axonal inputs within this pathway also indirectly may alter circadian rhythms in mice. Alternatively, in our glaucoma mice model, we observe a decrease in M4 cells (Gao et al., 2022) which project to the intergeniculate leaflet (IGL) (Ecker et al., 2010). The IGL, in turn, encodes irradiance and sends a projection to the SCN via the geniculohypothalamic tract (Morin & Studholme, 2014; Yuan et al., 2018). Therefore, the degeneration of M4 cells could affect the IGL's modulation of the retinal input to the SCN and indirectly impact its behavioral output (Hanna et al., 2017). It is important to point out that circadian dysfunction in glaucoma patients may not be solely due to ipRGC degeneration and altered photic input. Other factors, such as reduced social interactions (Golombek & Rosenstein, 2010) and mood disorders (Vadnie & McClung, 2017) may also contribute to the process.

It is known that alterations in circadian rhythmicity are related to hyperactivity disorders such as Attention-Deficit/Hyperactivity Disorder (Baird et al., 2011; Coogan et al., 2016). Therefore, similar phenotypes may exist in glaucoma. In fact, a significantly higher activity-to-rest ratio relative to controls is observed in an experimental rat model of glaucoma (De Zavalía et al., 2011) and in a genetic mouse model of glaucoma (Zhang et al., 2013). Similarly, in glaucoma patients, a significant increase in daily activity and wake time is observed (Lanzani et al., 2012). Circadian dysfunction can also be at the root of mood disorders and depression (Golombek & Rosenstein, 2010). It is becoming more appreciated that light is heavily involved in mood regulation, a process mediated mainly through ipRGCs, through SCN-dependent and independent pathways (An et al., 2020; Maruani & Geoffroy, 2022). The prevalence of mood disorder and depression is significantly higher in glaucoma patients than matched controls (Ayaki et al., 2016; Yoshikawa et al., 2020).

ipRGCs also are involved in other non-image-forming visual functions that are affected in glaucoma. Brn3b-positive M1 ipRGCs project to the olivary pretectal nucleus (OPN) (Baver et al., 2008; Ecker et al., 2010; Rupp et al., 2019), a region in the brain that controls the pupillary light reflex (PLR), the constriction of the pupil in response to bright light stimulation. In a rat model of unilateral glaucoma, with 50% ipRGC loss, a significant decrease in the magnitude of the consensual pupil constriction is observed in the contralateral intact eye (De Zavalía et al., 2011). Deficits in the PLR in human glaucoma patients have also been observed. Multiple studies have reported a significantly reduced PLR response in POAG (Gracitelli, Duque-Chica, et al., 2015; Kelbsch et al., 2016; Nissen et al., 2014), NTG (Ahmadi et al., 2020) and hereditary optic neuropathy (Kawasaki et al., 2014) patients compared to healthy subjects. This reduction in PLR response is more apparent after blue light stimulation compared to red light stimulation (Kelbsch et al., 2016; Nissen et al., 2014) which is consistent with the blue light sensitivity of melanopsin, the photopigment of ipRGCs. Although deficits in PLR are observed, it is not completely abolished. Relative maintenance of the PLR is seen in LHON and DOA patients (La Morgia et al., 2010). Moreover, in one patient with advanced secondary glaucoma, a pupillary response was retained even though no cognitive perception of light remained (Zhou et al., 2014). This is no surprise given the injury resistance of ipRGCs. Deficits in the PLR are positively correlated to the severity of disease. While a significant difference is found in the post-illumination pupil response between advanced glaucoma patients and early glaucoma patients, such a deficit is not apparent between patients with early glaucoma and healthy controls (Feigl & Zele, 2014), a pattern also observed in hereditary optic neuropathy (Kawasaki et al., 2014). Indeed, the degree of visual field loss is linked to the half-max intensity of pupil responses (Kawasaki et al., 2014).

Though a great number of ipRGC studies focus on the non-image-forming aspects of vision, increasing attention is being directed to the contributions of ipRGCs to image-forming vision. M2, M4, M5 and M6 cells and a small percentage of M1 cells send their axons to the dLGN, the principle relay for visual information to the visual cortex (Do, 2019; Quattrochi et al., 2019;

Schmidt et al., 2014; Stabio et al., 2018). Such circuitry suggests that these types of ipRGCs contribute to image-forming vision. Indeed, following ablation of several ipRGC types including the M4s (Schmidt et al., 2014), contrast sensitivity is significantly reduced at various spatial frequencies (0.05 and 0.09 c/d) to which M4s respond most strongly in isolated retina (Estevez et al., 2012). No such deficits in contrast sensitivity are observed in mice where only a subpopulation of M1s are knocked out (Schmidt et al., 2014), suggesting that existing M4s may contribute to contrast sensitivity. In mice ocular hypertension models, we observed a significantly reduced M4 density which also exhibited a significant decrease in contrast sensitivity measured by the optomotor test (Gao et al., 2022). Moreover, these mice demonstrate a greater reduction of contrast sensitivity at 0.103 c/d than 0.192 c/d (Figure 4c), which correlates with M4 degeneration. However, this does not exclude the possibility that degeneration of other non-M4 RGCs may contribute to the change in contrast sensitivity in the OHT mice, as the general RGC population suffered substantial cell loss (Baden et al., 2016b; Khani & Gollisch, 2017). Distinguishing the contributions of ipRGCs and non-ipRGC ganglion cells to image-forming vision is challenging, and currently, little is known on how image-forming visual functions mediated by ipRGCs are affected in glaucoma patients. To address the issue, the previously mentioned “silent substitution” paradigm has been developed (Allen et al., 2019) to examine the difference in melanopsin-mediated photoresponses between healthy subjects and glaucoma patients.

In conclusion, ipRGC-mediated image-forming and non-image-forming visual behaviors may be altered in glaucoma. A better understanding of ipRGC type-dependent degeneration and the corresponding ipRGC-driven neural circuits that account for the behavioral changes suffered by glaucoma patients is needed. The results will help to improving patient care and treatment as glaucoma develops and progresses.

Tables

Table 1. Rodent ipRGCs density

Species	Cell type	Quantification method	Density (cells/mm^2)	Cells per retina	Source
Mouse	Total ipRGCs	Transgene (Opn4$^{Cre/+}$; Z/AP)		2058 ± 141 (n = 4)	(Ecker et al., 2010)
		Immunohistochemistry	113 ± 21 (n = 9)	1194 ± 281 (n = 9)	(Jain et al., 2012)
		Transgene (Opn4.Cre$^{+/-}$. EYFP$^{+/+}$)		4415–4705 (n = 2)	(Hughes et al., 2013)
		Immunohistochemistry		1021 ± 109 (n = 19) in C57BL/6 962 ± 169 (n = 21) in albino mice	(Valiente-Soriano et al., 2014)
		Immunohistochemistry	219.6 ± 3.0 (n=16, ± SEM)		(Gao et al., 2022)
	*M1	Immunohistochemistry		680 and 780	(Hattar et al., 2002)
		Transgene (Opn4$^{tau\text{-}lacZ}$)		About 600	(Hattar et al., 2002)
		Transgene (Opn4$^{tau\text{-}lacZ}$)		About 750	(Hattar et al., 2006)
	M1	Immunohistochemistry	63	891	(Berson et al., 2010)
		Immunohistochemistry		920	(Hughes et al., 2013)
		Immunohistochemistry	54.4 ± 3.1 (n=3, ± SEM)		(Gao et al., 2022)
	Brn3b- M1	Immunohistochemistry	71 ± 22 (n = 4)	749 ± 309 (n = 4)	(Jain et al., 2012)
	Displaced M1	Immunohistochemistry	^25	250	(Berson et al., 2010)
		Immunohistochemistry	7.0 ± 0.7 (n=16, ± SEM)		(Gao et al., 2022)
	M2	Immunohistochemistry	59	830	(Berson et al., 2010)
		Immunohistochemistry		827	(Hughes et al., 2013)
	*M4	Immunohistochemistry	61	850	(Berson et al., 2010)
	M4	Transgene (Opn4$^{Cre/+;}$ Brainbow-1.0) Immunohistochemistry		856	(Schmidt et al., 2014)
		Immunohistochemistry	52.2 ± 2.0 (n=10, ± SEM)		(Gao et al., 2022)
Rat	Total ipRGCs	Immunohistochemistry		2320 and 2590	(Hattar et al., 2002)
	Displaced ipRGCs	Immunohistochemistry		^116 and 130	(Hattar et al., 2002)

*Subtype classified based on morphology or quantification method when it is not specified in original study.
^Estimated numbers from figures or calculated from other measurements in study when direct citation is not available.
Numbers are reported as mean ± SD if not otherwise stated

Table 2. Primate ipRGCs density

Species	Cell type	Quantification method	Density (cells/ mm^2)	Cells per retina	Source
Tree Shrew	Total ipRGCs	Immunohistochemistry		2899 and 3272	(Johnson et al., 2019)
	M1	Immunohistochemistry	About 10	^736 and 954	(Johnson et al., 2019)
	Displaced M1	Immunohistochemistry		268 and 256	(Johnson et al., 2019)
	M2	Immunohistochemistry		27 and 81	(Johnson et al., 2019)
	dopaminergic ipRGCs	Immunohistochemistry		1868 and 1981	(Johnson et al., 2019)
Macaque	Total ipRGCs	Immunohistochemistry	20-25 in the parafovea	About 3000	(Liao et al., 2016)
Human	Total ipRGCs	Immunohistochemistry	30-30 in central retina; 8-10 in periphery	About 4400	(Liao et al., 2016)
		Immunohistochemistry		7520 and 7046	(Hannibal et al., 2017)
		Immunohistochemistry	4.77	4700	(Esquiva et al., 2017)
		Immunohistochemistry	2.47		(Mure et al., 2019)
	M1	Immunohistochemistry	0.51 ± 0.27 (n=24, ± SEM) in superior nasal area		(Esquiva et al., 2017)
		Immunohistochemistry	15-18 in central retina; 10-11 in periphery (n = 4)		(Nasir-Ahmad et al., 2019)
	Displaced M1	Immunohistochemistry	2.05 ± 0.47 (n=24, ± SEM) in superior nasal area		(Esquiva et al., 2017)
	M2	Immunohistochemistry	0.65 ± 0.33 (n=24, ± SEM) in superior nasal area		(Esquiva et al., 2017)
	M3	Immunohistochemistry	0.97 ± 0.44 (n=24, ± SEM) in superior nasal area		(Esquiva et al., 2017)

^Estimated numbers from figures or calculated from other measurements in study when direct citation is not available.

Numbers are reported as mean ± SD if not otherwise stated

Table 3. Regional differences in ipRGC distribution

Species	Cell type	Density (cells/ mm^2)				Source
		Inferior (Ventral)	**Superior (Dorsal)**	**Nasal**	**Temporal**	
Mouse	Total ipRGCs	306.6 ± 14.9 (n= 3, ± SEM)	275.3 ± 19.6 (n= 3, ± SEM)			(Hughes et al., 2013)
		228.8 ± 17.1 (n=12)	186.8 ± 23.1 (n=12)	198.1 ± 13.5 (n=12)	243.7 ± 23.3 (n=12)	unpublished
	M1	43.3 ± 7.9 (n= 3, ± SEM)	75.4± 9.1 (n= 3, ± SEM)			(Hughes et al., 2013)
	Displaced M1	3.4 ± 2.5 (n=12)	8.5 ± 4.7 (n=12)	3.1 ± 2.3 (n=12)	12.0 ± 5.0 (n=12)	unpublished
	M2	36.9 ±4.1 (n= 3, ± SEM)	81.7 ± 8.8 (n= 3, ± SEM)			(Hughes et al., 2013)
	M4	54.2 ± 13.0 (n=9)	46.7 ± 5.8 (n=9)	43.9 ± 6.0 (n=9)	67.1 ± 11.0 (n=9)	unpublished
	M4 and M5	^ about 230 (n= 3)	^ about 160(n= 3)			(Hughes et al., 2013)
Human	Total ipRGCs	9.6 ± 0.3 (n = 2)	8.6 ± 1.4 (n = 2)	13.8 ± 0.5 (n = 2)	10.9 ± 3.3 (n = 2)	(Hannibal et al., 2017)
	M1			15-18 (n=4)	15-18 in central retina and 10-11 in periphery (n = 4)	Nasir-Ahmad et al., 2019)
			0.51 ± 0.27 (n=24, ± SEM) in superior nasal area			(Esquiva et al., 2017)
	Displaced M1		2.05 ± 0.47 (n=24, ± SEM) in superior nasal area			(Esquiva et al., 2017)
	M2			19-20 (n = 4)	14-15 in central retina and 7-8 in periphery (n = 4)	(Nasir-Ahmad et al., 2019)
			0.65 ± 0.33 (n=24, ± SEM) in superior nasal area			(Esquiva et al., 2017)
	M3		0.97 ± 0.44 (n=24, ± SEM) in superior nasal area			(Esquiva et al., 2017)

Numbers are reported as mean ± SD if not otherwise stated

Table 4. ipRGC degeneration in glaucoma

Species	Model	Control	Glaucoma	ipRGC % decrease	Total RGC % decrease	Source
Mouse	Experimental glaucoma model	219.6 ± 3.0 (n=16, ± SEM)	183.4 ± 4.5 cells/ mm^2 6-9 months (n= 11, ± SEM)	16.5% (total ipRGCs)	32.6%	(Gao et al., 2022)
	Optic nerve transection	66±7 cells/mm^2 (N=6, ± SEM)	^about 28 cells/mm^2	58 % at one month (*M1-M3)	88 % at one month	(Robinson & Madison, 2004)
	Transgene (Thy1-CFP-DBA/2J)	48 ± 3 cells/mm^2 at 2 month	19±4 cells/mm^2 at 14 month	^60% at 14 month (*M1-M3)	^33% at 14 month	(Zhang et al., 2013)
	Experimental glaucoma model	1059 ± 79 and 1019 ± 140 cells per retina from 2 control groups (n = 7)	629 ± 254 and 478 ± 248 cells per retina at 2 and 4 weeks (n = 7)	40% and 53% at 2 and 4 weeks (M1-M3)	^34% and 59% at at 2 and 4 weeks	(Valiente-Soriano, Salinas-Navarro, et al., 2015)
	Transgene (GLAST)	^27-29 cells/mm^2	^24-26 cells/mm^2	NS (*M1)	48.4% ± 0.9% (± SEM)	(Honda et al., 2019)
	Optic nerve crush			^About 30% and 60% at 14 and 28 days post ONC (M1)	^About 80% and 90% at 14 and 28 days post ONC	(Duan et al., 2015)
	Experimental glaucoma model	54.4 ± 3.1 (n=3, ± SEM)	56.4 ± 1.1 cells/ mm^2 6-9 months (n=4, ± SEM)	NS (M1)	32.6%	(Gao et al., 2022)
	Experimental glaucoma model	7.0 ± 0.7 (n=16, ± SEM)	6.7 ± 1.0 cells/ mm^2 6-9 months (n=12, ± SEM)	NS (displaced M1)	32.6%	(Gao et al., 2022)
	Optic nerve crush			^Almost all gone at 14 and 28 days post ONC (M2)	^About 80% and 90% at 14 and 28 days post ONC	(Duan et al., 2015)
	Experimental glaucoma model	52.2 ± 2.0 (n=10, ± SEM)	38.8 ± 2.7 cells/ mm^2 at 6-9 months (n=10, ± SEM)	25.7% (M4)	32.6%	(Gao et al., 2022)
Rat	Experimental glaucoma model	1374 ± 74 cells per retina (n = 4, ± SEM)	763 ± 146 cells per retina (n = 4, ± SEM)	^44% at 10 weeks (*M1-M3)	About 40% at 10 weeks	(De Zavalía et al., 2011)
	Experimental glaucoma model	2178 ± 169 (n= 6) cells per retina	1082 ± 324 and 1108 ± 255 cells per retina at 12 and 15 days n = 4	^50% and 49% at 12 and 15 days (M1-M2)	^44% and 54% at 12 and 15 days	(Valiente-Soriano, Nadal-Nicolás, et al., 2015)
	Experimental glaucoma model	^25-30 cells/mm^2		NS (*M1)	^7%, 22%, 28% and 24% at 2,4,8 and 12 weeks	(Li et al., 2006)
Human	Leber hereditary	18,13 and 8 cells/mm^2	9,8 and 7 cells/mm^2	About 50% (total ipRGCs)	74%, 98% and 94%	(La Morgia et al., 2010)

	optic neuropathy (LHON) and Kjer type dominant optic atrophy (DOA)					
	Glaucoma	^About 3 cells/mm^2	^about 3 cells/mm^2 in mild glaucoma and 1.5 cells/mm^2 in severe glaucoma	NS between control and mild glaucoma ^About 50% between control and severe glaucoma (total ipRGCs)	NS between control and mild glaucoma ^About 99% between control and severe glaucoma	(Obara et al., 2016)
	Glaucoma	^about 1.4 cells/mm^2	^about 1.6 cells/mm^2 in mild glaucoma and 0.8 cells/mm^2 in severe glaucoma	NS between control and mild glaucoma Not significant between control and severe glaucoma (INL ipRGCs containing M1)	NS between control and mild glaucoma ^About 99% between control and severe glaucoma	(Obara et al., 2016)
	Glaucoma	^about 1.7 cells/mm^2	^about 1.4 cells/mm^2 in mild glaucoma and 0.2 cells/mm^2 in severe glaucoma	NS between control and mild glaucoma Not significant between control and severe glaucoma (GCL ipRGCs containing M2)	NS between control and mild glaucoma ^About 99% between control and severe glaucoma	(Obara et al., 2016)

^Estimated numbers from figures or calculated from other measurements in study when direct citation is not available.

*Subtype classified based on morphology or quantification method when it is not specified in original study.

Numbers are reported as mean ± SD if not otherwise stated

NS: not significant

Chapter 2 Differential Effects of Experimental Glaucoma on Intrinsically Photosensitive Retinal Ganglion Cells in Mice

Jingyi Gao[1†], Erin M. Griner[1†], Mingna Liu[1†], Joanna Moy[1], Ignacio Provencio[1, 2, 4 *], and Xiaorong Liu[1,2, 3, 4 *]

[1]Department of Biology, University of Virginia, Charlottesville, VA, USA

[2]Department of Ophthalmology, University of Virginia, Charlottesville, VA, USA

[3]Department of Psychology, University of Virginia, Charlottesville, VA, USA

[4]Program in Fundamental Neuroscience, University of Virginia, Charlottesville, VA, USA

†: These authors contributed equally to this work.

*: Corresponding authors, provencio@virginia.edu (Ignacio Provencio) and xl8n@virginia.edu (Xiaorong Liu).

Gilmer Hall 480,485 McCormick Rd, University of Virginia, Charlottesville, VA 22904

Acknowledgements

This study was funded by NIH grants R01EY029121 and R01EY026286. We thank Dr. Marta Grannonico for her technical support and fruitful discussions.

Conflicts of Interests: No.

Role of authors: J.G., I.P., and X.L. designed the experiments; J.G., E.M. G., M.L., and J.M. carried out the experiments and data analysis; J.G., I.P., and X.L. wrote the manuscript, and J.G., E.M.G., M.L., J.M., I.P., and X.L. edited and approved the manuscript.

Keywords: glaucoma; intrinsically photosensitive retinal ganglion cells (ipRGCs); melanopsin; circadian rhythm; visual acuity; ocular hypertension;

Abstract

Glaucoma is a group of eye diseases characterized by retinal ganglion cell (RGC) loss and optic nerve damage. Studies, including this study, support that RGCs degenerate and die in a type-specific manner following the disease insult. Here we specifically examined one RGC type, the intrinsically photosensitive retinal ganglion cell (ipRGC), and its associated functional deficits in a mouse model of experimental glaucoma. We induced chronic ocular hypertension (OHT) by laser photocoagulation and then characterized the survival of ipRGC subtypes. We found that ipRGCs suffer significant loss, similar to the general RGC population, but ipRGC subtypes are differentially affected following chronic OHT. M4 ipRGCs, which are involved in pattern vision, are susceptible to chronic OHT. Correspondingly, mice with chronic OHT experience reduced contrast sensitivity and visual acuity. By contrast, M1 ipRGCs, which project to the suprachiasmatic nuclei (SCN) to regulate circadian rhythmicity, exhibit almost no cell loss following chronic OHT. Accordingly, we observed that circadian re-entrainment and circadian rhythmicity are largely not disrupted in OHT mice. Our study demonstrates the link between subtype-specific ipRGC survival and behavioral deficits in glaucomatous mice. These findings provide insight into glaucoma-induced visual behavioral deficits and their underlying mechanisms.

Introduction

Glaucoma, characterized by retinal ganglion cell (RGC) loss and optic nerve damage, is the leading cause of global blindness (Li et al., 2014). RGCs, which exhibit diverse morphologies and functions (Sanes & Masland, 2015), convey photic information from the retina to processing centers in the brain (Quigley, 2016). Studies, including ours, have shown subtype-specific RGC loss in various models of glaucoma and optic nerve injury, yet much remains to be characterized regarding RGC subtype-associated visual deficits and their underlying mechanisms (Chen et al., 2015; Cui et al., 2015; Della Santina & Ou, 2017; Duan et al., 2015; Li et al., 2006; Tran et al., 2019).

One type of RGC, the intrinsically photosensitive retinal ganglion cell (ipRGC), plays a role in image-forming and non-image-forming photoreception (Berson et al., 2010; Panda et al., 2002). Although all ipRGCs express the rhabdomeric-like photopigment melanopsin, six distinct subtypes of ipRGCs, M1 through M6, have been described and characterized (Do, 2019; Duda et al., 2020; Sondereker et al., 2020). For example, M1 ipRGCs, having dendrites that stratify in the OFF-sublamina of the inner plexiform layer (IPL), express the highest level of melanopsin among the subtypes and exhibit the most robust intrinsic light response (Emanuel et al., 2017). M1 cells project primarily to the hypothalamic suprachiasmatic nuclei (SCN) (Berson et al., 2010), mediating the effects of light on circadian regulation of physiology and behavior (Baver et al., 2008; Berson et al., 2002; Chen et al., 2011). By contrast, the M4 ipRGCs, also known as the sustained large ON-alpha RGCs, are weakly melanopsin-positive and project to the ventromedial sector of the dorsolateral geniculate nucleus (dLGN), a site responsible for some aspects of pattern vision such as contrast sensitivity (Ecker et al., 2010; Estevez et al., 2012; Schmidt et al., 2014).

How ipRGCs are affected by glaucomatous insult remains an area of great interest. Subtype-dependent ipRGC survival has been studied in various animal models, although the results among different studies have been equivocal. For example, in a rat ocular hypertension

(OHT) model, few if any melanopsin-positive ipRGCs degenerated (Li et al., 2006). However, in mice following optic nerve crush injury, most M2 ipRGCs died, but more than 70% of M1 ipRGCs survived (Duan et al., 2015). Furthermore, physiological deficits associated with ipRGC loss have been examined in glaucoma patients and animal models. Glaucoma patients often suffer a higher prevalence of sleep disorders, which may be due to the general loss of ipRGCs (Ciulla et al., 2019; Gracitelli, Duque-Chica, et al., 2015). The pupillary light reflex, regulated by ipRGCs, was reduced in humans with glaucoma (Gracitelli, Duque-Chica, et al., 2015). In a rat model of experimental glaucoma, animals can synchronize their locomotor activities to the light: dark (LD) cycle, but they require more days to entrain to a shifted LD cycle in comparison with control rats (Drouyer et al., 2008). Yet much remains to be characterized regarding the functional changes resulting from the subtype-specific loss of ipRGCs during glaucoma development and progression.

In this study, the subtype-specific ipRGC loss and the attendant functional deficits in a mouse model of experimental glaucoma were examined. Long-term ocular hypertension was induced by laser photocoagulation and the survival of ipRGC subtypes was characterized. Furthermore, the functional consequences on circadian rhythmicity, visual acuity, and contrast sensitivity were analyzed.

Materials and Methods

Laser-photocoagulation to induce chronic OHT in mice

Adult (3-14 months) male and female wild-type (WT) C57BL/6 mice were used in this study. Ocular hypertension (OHT) was generated by laser photocoagulation of the trabecular meshwork of the eyes in 2-3 months old mice as described previously (Chen et al., 2015; Feng, Chen, et al., 2013). In brief, mice were anesthetized by intraperitoneal injection of 80 mg/kg ketamine (Kataset, Zoetis; NADA #043-304) and 4 mg/kg xylazine (AnaSed, Akorn; NADA#139-236). Eyes were dilated with topical application of 2.5% phenylephrine hydrochloride ophthalmic solution (Akorn, NDC #17478-201-15) and 1% Tropicamide Ophthalmic solution (Akron, NDC # 17478-102-12), and the aqueous humor was aspirated from the anterior eye by a glass micropipette (World Precision Instruments Inc, Sarasota, FL). Laser illumination was delivered unilaterally or bilaterally (Figure. 1) by the PASCAL Synthesis 532 system (Topcon, Oakland, NJ). Six groups of five 200 μm (diameter) laser spots with zero spacing were applied perpendicular to the corneal limbus to circumscribe the trabecular meshwork at a laser power of 120 mW and exposure time of 20 ms. This procedure took 10-15 minutes for each eye. A drop of VIGAMOX (Moxifloxacine Hydrochloride Ophthalmic solution 0.5%) was applied to prevent infection, and lubricants were applied (Puralube Vet ointment, NDC # 17033-211-38) to prevent drying and formation of a cataract. The animals then were kept on a heating pad until fully responsive.

IOP measurement and the optomotor test

Intraocular pressure (IOP) was measured in awake mice using a Tonolab rebound tonometer (iCare, Raleigh, NC, USA) as previously described (Feng, Chen, et al., 2013; Thomson et al., 2020). In brief, each mouse was placed into a soft plastic cone holder and restrained on a platform. Averages from three sets of measurements per eye were recorded. All IOP measurements were obtained under ambient lighting between 10:00 AM and 1:30 PM.

Both visual acuity and contrast sensitivity were assessed by the optomotor test

(Rangarajan et al., 2011; Thomson et al., 2020) (PhenoSysqOMR, PhenoSys GmbH, Berlin, Germany). In the optomotor test, the freely-moving animal was placed on a stationary round platform in the middle of four LCD monitors (Thomson et al., 2020). After 1-3 minutes of adaptation with a gray screen, a sine wave grating will be made to move across all 4 monitors. The animal was presented with moving gratings which were alternating clockwise and counter-clockwise for 10 seconds in each direction with varied spatial frequencies from 0.05 to 0.50 cycles/degree (c/d). The movement of the animal's head in-concert with the drifting grating was scored as "seen"; the highest spatial frequency "seen" was defined as the animal's visual acuity. The two eyes of individual mice were examined separately by reversing the drifting grating direction (i.e., a clockwise drifting grating was used to identify the visual function of the left eye, and a counterclockwise drifting grating for the right eye (Douglas et al., 2005; Feng, Zhao, et al., 2013). Contrast sensitivity was measured at two preselected frequencies: 0.103 and 0.192 c/d, each with contrasts from 1 to 0.1, defined as the Michelson contrast from the screen's luminance (maximum – minimum)/(maximum + minimum). The contrast threshold for each eye is defined as the lowest contrast that elicits responses at the pre-fixed frequency, and contrast sensitivity is the reciprocal of the threshold (Prusky et al., 2004).

Immunohistochemistry and confocal imaging

Mice were euthanized with 600 mg/kg euthasol (Euthasol, Virbac ANADA, # 200-071) and perfused with 4% paraformaldehyde (PFA) (ChemCruz, sc-281692). Eye cups were dissected, post-fixed in PFA for 30 minutes, washed with phosphate buffered saline containing Triton-X detergent (PBST, 0.5% Triton X-100), and then blocked for 1 hour in blocking buffer (1% BSA and 10% normal donkey serum, 0.5% Triton X-100 (Sigma-Aldrich, St. Louis, MO, USA). Primary antibodies, diluted using blocking buffer, included a rabbit polyclonal anti-melanopsin (1:2000) (Panda et al., 2002), mouse anti-SMI-32 (Biolegend, 801702/01, 1:250, RRID: AB_2715852), mouse anti-Brn3a (Millipore, MAB1585, 1:125, RRID: AB_94166) and rabbit anti-rbpms (Abcam, ab194213, 1:500). Secondary antibodies, including donkey anti-mouse immunoglobulin G conjugated to Alexa Fluor 594 dye (Invitrogen A-21203, RRID: AB_141633), donkey anti-mouse immunoglobulin G conjugated to Alexa Fluor 647 dye (Invitrogen A-31571, RRID: AB_162542) and donkey anti-rabbit immunoglobulin G conjugated to Alexa Fluor 488 dye (Invitrogen A-21206, RRID: AB_2535792), were also diluted at 1:1000 in blocking buffer and incubated overnight at 4°C. After immunostaining, retinas were flat-mounted and cut into four quadrants: temporal, nasal, inferior and superior. For cryosection, fixed eye cups were cryoprotected overnight in 30% sucrose solution and embedded in OCT medium (Sakura Finetek, Torrance, CA, USA). Blocks were sectioned by cryostat at 15-20 μm and counterstained with DAPI (Vectashield H-1200, Vector Laboratories, Inc. Burlingame, CA, USA).

Confocal images were taken using a Zeiss LSM800 confocal microscope (Zeiss, Thornwood, NY). For flat-mounted retinas, Z-stack images covering the depth of the retina from the inner nuclear layer (INL) to the ganglion cell layer (GCL; approximately 50-80 μm) were acquired. Lower magnification (5×) pictures were captured for each leaflet of the retina using the tiling/stitch function in Zen (Zen 3.2; Oberkochen, Germany, http://www.zeiss.com/microscopy /en_us/products/microscope-software/zen.html#introduction, RRID: SCR_013672). For cell counting, individual images were captured at 20×, covering an area of 0.102 mm^2. To distinguish the M1 cells in the GCL from the displaced M1s in the INL, individual z-stack images covering an area of 0.0255 mm^2 were taken using a 40× water immersion objective. 3-D reconstruction and vertical view images were done and acquired by Imaris (Imaris 9.6, Bitplane Inc. Concord, MA, http://www.bitplane.com/imaris/imaris, RRID: SCR_007370).

Antibody characterization

Primary antibodies are listed in **Table 1**. The primary polyclonal antiserum (UF006) to melanopsin was raised in rabbit against a synthetic peptide consisting of the 15 N-terminal amino acids of mouse melanopsin (Genbank accession NP_038915) conjugated to keyhole limpet hemocyanin

(KLH). Specificity of this antiserum has been confirmed in control studies showing a dose-dependent loss of immunoreactivity by pre-absorption with the immunogen and by the lack of immunoreactivity in the retinas of melanopsin-null mice (Panda et al., 2002). The lack of immunoreactivity in melanopsin knockout mice was confirmed using the immunoperoxidase method (Panda et al., 2002). We also validated the antibody using the *Opn4*$^{cre/cre}$ mice (Ecker et al., 2010) crossed with a Synaptophysin-tdTomato cre reporter line, Ai34(RCL-Syp/tdT)-D (PubMed ID: J:170755). We found some of tdTomato+ cells are strongly SMI-32 positive and weakly melanopsin positive (data not shown), confirming their identity as M4 cells.

The mouse anti-Brn3a antibody (Millipore, #MAB1585, RRID: AB_94166) was generated against amino acids 186-224 of Brn-3a fused to the T7 gene 10 protein. According to the manufacturer, it does not recognize either Brn3b or Brn3c, nor stains tissues of Brn-3a knockout mice. This antibody labels RGCs in mouse retina (Voinescu et al., 2009), as seen in this study. We also co-labeled Brn3a with rbpms, another general RGC marker, and found that all Brn3a-positive cells were rbpms-positive (**Figure 3a**).

The mouse anti-SMI-32 antibody (Biolegend, #801702, RRID: AB_2715852) specifically recognizes a 200 kD non-phosphorylated epitope in neurofilament H, tested in various mammalian species. Specifically, in retina it labels some retinal ganglion cell bodies, dendrites and axons (Feng, Zhao, et al., 2013).

The rabbit anti-rbpms antibody (Abcam, ab194213) was generated against a synthetic peptide within rat rbpms (N-terminal) conjugated to KLH. In western blots, the rbpms antibody detects the expected 22 kDa band from rat heart lysate (manufacturer's specification). In mouse retina, it specifically labels RGCs (Thomson et al., 2020).

Cell quantification

For general RGC and ipRGC cell counting, mouse retinas were immunostained with anti-rbpms, anti-Brn3a, or anti-melanopsin antibodies. For each retina, at least 24 *en face* z-stack images covering the depth from the GCL to the INL were captured (roughly 50-80 μm of total depth). Six images were acquired for each quadrant to ensure broad coverage of the entire retina (Fig. 1A). A rectangle covering no less than 0.025mm^2 area was randomly drawn on the images and Brn3a-, rbpms-, or melanopsin-positive cells within the rectangle were manually counted in Zen (Zen 3.2; Oberkochen, Germany).

To quantify M4 cells, mouse retinas were double immunostained with anti-SMI-32 and anti-melanopsin antibodies. Images were acquired as described above, and cells were classified as M4 when they met the following three criteria: 1) a cell soma size larger than 200 μm^{2}2) faintly positive label for melanopsin, and 3) strongly positive label for SMI-32.

M1 in the GCL and displaced M1 cells in the INL were counted by taking images at the focal plane of the GCL and INL, respectively. For each retina, a total of 36 *en face* z-stack images were taken, with six images for each quadrant. Three-dimensional reconstruction was done using Imaris software (Imaris 9.6, Bitplane Inc. Concord, MA) and melanopsin-positive cells with dendrites reaching only the off sub-lamina of the IPL were counted as M1 cells. Although M6 ipRGCS also have dendrites reaching the off sub-lamina of the IPL, they are rarely labeled by immunofluorescence, even with amplification, and therefore are unlikely be misidentified as M1 (Quattrochi et al., 2019). Similarly, cells with at least one dendrite terminating in the on sub-lamina of IPL, potentially M3 cells, were not included. Cell density for each retina was calculated using the total number of cells counted divided by the total area.

Circadian behavioral analysis

Animals were housed in individual cages with running wheels in light tight boxes under a 12 hour light:dark (LD) schedule. Fluorescent lights (100 μW/cm^2) were used for illumination, and food and water were provided *ad libitum*. Wheel running was monitored and analyzed with the ClockLab collection and analysis software suite (Actimetrics, Wilmette, IL). After at least 14 days of entrainment to the LD cycle, the dark period was advanced by 6 hours and wheel running was monitored for the following 15 days. The duration of re-entrainment was defined as the number of days required to shift activity onset by 6 hours followed by two consecutive days of activity onset or offset within this range. Activity onset was determined by the ClockLab software and adjusted manually to avoid masking effect. Entrainment was scored manually by a blind observer.

Circadian phase shifting using low intensity light was performed in a similar manner, except during the 12-hour light period, the intensity of the fluorescent source was adjusted to 1.5 $\mu W/cm^2$ by wrapping the fluorescent light bulbs with layers of pliable, semitranslucent neutral density filters.

Animals were also exposed to constant darkness (DD), and the free-running period was calculated according to the onset of activity across at least 10 days in constant darkness. The circadian period was calculated by 24 hours minus the slope of the least square fitted line of the onsets.

All results were expressed as the mean ± SEM. Non-parametric Mann-Whitney tests were performed to compare two groups of samples. All animal procedures were approved by the Institutional Animal Care and Use Committee at University of Virginia and conformed to the guidelines on Use of Animals from the National Institute of Health (NIH).

Results

The general RGC population suffers a significant loss following chronic ocular hypertension.

We performed laser photocoagulation in adult C57BL/6 mice to induce OHT as described previously (Feng, Chen, et al., 2013; Feng, Zhao, et al., 2013)(**Figure 1)**. For unilaterally lasered mice, the right eye was lasered and the left untreated eye of the same mouse was used as a control (**Figure 1a**). We also generated bilaterally lasered mice in order to induce chronic OHT in both eyes for circadian behavioral tests (**Figure 1b**). We tracked the intraocular pressures (IOP) every 2 weeks for the first two months and then every month up to one year, and simultaneously tracked visual acuity of each eye. The unilaterally lasered mice with treated eyes that exhibited consistently elevated IOP for more than three months and showed declining visual acuity were used for cell quantification (**Figure 1a**), while bilaterally lasered mice were used for circadian behavioral tests (**Figure 1b**).

The changes in IOP and visual acuity were tracked over time (**Figure 2**). For the first 3 months post-laser photocoagulation, the IOP of the lasered eye was elevated more than 25% than that of the control eye (**Figure 2a**). Three months post-laser photocoagulation, the IOP of the lasered eye of the unilaterally lasered mice was elevated to 19.15 ± 0.84 mmHg (n=7), significantly higher than that of the non-lasered control eyes (15.31± 0.29 mmHg, n=7, $p<0.01$, Mann-Whitney test, **Figure 2a**). The IOP of the lasered eye gradually dropped and was not significantly different from the control eyes by eight months post-laser surgery (controls: 14.6±0.5 mmHg, n=4; OHT: 18.2± 3.7 mmHg, n=6, p=0.2, Mann-Whitney test). The IOP was also elevated in each eye of the bilaterally lasered mice for more than three months (left panel, **Figure 2b**) and eventually dropped at eight months post-laser photocoagulation (left eye OHT: 15.94±1.18 mmHg, right eye OHT: 15.77±1.54 mmHg, p=0.87, Mann-Whitney test, **Figure 2b**).

Chronic IOP elevation induced a continuous decrease in visual acuity (**Figure 2a**). The acuity of the OHT eyes dropped from 0.35±0.02 c/d (n=11) to 0.28±0.02 c/d (n=6) at eight months post-laser photocoagulation. At the same time, the control eyes' acuity remained within normal range at 0.39±0.01 c/d (n=4) eight months post-laser surgery, significantly higher than the OHT eyes' (p=0.01, Mann-Whitney test) (Chen et al., 2015; Douglas et al., 2005; Feng, Chen, et al., 2013; Prusky et al., 2004).

Next, RGC loss following chronic IOP elevation was quantified. The general RGC population was immunolabeled using antibodies to Brn3a (Xiang et al., 1995) and rbpms (Rodriguez et al., 2014). Previous studies suggested that rbpms is expressed exclusively in most if not all RGCs, while Brn3a is expressed in some RGCs (Feng, Zhao, et al., 2013; Pan, Yang, Feng, & Gan, 2005; Rodriguez et al., 2014). We confirmed the labeling pattern in wild type mice (**Figure 3a).** It was estimated that about 59% of the cells in the GCL are displaced amacrines and 41% are RGCs (Jeon et al., 1998). Indeed, we found that about 48.2% of all cells in the GCL were rbpms-positive RGCs; in addition, all Brn3a-positive cells were rbpms-positive, while about 87% of rbpms-positive cells were Brn3a-positive (**Figrue 3a)**. At six months post-laser photocoagulation, the densities of Brn3a-positive cells were quantified and compared between OHT and control eyes (**Figure 3b, c**). We found that Brn3a-positive RGC density was significantly reduced by 25.6% in OHT eyes compared to controls (controls: 3859.7±156.8 /mm^2, n=5; OHT: 2871.7±94.4 /mm^2, n=3, p=0.04, Mann-Whitney test). At 8-months post-laser photocoagulation, rbpms-positive RGC density was also significantly reduced by 32.6% in OHT eyes compared to the controls (controls: 3942.5±100.4 /mm^2, n=3; OHT: 2658.1±216.0 /mm^2, n=4, p=0.03, Mann-Whitney test) (**Figure 3d, e**). Together our results showed that 6 to 8 months of chronic IOP elevation induced approximately 25-33% RGC loss, consistent with our previous findings (Chen et al., 2015; Feng, Chen, et al., 2013).

Significant loss of ipRGCs occurs following chronic ocular hypertension.

Previously studies, including ours, showed that the RGC degeneration is cell type-specific (Duan et al., 2015; Feng, Zhao, et al., 2013). For instance, ipRGCs have been shown to be relatively resistant to chronic OHT or acute optic nerve damage (Duan et al., 2015; Li et al., 2006). Therefore, we next examined whether ipRGC survival differs from survival of the general RGC population in our chronic model of ocular hypertension. Melanopsin antisera was used to label the majority of ipRGCs, M1 through M4, and possibly some weakly melanopsin-positive M5 and M6 (**Figure 3f, g**) (Quattrochi et al., 2019). We have included all cells immunolabeled with the anti-melanopsin antisera in the GCL and the INL for general ipRGC quantification. Surprisingly, at 8 to 9 months post-laser surgery, we observed a 16.5% reduction in the total ipRGC population in the OHT eyes compared to the control eyes (controls: 219.6±3.0 /mm^2, n=16; OHT: 183.4±4.5 /mm^2, n=11, p<0.001, Mann-Whitney test) (**Figure 3f, h**). We conclude that, like the general RGC population, the ipRGC population also suffers significant degeneration following the chronic hypertension insult, albeit to a lesser extent. Because the ipRGCs are not a homogeneous group and can be further classified into several subtypes, from M1 to M6, each with distinct morphology and function (Do, 2019), we next examined how different ipRGC subtypes survive in the context of chronic OHT.

M4 ipRGCs are susceptible to chronic IOP elevation.

Combining immunohistochemistry and three-dimensional reconstruction of ipRGC morphology, we characterized and quantified several ipRGC subtypes. To identify the M4 ipRGCs, we double-stained retinas with antibodies against melanopsin and the SMI-32 neurofilament epitope (**Figure 4a**). We compared the survival rate of M4 ipRGCs at eight to nine months post-laser photocoagulation. We found that M4 ipRGCs were significantly reduced by 25.7% (controls: 52.2±2.0 /mm^2, n=10; OHT: 38.8±2.7 /mm^2, n= 10, p<0.01, Mann-Whitney test) (**Figure 4b**), similar to the general ipRGC population.

Because M4 ipRGCs are thought to be involved in image-forming vision, especially in contrast sensitivity (Schmidt et al., 2014), we tested the contrast sensitivity of the OHT eyes at the spatial frequencies of 0.103 and 0.192 c/d. We found that the contrast sensitivities were significantly reduced (0.192: p<0.01, and 0.103: p<0.001 in Mann-Whitney test) in OHT eyes compared to control eyes (**Figure 4c**). At 0.103 c/d, the average contrast sensitivity for control eyes was 6.09±0.56, while for the OHT eyes it was 3.15±0.20 (n=12 in each group). At 0.192 c/d, the average contrast sensitivity for the control eyes was 5.50 ± 0.35, while in the OHT eyes it was only 3.63±0.31. This reduction in contrast sensitivity is consistent with the significant loss of general RGCs and M4 ipRGCs.

M1 ipRGCs are resistant to chronic IOP elevation.

Based on 3-D reconstruction of confocal z-stack images of ipRGCs, we identified common M1 ipRGCs with dendrites reaching the OFF sub-lamina of the IPL (**Figure 5a**). A small group of M1 cells also have perikarya located in the INL and thus are called displaced M1 ipRGCs (**Figure 5b**) (Berson et al., 2010; Duda et al., 2020; Ecker et al., 2010). We quantified the common M1 ipRGCs with cell bodies in the GCL and the displaced ipRGCs separately. Interestingly, we found that the density of M1 ipRGCs in the GCL did not change significantly at 8 months post-IOP elevation compared to controls (controls: 54.4±3.1 /mm^2, n=3; OHT: 56.4±1.1 /mm^2, n=4 p=0.86, Mann-Whitney test) (**Figure 5c**). Similarly, we found no significant change in the density of displaced M1 ipRGCs (OHT: 6.7±1 /mm^2, n=12; controls: 7.0±0.7 /mm^2, n=16, p=0.66, Mann-Whitney test) (**Figure 5d**). Taken together, the M1 ipRGC population suffered little, if any, cell loss following chronic ocular hypertension.

Circadian re-entrainment and circadian rhythmicity remain largely intact in OHT mice.

Given that M1 ipRGCs are known to innervate the master circadian clock in the hypothalamic suprachiasmatic nucleus (SCN) (Baver et al., 2008; Chen et al., 2011; Hattar et al., 2002; Jain et al., 2012), and M1 ipRGCs are preferentially spared from damage in OHT mice, we tested the hypothesis that the circadian behaviors may remain largely unaffected in glaucomatous mice. We performed bilateral laser photocoagulation on both eyes of C57BL/6 mice, and then tracked the IOP, visual acuity, and contrast sensitivity for up to one year. Mice that showed sustained IOP elevation for more than three months for both eyes (**Figure 2b**) were used for circadian studies. Out of more than 40 mice upon which we performed bilateral laser surgeries, six met this criterion for circadian testing (**Figure 1b**).

At seven months post-laser photocoagulation, six bilaterally lasered mice and six age-matched control mice were transferred to individual cages equipped with running wheels and maintained in a 12-hour light:dark (LD) schedule. The mice were allowed to adapt for 10 days in the running wheel cages. We observed clear onsets of activity immediately after lights-off in both control and bilaterally lasered mice (**Figure 6a**). We then advanced the dark phase of the LD cycle by six hours and monitored the wheel running behavior for 15 days. The entrainment was scored by a blind observer where re-entrainment was quantified as the number of days required to achieve a stable phase of entrainment to the advanced light cycle followed by two consecutive days of similar phase. Surprisingly, we found that the bilaterally lasered mice entrained significantly faster than control mice (controls: 8.8±0.5 days, n=6; OHT: 6.7±0.7 days, n=6, p=0.049, Mann-Whitney test) (**Figure 6a, b**). To confirm this result, we performed another round of phase advance and found similar results (controls: 7.5±0.4 days, n=6; OHT: 5.8±0.5 days, n=6, p=0.04, Mann-Whitney test).To test whether sensitivity of photoentrainment was altered, we performed a shift where the light intensity was reduced 60-fold from 100 μW/cm^2 to 1.5 μW/cm^2 (**Figure 6c**). We found no significant difference in the number of days required for re-entrainment between control and the bilaterally lasered mice (controls: 8.8±0.5 days, n=6; OHT: 7.8±0.7 days, n=6, p=0.22, Mann-Whitney test) (**Figure 6d**).

We next tested whether the difference observed in re-entrainment rate is caused by a difference in circadian periods. The same animals were maintained under constant darkness for at least 2 weeks and the stable free-running period was calculated across at least 10 days for each mouse (**Figure 6e**). We found no significant difference in circadian period between the control and bilaterally lasered mice (controls: 23.6±0.02 hours, n=6; OHT: 23.6±0.02 hours, n=6, p=0.81, Mann-Whitney test) (**Figure 6f**).

After the circadian experiments (about 11 months post-laser surgery), we examined the visual acuity (**Figure 7a**) and contrast sensitivity (**Figure 7b**) of the experimental and control animals. The OHT mice exhibited a significantly reduced contrast sensitivity: At 0.103 c/d, the contrast sensitivity of OHT mice (n=12 eyes) was 3.06±0.18, and that of controls (n=12 eyes) was 5.56±0.49 ($p<0.001$, Mann-Whitney test). At 0.192 c/d, the contrast sensitivity of OHT mice (n=12 eyes) was 3.28±0.18, and that of controls (n=12 eyes) was 5.53±0.69 ($p<0.001$, Mann-Whitney test). Similarly, the visual acuity of OHT mice was significantly reduced compared to controls, which remained high (controls: 0.36 c/d, n=12; OHT: 0.28±0.01 c/d, n=12; $p<0.001$, Mann-Whitney test).

Finally, we analyzed the overall morphology of the retinas (**Figure 7c**). The laminar structure was largely normal in OHT eyes. As expected, we observed a decrease in RGC density as determined by rbpms labeling in the OHT retina (**Figure 7d**). We quantified two OHT retinas and the overall density of the rbpms-positive cells in the OHT eyes was approximately 1674 cells/mm^2 at twelve months post laser photocoagulation, a 54.8% reduction compared to the control retina (3700 cells/mm^2, n=1). Similarly, the density of melanopsin-positive ipRGCs was also reduced (**Figure 7e**) to 182.5 cells/mm^2 (n=2), 13.5% lower than the control retina (211 cells/mm^2, n=1).

Discussion

Characterization of general RGC population and ipRGC subtypes

Rbpms is a general RGC marker that is expressed by most, if not all, RGCs in mouse retina (Rodriguez et al., 2014). We found that the anti-rbpms antibody labeled about half of all cells in the GCL, s previously reported (Jeon et al., 1998). The other general RGC marker we used in this study, Brn3a, is present in 87% of all rbpms-positive RGCs (**Figure 3a)**. We further assessed the general ipRGC population identified by the melanopsin antibody, which immunolabeled M1 through M4 (and possibly some M5) (Quattrochi et al., 2019; Stabio et al., 2018). We calculated a density of 219.6 cells/mm^2, which can be extrapolated to about 2800 cells per retina. This number agrees with a previous report of an estimated 2600 ipRGCs (Berson et al., 2010).

A total of six different ipRGC subtypes have been characterized, each with distinct morphology, physiology, and functions (Do, 2019; Duda et al., 2020). In the control retina, we calculated a density of 52.2 cells/mm^2 of M4 cells by anti-SMI32 and anti-melanopsin antibodies. In one study by Schmidt and colleagues (Schmidt et al., 2014), an average of 571.6 total M4 cells were found in mouse retinas, which translates to about 45 cells/mm^2. Similar results were confirmed by another study where a total of 529 M4 cells were observed (Sonoda, Li, et al., 2020). We further classified displaced M1 cells by their specific dendritic lamination in the OFF sublamina of the IPL, similar to the M1 ipRGCs with perikarya in the GCL. We have calculated densities of 54.4 cells/mm^2 and 6.7 cells/mm^2 for M1 cells and displaced M1 cells, respectively. The total number of M1 cells is 54.4+6.7 = 61.1 cells/ mm^2, which agrees with the previous finding by Berson and colleagues that the density of the total M1 cells was 63 cells/mm^2 (Berson et al., 2010). Together, our data show that these markers can assess accurately the general RGC population and ipRGC subtypes, thus enabling us to further examine their survivals in mice with chronic ocular hypertension.

Subtype-dependent ipRGC degeneration in OHT mice

Glaucoma is characterized by progressive RGC cell degeneration and death (Chen et al., 2015; Feng, Chen, et al., 2013; Quigley, 2016). We observed a 25.6% cell loss of Brn3a-positive RGCs and a 32.6% reduction in rbpms-positive RGC density 6 to 8 months post-laser photocoagulation. Many studies have shown that ipRGCs are resistant to various disease insults (Chen et al., 2014; Duan et al., 2015; Tran et al., 2019). For example, in a chronic OHT model in rats, no substantial ipRGCs loss or change in dendritic arbor structure could be found after 3 months of sustained elevation of IOP, while a significant number of superior colliculus projecting RGCs degenerated (Li et al., 2006). In a mouse optic nerve crush model, ipRGCs also have been found to preferentially survive relative to other RGC types (Duan et al., 2015; Tran et al., 2019). Our results show that with chronic IOP elevation the general ipRGCs (all M1-M4, possibly some M5 and M6) density was reduced 16.5%, which is less than the 30% loss of the general RGC population.

The survival of ipRGCs may not be uniform among different subtypes. At 14 days post-optic nerve crush injury, only a small number of M2 cells survived, but over 70% of M1 cells and over 80% of alpha RGCs labeled in a Kcng4-YFP transgenic line, including the M4 ipRGCs, survived (Duan et al., 2015). At 60-days post optic nerve transection in rats, M1 cells comprised about 80% of all surviving RGCs (De Sevilla Müller et al., 2014). We also found no significant loss in M1 cells and displaced M1 cells in OHT mice, however, M4 cells suffered 25.7% loss. Other ipRGC subtypes, including M2s and possibly some M5 and M6s, also suffered about 23% cell loss (**table1**). This inconsistency may be explained by the different methods applied for RGC subtype categorization, as well as the differential survival of each subtype in different animal models. For example, Tran et al (2019) quantified RGCs from single cell samples dissociated from whole retinas, which provides a comprehensive profile of RGC survival, but may also cause disproportionate representation of RGC types (Tran et al., 2019). Additionally, optic nerve crush injury or transection is an acute model of RGC damage, analyzed within a couple weeks of crush, while chronic OHT induces slow and progressive RGC loss over months. Therefore, RGCs may respond differently to different types of disease insult (McKinnon et al., 2009). Interestingly, melanopsin overexpression in RGCs promoted axonal regeneration by activating the mammalian target of rapamycin (mTOR) pathway (Li et al., 2016). Taken together, we found that ipRGCs survived well with chronic OHT and this survival is subtype dependent. More work is needed to better understand the underlying molecular mechanisms of protection, degeneration, and regeneration which, in turn, will offer insights to develop neuroprotective treatments of glaucoma.

Behavioral consequences of chronic OHT on circadian entrainments and visual acuity

As discussed, ipRGCs are involved in a broad range of image forming and non-image forming functions (Do, 2019; Duda et al., 2020; Lucas et al., 2020). Thus, we further investigated how the subtype-specific loss of ipRGCs affects visual behaviors in mice suffering chronic OHT insult. It has been shown that M4 cells project to dLGN (Estevez et al., 2012) and contribute to contrast sensitivity aspects of image forming vision with and without rods/cones inputs (Ecker et al., 2010; Schmidt et al., 2014; Sonoda, Li, et al., 2020).

Specifically, following ablation of several ipRGC subtypes including the M4s, contrast sensitivity was significantly reduced at various spatial frequencies (Schmidt et al., 2014). The authors also observed that spatial frequencies at which significant deficits were found in these mice matched the spatial frequencies (0.05 and 0.09 c/d) to which M4s respond most strongly in isolated retina (Estevez et al., 2012), suggesting that M4s could contribute to contrast sensitivity. In the current study, we found a significant decrease in contrast sensitivity, which is also correlated with the significant loss of M4 cells in OHT eyes. Similarly, we also observed that our OHT mice exhibited greater reduction of contrast sensitivity at 0.103 c/d than 0.192 c/d (Figure 4c). Yet we cannot exclude that degeneration of other non-M4 RGCs may contribute to the change in contrast sensitivity in the OHT mice (Baden et al., 2016a; Khani & Gollisch, 2017). M1 cells, on the other hand, project to the suprachiasmatic nucleus (SCN), the master clock that regulates circadian photoentrainment, a non-image forming function (Baver et al., 2008; Do, 2019; Vadnie & McClung, 2017). With little M1 loss under chronic OHT, we found no delay in circadian re-entrainment between non-ocular hypertensive controls and OHT mice.

Note that when mice were subjected to a phase advance of a relatively bright LD cycle, the OHT mice established a stable phase of entrainment significantly faster than the age-matched controls. In a similar study using a rat OHT model, the authors found the opposite result where it took significantly more time for the OHT rat to re-entrain after phase advance (Drouyer et al., 2008). They also observed a significant reduction in RGC terminals in the SCN. These differences could be attributed to the intensity and duration of IOP elevation which may induce a different severity of RGC cell death. For example, IOP had been doubled for over 4 months in the rat glaucoma model, which led to a 50-70% reduction of RGC axon terminals in a majority of visual and non-visual centers in the brain (Drouyer et al., 2008). By contrast, our mouse model exhibited a mild IOP elevation (about 20-30% increase) for a longer duration (from 3 months to up to a year).

The accelerated re-entrainment observed in mice with elevated IOP relative to normotensive controls was unexpected. We hypothesize that even a slight reduction of the direct photic input into the hypothalamus may cause an increase in the desynchrony among the cellular oscillators of the SCN. Such desynchrony speeds circadian entrainment in response to a shifted LD cycle. For example, the administration of vasoactive intestinal peptide (VIP) induces desynchrony or “phase tumbling” among SCN oscillator cells. If VIP is given prior to a shift in the LD cycle, the number of days required to re-entrain is halved compared to mice receiving vehicle injections (An et al., 2013). Although we did not observe a reduction in M1 cells in our bilaterally lasered mice, it remains possible that the synaptic input from M1 cells to the SCN was damaged under prolonged elevated IOP. In addition, the expression level of melanopsin as well as melanopsin activity could also affect re-entrainment rates. Melanopsin knockout mice exhibit reduced phase-shifting responses (Panda et al., 2002). The lack of C-terminal phosphorylation sites of the melanopsin molecue may also lead to faster re-entrainment (Somasundaram et al., 2017). Alternatively, we observed a decrease in M4 cells which project to the intergeniculate leaflet (IGL) (Ecker et al., 2010). The IGL, in turn, encodes irradiance and sends a projection to the SCN via the geniculohypothalamic tract (Morin, 2013; Yuan et al., 2018). Therefore, the degeneration of M4 cells could affect the IGL's modulation of the retinal input to the SCN and indirectly impact its behavioral output (Hanna et al., 2017).

The disruption of the circadian system observed in animal glaucoma models are also observed in patients. Primary open angle glaucoma (POAG) and primary angle-closure glaucoma (PACG) patients often suffer mood and sleep disorders, and the severity is correlated with visual field impairment (Ciulla et al., 2019; Wang et al., 2013). Sleep efficiency assessed by polysomnographic recordings was significantly lowered (Gracitelli, Duque-Chica, et al., 2015), and blood melatonin levels are higher in early morning in POAG patients (Ma et al., 2018). It will be of great interest to further understand the ipRGC-mediated neural circuits that account for the behavioral changes suffered by glaucoma patients. Such an understanding will lead to improved patient care and treatment as glaucoma develops and progresses.

Figures

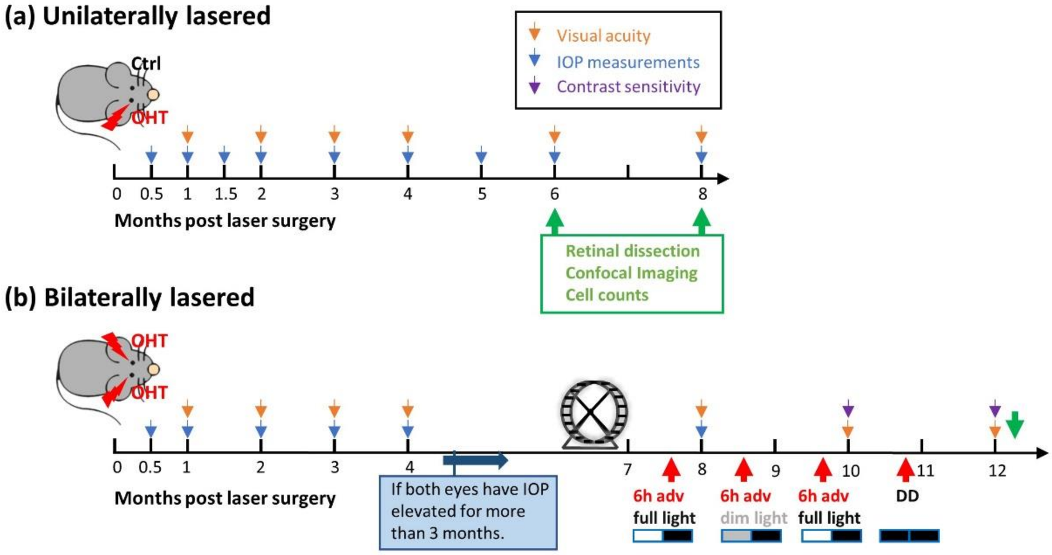

Figure 1. Experimental design to investigate ipRGC survival and its functional consequences in laser-induced ocular hypertensive (OHT) mice. (a) Unilaterally lasered mice were generated for cell quantification. OHT was induced in one eye while the other eye of the mouse was used as a control. (b) Bilateral OHT was induced in both eyes of a mouse for circadian behavioral tests. Mice that had IOP consistently elevated for more than three months were subjected to three rounds of phase advances (red arrows) in the light period of light: dark cycle. Free run under constant darkness (DD) were performed to assess circadian periods at the end. Intraocular pressure (IOP) (blue arrows), visual acuity (orange arrows), and contrast sensitivity (purple arrows) were assessed regularly. Adv: advance.

(a) **Unilaterally lasered**

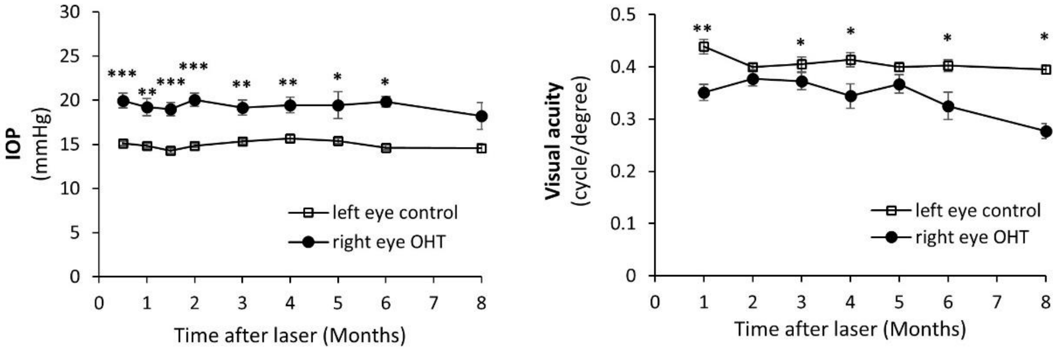

(b) **Bilaterally lasered**

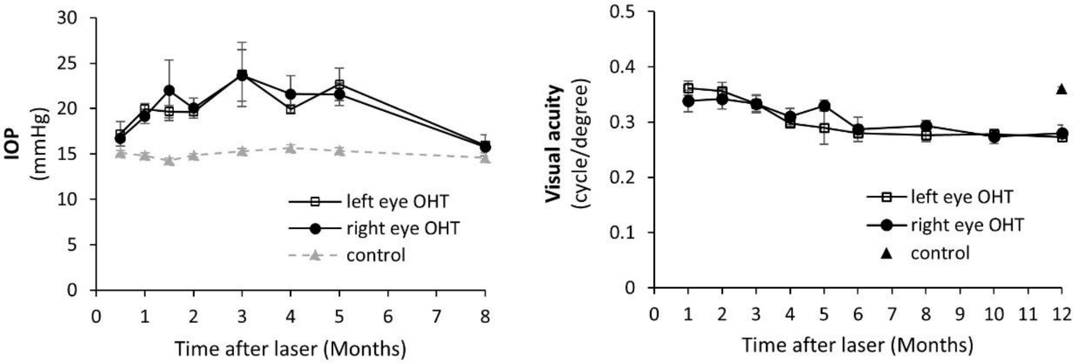

Figure 2. Chronic IOP elevation led to decreased visual acuity. (a) For unilaterally lasered mice, the IOP of the OHT eye was elevated for more than 3 months while that of the control eye remained constant (left). With chronic IOP elevation, the visual acuity of the OHT eye continued to decrease while that of the control eye remained relatively stable (right). n = 4-13 in each group. (b) For bilaterally lasered mice, the IOP of both OHT eyes (left) remained elevated for more than 3 months. The IOP of control eye from unilaterally lasered mice was shown in gray (dashed line) for purpose of comparison. With chronic IOP elevation, the visual acuity (right) of both eyes continued to decrease. The visual acuity of age matched untreated control mice was shown (black triangle). n = 4-11 in each group. *: $P < 0.05$; **: $P < 0.01$; ***: $P < 0.001$. in ‘Mann-Whitney test. Data presented as Mean ± SEM. If no asterisk, not significant.

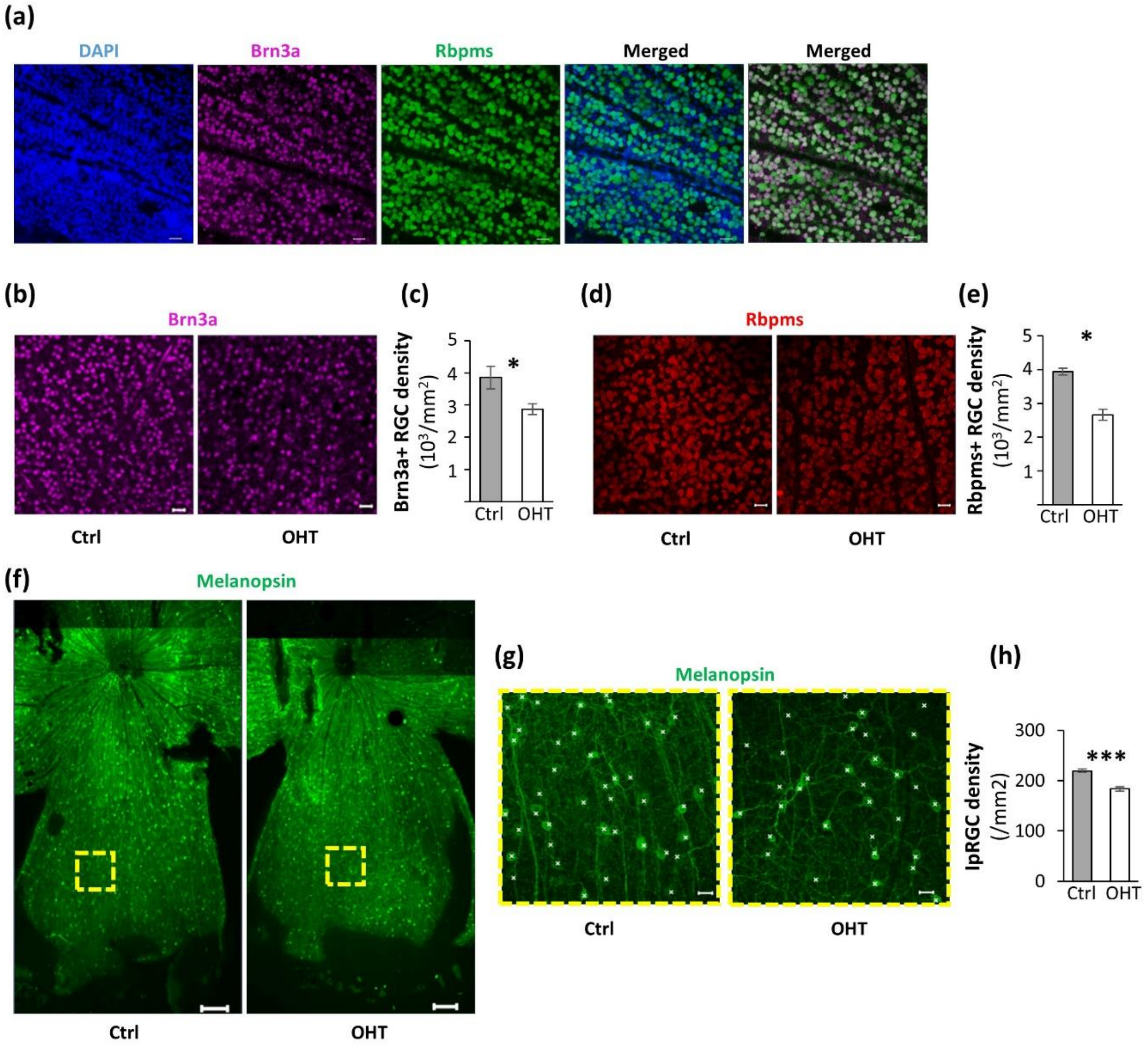

Figure 3. General RGC population and ipRGCs suffered significant loss in OHT mice.

(a) Flat mounted retinas of 8-month-old wt mice stained with DAPI (blue), Brn3a (purple), and rbpms (green). Almost all Brn3a-positive cells were rbpms-positive and roughly 90% of rbpms-positive cell were Brn3a-positive. (b) Flat-mounted retinas of a control and an OHT 6-8-months post laser surgery were immunostained with Brn3a (b) or rbpms (d) antibodies for the general population of RGCs. Quantification of Brn3a-positive cells (c) and rbpms-positive cells (e) were shown between control and OHT retinas. (f) Flat mounted images of the temporal leaflet of a control (left) and an OHT (right) retina stained with anti-melanopsin antibody. (g) The high-magnification images of ipRGCs in the GCL (yellow rectangles in f) were used for cell counting.

White crosses denote ipRGC somas. (h) Quantification of melanopsin-positive ipRGCs. *: P<0.05; ***: P<0.001 in Mann-Whitney test. Scale bar for (a, b, d, and g) is 20 µm and for (f) is 200 µm.

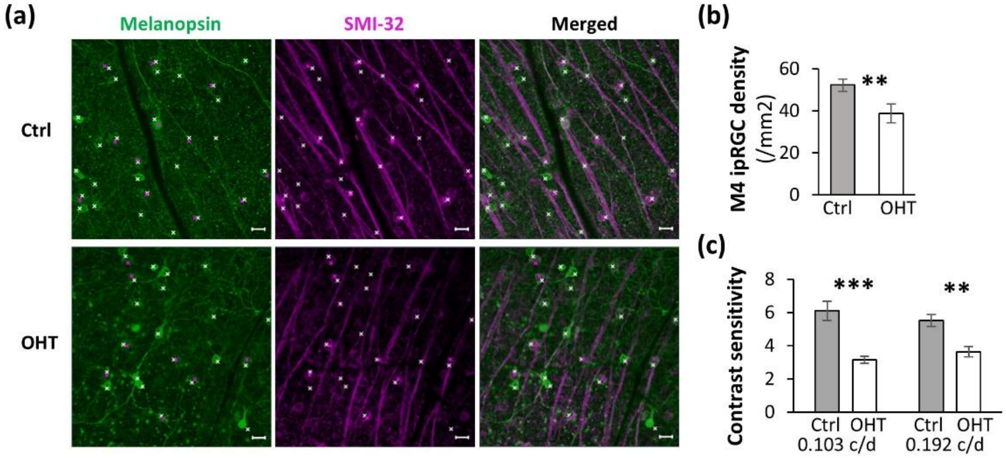

Figure 4. M4 ipRGC suffered significant loss following the chronic IOP elevation. (a) Confocal images of flat mounted retinas from a control eye and an OHT eye eight-months post laser surgery immunostained with melanopsin and SMI-32 antibodies. White crosses denote melanopsin-positive cells and violet crosses denote large cells positive for both melanopsin and SMI-32. Scale bar is 20 µm. (b) Quantification of M4 cell density in control and OHT retinas. (c) Contrast sensitivity measured at 0.103 and 0.192 cycle per degree (c/d) of control and OHT group eight-months post laser surgery. **: P < 0.01; ***: P < 0.001 in Mann-Whitney test. Data presented as Mean ± SEM.

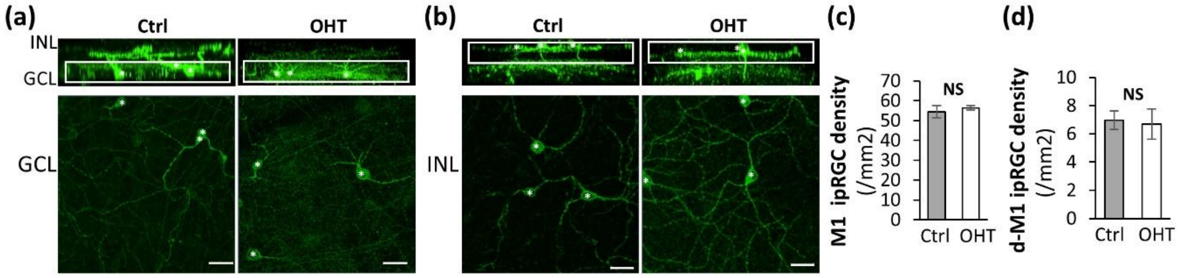

Figure 5. M1 ipRGC is resistant to the IOP elevation. (a) Identification of M1 ipRGCs by their dendritic patterning and location of somas. Z-stack confocal images of the flat-mounted retinas were projected to 2-D images are shown at the bottom. The extrapolated vertical view was shown on the top. White rectangles mark the ganglion cell layer (GCL). INL: inner nuclear layer. (b) Displaced melanopsin-positive cells in the INL. While rectangles mark the INL. Scale bar is 20µm. (c-d) Quantifications of M1 density (c) and displaced M1 density (d). NS: not significant in Mann-Whitney test. Data presented as Mean ± SEM.

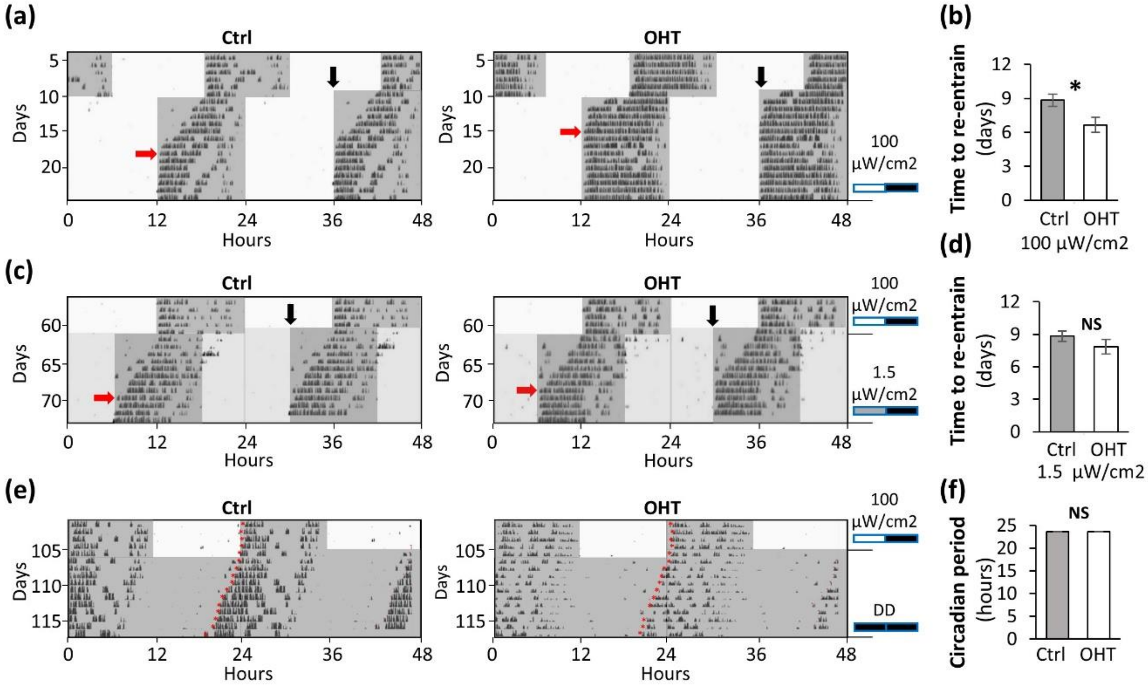

Figure 6. OHT mice exhibited a largely normal circadian re-entrainment behavior. (a) Examples of double plot actograms for a wt control and a bilaterally lasered mouse (OHT) under bright light intensity (a) or low light intensity (c) during light portion of the light: dark cycle. Six-hour phase-advance was performed to assess re-entrainment. White and light gray backgrounds indicate the light portions, and the dark gray backgrounds indicate the dark portions of the light: dark cycle, respectively. Red arrows point to the day when re-entrainment was observed. Black arrows point to the light shift. (b, d) Quantification of the average days it took for mice to re-entrain to the new light: dark cycle after phase-advance. (e) Examples of double plot actograms of circadian free run under constant darkness (DD) after day 105. Red asterisks mark the onset of activity on each day. (f) The average free running circadian periods for control and OHT mice. NS: Not significant; *: $P < 0.05$ in Mann-Whitney test. Data presented as Mean ± SEM.

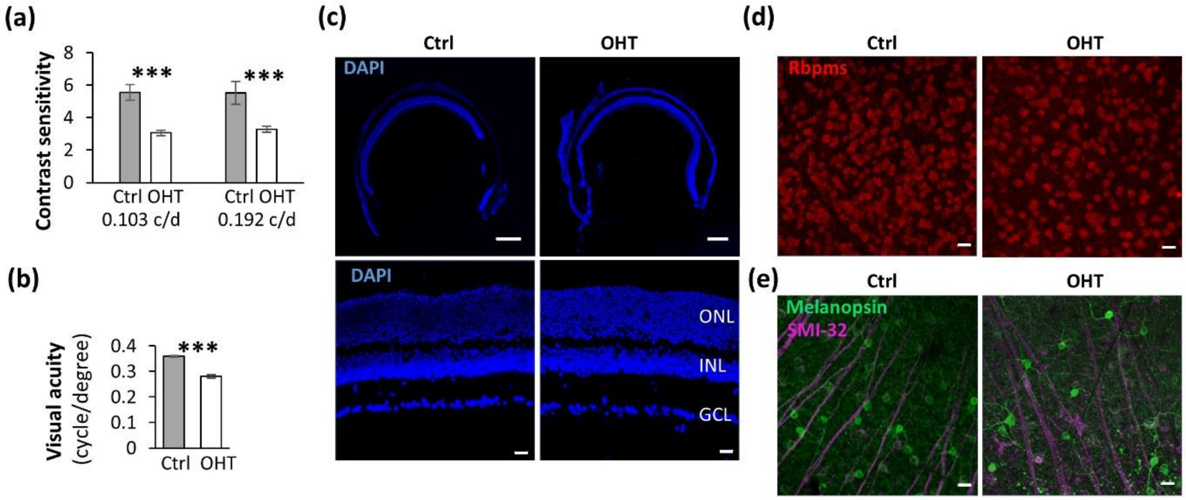

Figure 7. The overall retinal morphology was largely normal by eleven months post laser surgery, despite observed reduction in RGC density. (a-b) Contrast sensitivity (a) and visual acuity (b) of control and OHT mice 11-months post laser surgery. (c) Cross sections of control and bilaterally lasered OHT eye cups eleven-months post laser surgery. Scale bar is 500 µm. Representative higher magnification images were shown below. Scale bar is 50µm. (d-e) Flat mounted retinas of control and OHT retina were stained with rbpms antibody (d) and antibodies against SMI-32 and melanopsin (e). Scale bar is 20µm. ***: P < 0.001 in Mann-Whitney test. Data presented as Mean ± SEM.

Table 1 Primary antibodies used in this study

Antibody	**Immunogen**	**Source (RRID number)**	**Dilution factor**
Melanopsin	15 N-terminal amino acids of mouse melanopsin	Iggy Provencio (Panda et al., 2002), Rabbit monoclonal	1:2000
Brn3a	Amino acids 186-224 of Brn-3a fused to the T7 gene 10 protein	Millipore, MAB1585, (RRID: AB_94166), mouse monoclonal	1:125
SMI-32	Neurofilament H	Biolegend, 801702, (RRID: AB_2715852), mouse monoclonal	1:250
rbpms	Synthetic peptide within Rat RBPMS (N terminal) conjugated to Keyhole Limpet Haemocyanin (KLH)	Abcam, ab194213, rabbit polyclonal	1:500

Table 2 Summary of RGC Density in OHT and Control Mice

RGC type	**Cell density (/mm^2)** mean ± SEM (n)		**Percentage change**
	Control	**OHT (6-9m post laser photocoagulation)**	
rbpms	3942.5 ± 100.4 (3)	2658.1 ± 216.0 (4)	-32.6
Brn3a	3859.7 ± 156.8 (5)	2871.7 ± 94.4 (3)	-25.6
Melanopsin	219.6 ± 3.0 (16)	183.4 ± 4.5 (11)	-16.5
M1	54.4 ± 3.1 (3)	56.4 ± 1.1 (4)	3.4
Displaced M1	7.0 ± 0.7 (16)	6.7 ± 1.0 (12)	- 4.2
M4 (SMI-32+Melanopsin)	52.2 ± 2.0 (10)	38.8 ± 2.7 (10)	-25.7
M2, M3 and some M5, M6	106.0†	81.5 †	-23.1

†: Numbers are based on calculations, not direct cell counts.

Chapter 3 Longitudinal analysis of retinal ganglion cell damage at individual axon bundle level in mice using visible-light optical coherence tomography fibergraphy

Marta Grannonico[1, *], David A. Miller[2, *], Jingyi Gao[1, *], Kara M. McHaney[1], Mingna Liu[1], Michael Krause[3], Peter A. Netland[3], Hao F. Zhang[2, †], Xiaorong Liu[1, 3, 4, 5 †]

[1] Department of Biology, University of Virginia, Charlottesville, VA

[2] Department of Biomedical Engineering, Northwestern University, Evanston, IL

[3] Department of Ophthalmology, University of Virginia, Charlottesville, VA

[4] Program in Fundamental Neuroscience, University of Virginia, Charlottesville, VA, USA

[5] Department of Psychology, University of Virginia, Charlottesville, VA

***** These authors contributed equally to this work.

† Corresponding authors: Hao F. Zhang: hfzhang@northwestern.edu and Xiaorong Liu: xl8n@virginia.edu

Financial Interest Statement: H. F. Z. has financial interests in Opticent Health, which did not support this work. M. G., D. A. M., J. G., K. M. M., M. L., M. K., P. A. N., and X. L. have no conflict of interest.

Acknowledgments

This work was supported in part by NIH grants R01EY026078, R01EY029121, R01EY019949, R01EY026286, U01EY033001, and R44EY026466. We thank William Tucker and Taylor Byron for their technical support with quantification of axon bundles and RGC somas. We also thank Prof Ignacio Provencio for his insightful discussions.

Abstract

In optic neuropathies, such as glaucoma, and neurodegenerative diseases, such as Parkinson's disease and Alzheimer's disease, vision loss is often associated with loss of retinal ganglion cells (RGCs) and their axons. Taking glaucoma as an example, timely management is vital to preserving vision long-term; however, detecting RGC damages at the earliest stages and identifying damage progression continues to be a substantial clinical challenge that depends on disease severity. We previously established visible-light optical coherence tomography fibergraphy (vis-OCTF), a technique for directly visualizing and quantifying RGC axon bundles in mouse retinas *in vivo*, and validated vis-OCTF findings by *ex vivo* using confocal microscopy. In this study, we further developed a new analytic tool to longitudinally track individual axon bundles following the acute optic nerve crush injury (ONC) in mice. We analyzed four parameters: lateral width, bundle height, cross-sectional area, and the shape of individual bundles. Our results showed that axon bundles became wider and thicker at 3-days post ONC, followed by a significant reduction in cross-sectional area and lateral width at 6-days, and reduction in bundle height at 9-days post ONC. Early bundle swelling at 3-days post ONC correlated with about 15% RGC soma loss, and bundle thinning at 9-days post ONC correlated with about 68% RGC soma loss. Both experimental and simulation results suggest that the cross-sectional area of individual RGC axon bundles is a more sensitive indicator for RGC soma loss than the bundle width and height. Taken together, we demonstrate that the size transformation of RGC axon bundles monitored by vis-OCTF could serve as an *in vivo* biomarker for RGC damages, which sets the foundation for translating vis-OCTF findings from animal models to clinical care.

Introduction

Retinal ganglion cell (RGC) loss is a hallmark sign of optic neuropathies, such as glaucoma (Fan & Wiggs, 2010; Quigley, 2016; Smith et al., 2017), and neurodegenerative diseases that affect vision, such as Parkinson's and Alzheimer's disease (Morgia et al., 2017; Snyder et al., 2021). Thus, recognizing RGC loss at its earliest stage is crucial to prevent further irreversible vision loss (Gracitelli, Abe, et al., 2015; Quaranta et al., 2016; Welp et al., 2016). With current clinical diagnostic methods unable to detect RGC loss at the cellular level, functional and structural diagnostic methods are employed to indirectly assess RGC health (Geevarghese et al., 2021; Stein et al., 2021). For example, an important parameter for glaucoma diagnosis is visual field (VF) deficits, though more than 30% of RGCs may be lost before it can be detected by VF testing (Harwerth et al., 2010; Kerrigan-Baumrind et al., 2000; Quigley et al., 1981; Schuman et al., 2020; Wollstein et al., 2012). Characteristic changes in the optic nerve head (ONH) and optic disc are also used for glaucoma diagnosis, but identification of damage can be subjective, and grading varies between observers (Jampel et al., 2009). Of the clinically relevant noninvasive imaging methods (Anton et al., 1997; Da Pozzo et al., 2009; Wollstein et al., 1998; Wollstein et al., 2000), optical coherence tomography (OCT) is most widely used for the diagnosis and monitoring of optic neuropathies. OCT's cross-sectional imaging capabilities enable measurement of the retinal nerve fiber layer (RNFL) and ganglion cell – inner plexiform layer (GCIPL) thickness in vivo as indirect indicators of RGC health (Hou et al., 2018; Schuman et al., 2020; Tatham & Medeiros, 2017). However, inconsistent axial resolution (5 μm to 10 μm) and segmentation algorithms among clinical devices introduce measurement variability that make estimates of RGC health less reliable (Dong et al., 2017; Yang et al., 2015). Moreover, great variability in RGC density and RNFL thickness exists across the population, and individuals may exhibit very different patterns of disease progression, emphasizing the need to monitor individual patients longitudinally (Hou et al., 2018; Shin et al., 2017). RNFL thickness of healthy human subjects varies from 50 to about 120 μm as measured by OCT (Alasil et al., 2014). Overlaps between RNFL ranges were also observed between healthy subjects and glaucoma patients (Alasil et al., 2014). Shin and colleagues followed 292 eyes of 192 patients with primary open-angle glaucoma (POAG) and found that only 72 eyes (24.7%) showed progressive GCIPL thinning, and among the 72 eyes, 41 eyes showed progressing visual field (VF) loss (Shin et al., 2017). In our own studies, we also observed 38% RGC axon loss at 3-5 days after optic nerve crush (ONC) injury in mice before a significant reduction in overall RNFL thickness in mice (Li et al., 2020; Yi et al., 2016). In addition, the ganglion cell layer (GCL) contains non-RGC cells, such as displaced amacrine cells, and the inner plexiform layer (IPL) contains synaptic connections among different retinal cell types in rodent and primate eyes (Jeon et al., 1998). Displaced amacrine cells, which vary from 30% to 80% in the GCL, are largely unaffected by glaucoma (Quigley, 2016). In other words, the RNFL or GCIPL thinning is not a specific indicator to reflect RGC damage. Therefore, there is need for more accurate and sensitive biomarkers for RGC damages following disease insult.

We recently applied visible-light OCT (vis-OCT), which operates from 510 nm to 610 nm and reaches an axial resolution of 1.3 μm in the mouse retina (Miller et al., 2020; Shu et al., 2017). In the visible-light spectral range, optical scattering contrast in biological tissue is much higher than in the near-infrared (NIR) range (Miller et al., 2020). As a result, vis-OCT offers visualization of unique anatomical features and functional imaging capabilities that improve RGC damage evaluation (Shu et al., 2017). We developed vis-OCT fibergraphy (vis-OCTF) to visualize and quantify changes in individual RGC axon bundles in mice (Grannonico et al., 2021; Miller et al., 2020). It yet remains to be determined whether and how the structural changes of individual RGC axon bundles correlate with RGC soma loss with disease progression.

In this study, we applied vis-OCTF to identify individual RGC axon bundles and further quantified four parameters of bundle morphology: (1) lateral width, (2) bundle height, (3) cross-sectional area, and (4) bundle shape. Following ONC injury, we correlated the in vivo changes in RGC axon bundle morphology with RGC soma loss using confocal microscopy. Lastly, we used the experimental data we collected to create a simulation to determine which parameter is most sensitive and estimate each parameter’s floor value – a threshold at which no further change is observed (Bowd et al., 2017; Mwanza et al., 2015). Our study thus builds on the foundation of our previous studies to establish a new quantifiable biomarker for RGC loss in vivo.

Results

Establishing a new analytic tool for identifying and tracking individual axon bundles *in vivo*

Taking advantage of the improved axial resolution offered by vis-OCTF and associated data processing methods (Miller et al., 2020), we established an analytic tool for tracking changes in individual RGC axon bundles in vivo. Briefly, four vis-OCT volumes were acquired from the same eye with the optic nerve head (ONH) aligned to each of the four corners of the field of view. This minimized the curvature of the eye and maximized reflectance of the RNFL (Miller et al., 2020). **Figure 1A** shows one of the four processed vis-OCT fibergrams from a wildtype mouse. The red arc shows the path of a resampled circumpapillary scan centered at ONH (**Fig. 1B**) with two example RGC axon bundles (1) and (2) labeled. The width of each bundle was measured using the signal intensity profile, as shown in **Fig. 1C**, which gives 24.95 µm for bundle (1) and 11.68 µm for bundle (2). The resampled circumpapillary B-scan reconstructed at 425µm radius from the ONH shows the cross-sectional view of axon bundles (1) and (2), as indicated by the dashed green lines. The bundle height was measured using the normalized intensity peaks (**Fig. 1D**), which give 19.73 µm for bundle (1) and 12.77 µm for bundle (2), respectively.

Assuming RGC axon bundles have an ellipsoidal cross section, we calculated the cross-sectional area. As summarized in Fig. 1E, the areas of the axon bundles (1) and (2) are 386 µm^2 and 117 µm^2, respectively. We also developed a dimensionless indicator for the shape of axon bundles, which normalizes the bundle width to height ratio between -1 and +1. A wider axon bundle, like bundle (1), reflects a positive shape value ($S_{b1} = 0.21$); whereas a thicker axon bundle, like bundle (2), reflects a negative shape value ($S_{b2} = - 0.08$). Altogether, we established four parameters to detect changes in axon bundle morphology: width, height, area, and shape.

In vivo Tracking and quantification of RGC axon bundles following the ONC

We next applied vis-OCTF to examine the structural changes at the single axon bundle level following ONC. Figure 2A shows example fibergrams and circumpapillary B-scans of a mouse retina acquired at baseline (before ONC), 3-days (d), 6-d, 9-d, and 15-d post ONC (pONC). The red arc indicates the path of the reconstructed circumpapillary B-scan at 425 µm from the ONH. Magnified and aligned views of the fibergrams, indicated by blue boxes in the middle panel, show the same group of axon bundles tracked over time (**Fig. 2A**). The right panels show the resampled circumpapillary scans of the axon bundles at the same location. We labeled and tracked five axon bundles (1-5). At baseline, the five axon bundles exhibited diverse width, height, area, and shape (top panel of **Fig. 2A**). Following ONC injury, the lateral width of bundle 1 (blue) increased from 23.5 µm before ONC to 25.0 µm at 3-d, and then progressively decreased to 19.9 µm at 6-d, 15.2 µm at 9-d, and 13.7 µm at 15-d pONC (**Fig. 2A-B**). Interestingly, the height of bundle 1 increased from 11.6 µm before ONC to 20.3 µm at 3-d and 20.6 µm at 6-d pONC, and then decreased to 14.5 µm at 9-d pONC. By contrast, the width of bundle 4 (green) continued to decrease from 23.6 µm before ONC to 21.3 µm at 3-d, to 20.4 µm at 6-d, to 18.0 µm at 9-d, and 16.0 µm 15-d pONC. The height of bundle 4 increased from 10.3 µm before ONC to 16.8 µm at 3-d pONC and decreased to 15.7 µm at 6-d pONC.

The cross-sectional bundle area presented an overall clear pattern of increase-decrease for bundles 1 and 4, although the peak point for each bundle is different. Bundle 5, on the other hand, remained stable until 9-d pONC (**Fig. 2A-B**). The shape, however, did not show a clear trend for the selected bundles, which is likely due to different rates of changes in width and height for individual bundles. Taken together, our results suggest that (1) axon bundles have diverse morphology; (2) four of the five bundles labeled here exhibit an initial swelling phase before a shrinking phase; and (3) the four parameters of individual bundles change following different patterns.

We identified and tracked a total of 141 axon bundles from 3 mice following ONC injury. Histograms were generated (**Fig. 3** and **Suppl Fig. 1**) and their smoothed distributions are shown in **Fig. 3** to illustrate the parameter changes. **Figure 3A** shows that the RGC axon bundle width is significantly increased from baseline (black, mean: 13.7 ± 4.6 µm) to 3-d pONC (dark red; 14.5 ± 4.5 µm; p = 4.6e-2, One-way ANOVA), followed by a decrease at 6-d pONC (red; 12.8 ± 4.3 µm, p = 5.9e-2) and 9-d pONC (light red; 11.5 ± 3.8 µm, p<1e-4). Similarly, the height distribution plot shown in Fig. 3B indicates a significant increase of bundle thickness at 3-d (black; baseline mean: 12.5 ± 3.9 µm; dark blue; 3-d pONC: 13.5 ± 4.5 µm, p=1.5e-2). However, the height returned to baseline at 6-days after ONC (blue; 13.1 ± 4.3 µm, p= 2.5e-1), followed by a significant decrease at 9-d pONC (light blue; 11.1 ± 4.0 µm, p=5.0e-4).

Figure 3C shows the distribution of the bundle area, which indicates axon bundles with larger size at 3-d pONC (dark purple) compared to baseline (black; baseline: 136.6 ± 71.7 µm^2; 3-d pONC: 158.6 ± 82.9 µm^2; p = 9.0e-4). At 6-d pONC (purple), the area returned to baseline (6-d pONC: 133.8 ± 71.3 µm^2; p = 9.1e-1), where at 9-d pONC the area of the axon bundles (light purple) was significantly smaller compared to the baseline area (9-d pONC: 103.8 ± 58.9 µm^2, p<0.0001). We also noticed that large bundles (blue arrows in **Suppl Fig. 1**) tend to disappear first following ONC injury. The distribution curves of the axon bundle shape (**Fig. 3D**) show a progressive shift toward the negative values from baseline (black; 0.065 ± 0.3) compared to 3-d (dark green; 0.067 ± 0.3, p = 9.9e-1), 6-d (green; 0.011 ± 0.3, p = 2.8e-2), and 9-d pONC (light green; - 0.037 ± 0.3, p = 4.8e-2, **Fig. 3G**). These results indicate axon bundles take on a broader shape before injury and begin to shrink to a more circular shape after injury.

We next plotted the percent change values of individual axon bundles (**Figs. 3E-G**). The width of the axon bundles (red) is 14% higher at 3-d pONC compared to baseline and only 0.5% higher at 6-d pONC (**Fig. 3E**). The mean axon bundle height (blue) was 13% higher at 3-d and 9% higher at 6-d pONC compared to baseline. By 9-d pONC, both the width and height of RGC axon bundles decreased by 10% and 7%, respectively (**Fig. 3E**). In other words, the width dropped below baseline close to 6-d pONC, while height dropped below baseline between 6-d and 9-d pONC.

The cross-sectional area, which enhances the subtle changes in the axon bundle morphology, reveals a clear trend (**Fig. 3E**). The area increased by 30% at 3-d, and 8% at 6-d, and then decreased by 16% at 9-d pONC, compared to baseline. We also observed a striking change in bundle shape which decreased from baseline by 190% at 3-d, then to 677% at 6-d, and followed by 404% at 9-d (**Fig. 3F**).

We plotted the size changes in the overall axon bundle population (**Fig. 3G**). About 60% of bundle population presented a size increase at 3-d pONC, and 70% of bundle population showed a size decrease at 9-d pONC. At 6-d pONC, about half of bundle population increased (51%) and half of bundle population decreased (48%). Taken together, our results demonstrate (1) a majority of the axon bundles exhibit a swollen phase immediately following ONC injury followed by a shrinking phase; (2) the change in width is more sensitive than the change in the height immediately after ONC injury; (3) the RGC axon bundle cross-sectional area, which combined the width and height measurements, amplified the subtle changes in axon bundle morphology; and (4) the RGC axon bundle shape parameter showed a strong decrease from baseline suggesting a shift towards bundles becoming elongated axially.

Establishing the correlation of morphological changes in axon bundles with RGC soma loss

We correlated the changes in axon bundle morphology with RGC density. In this set of experiments, we acquired vis-OCT images from healthy wild type mice and mice at 3-, 9-, and 15-d post ONC, respectively. Immediately following vis-OCT imaging, mice were perfused, and the retinas were flattened and immunostained with rbpms, an RGC marker, and imaged by confocal microscopy. As demonstrated in the schematic representation of the flattened retina in **Fig. 4A**, we divided the retina into superior (S), inferior (I), nasal (N), and temporal (T) quadrants. Examples of *in vivo* vis-OCTFs (left panel) and their corresponding *ex vivo* confocal microscopy images of flattened retinas (middle panel) are shown side by side in **Fig. 4B**. Magnified views of retina confocal images (right panel in **Fig 4B-E**) showed a steady decrease in RGC soma density compared to control at 3-d, 9-d, and 15-d pONC.

We quantified the rbpms-positive RGC density from each retina and plotted it against each axon bundle size parameter quantified from vis-OCT images (**Fig. 5A-D**). Each data point represents the average reading per retina. The mean density of rbpms positive RGCs decreased from the control 4095 ± 209 cells/mm^2 (n=6 retinas), to 3475 ± 343 cells/mm^2 (15% reduction, n=9 retinas) at 3-d pONC, 1305 ± 104 cells/mm^2 (68.1% reduction, n=8 retinas) at 9-d pONC, and 611 ± 37 cells/mm^2 (85.1% reduction, n=3 retinas) at 15-d pONC.

The overall relationship between axon bundle height, width, and area with RGC density was non-linear (**Fig. 5A-C**) due to a swelling phase that immediately followed ONC. For example, at 3-d pONC (**Fig. 5A**), an average of 15% of RGCs had degenerated ($p<0.001$), while the area of the axon bundles increased by 36% compared to the control (control: 92.4 ± 13.6 µm^2, n= 6; 3-d pONC: 126 ± 17.8 µm^2, n=9; $p <0.01$). At 9-d pONC, the average area decreased12% at 9-d pONC (81.9 ± 17.8 µm^2, n=8), though not significant compared to controls (p=0.5), while the RGC density decreased 68% compared to the controls ($p<0.001$). At 15-d pONC, the axon bundle area decreased 37% (15-d pONC: 58.4 ± 10.4 µm^2, n=3; p=0.03), while RGC density suffered 85% reduction ($p<0.001$, **Fig. 5C**). Overall, the axon bundle's width, height, and area were initially negatively correlated with RGC density and then became positively correlated.

Second order polynomial regression models were fit to the bundle width, height, and area plots to examine the data quantitatively (dashed lines in **Fig. 5A-C**). RGC density and three of the axon bundle parameters are strongly correlated, and the overall regression was statistically significant for width (R^2=0.55, $p < 0.001$), height (R^2=0.45, $p<0.001$), and area (R^2=0.55, $p<0.001$). From the regressions, we estimated the RGC density at which the thickness, width and area peaked. We found that axon bundle area peaked at 152 µm^2 with an RGC density of 3780 cells/mm^2 (8% cell loss), while the width and height peaked at a lower RGC density of 3000 cells/mm^2 (27% cell loss) and 2875 cells/mm^2 (30% cell loss), respectively.

Though the axon bundle changed in size after ONC injury, we did not observe a clear trend of shape changes (**Fig. 5D**). The shape parameter remained stable slightly below zero in control and ONC retinas, which we fit a linear regression model to (p=0.47, One-way ANOVA; **Fig. 5D**). The R-squared values, significances, and estimates of peak values are listed in Table 1. Taken together, our findings suggest that (1) the width, height, and area parameters of the axon bundles all change with RGC loss following a similar pattern, but with different sensitivity; and (2) area is the first parameter to show a positive correlation with RGC loss.

Due to the unpredictability of location and the extent of RGC damage caused by ONC, we compared the relationship between bundle morphology and RGC density in different retinal quadrants after ONC. In Fig. 6, the four axon bundle parameters for the superior (S), inferior (I), nasal (N) and temporal (T) regions of retina were plotted against RGC density for each of the orientations. Second order polynomial regression models were fit to each region separately (**Fig. 6A-C**). Regression analyses were performed, and we found that all regressions were statistically significant for width, height, and area parameters plotted against rbpms+ RGC density, except for temporal width regression. The R-square values, significances and estimates of peak values for all four regions were listed in **Table 2**. For example, at 3-d pONC, the average density of RGCs in the superior and nasal leaflets had decreased 20% (superior: 3314 ± 356 cells/mm^2 for control, 2681 ± 337 cells/mm^2 at 3-d pONC, $p < 0.01$) and 13% percent (nasal: 4371 ± 334 cells/ mm^2 for control, 3826 ± 385 cells/ mm^2 at 3-d pONC, $p < 0.01$), respectively. These correlate with a significant 48% increase in the area in superior region (control: 94 ± 14.9 µm^2, 3-d pONC: 140 ± 26.5 µm^2, p = 0.01) and a 36% increase in nasal region (control: 91 ± 11.7 µm^2, 3-d pONC: 124 ± 31.6 µm^2, p =0.07). At 15-d pONC, axon bundles from both nasal (15-d pONC: 56 ± 15.7 µm^2, p = 0.2) and superior regions (15-d pONC: 54 ± 14.8 µm^2, p = 0.1) showed reduction in area compared to the control, which correlate with an 84% (nasal: 15-d pONC: 712 ± 52cells/ mm^2, $p < 0.001$, student's t-test) and 87% reduction in RGC density, respectively (superior: 15-d pONC: 414 ± 20 cells/ mm^2, $p < 0.001$, student's t-test). We fit linear regression lines for the shape parameter for each region and performed regression analysis (**Fig. 6D**). Interestingly, though no regression was significant for superior, temporal, and nasal regions, a significant linear relationship was found between RGC density and shape parameter for the inferior region (R^2 = 0.25, $p < 0.01$). We found that there is a negative relationship between axon bundle shape and RGC density, suggesting uneven changes in axon thickness and width in the inferior region. Overall, our data showed that the width, height, and area can serve as quantifiable biomarkers for RGC density globally and regionally.

Confocal microscopy imaging confirmed axon bundle damages after ONC.

We performed confocal airy scan microscopy to further examine the axon bundle damages following ONC injury. The retina was dissected and double-immunostained with mouse anti-tubulin beta 3 (Tuj1, top and bottom rows) and rat anti-neurofilament H (NFH, middle row**, Fig. 7**) (Sánchez-Migallón et al., 2018b). Confocal images were taken at the ONH region of these retinas (top row, **Fig. 7A**) close to the lesion site of ONC surgery. In the control retina, axon bundles were well organized and converged directly toward the ONH to exit the eye. At 3-d pONC (**Fig. 7B**), some axon bundles became disorganized with loose or splitting axon bundles (yellow arrows). We also observed retraction bulbs (white arrows), the non-growing counterparts of growth cones, at the tip of some of the lesioned axons (Ertürk et al., 2007). At 9-d pONC, the axon bundles near the ONH became entangled, with some retraction bulbs and lesioned axon tips pointing away from the ONH (**Fig. 7C**). At 15-d pONC, some of the axon bundles have degenerated and disappeared at the ONH (**Fig. 7D**).

Visible damage was not limited to the ONH area. In the flattened central-peripheral area (**Fig. 8**), axonal spheroids (white arrows) labeled by both Tuj-1 and NFH started to form on axon bundles at 3-d pONC, giving it a beaded morphology different from the control retina (**Fig. 8A-B**). Moreover, degenerating RGC soma became labeled by NFH (**Suppl Fig. 3**). At 9-d pONC, an increased number of axonal spheroids were seen close to (white arrows) and inside of (blue arrows) bundles, with some reaching more than three microns in diameter (**Fig. 8C**), suggesting increased axon degeneration (Yong et al., 2019). At 15-d pONC (**Fig. 8D**), while axonal spheroids were still present on the axon bundles, other types of vesicles were also observed as shown in the magnified view in **Fig. 8D**. These vesicles were positive for NFH, but negative for Tuj-1, suggesting that they consisted entirely of phosphorylated neuro-filaments (Ertürk et al., 2007). Altogether, morphological changes in the axon bundles were observed both at the ONH close to lesion site and in the retina away from the initial lesion site, consistent with our findings of axon bundle morphological changes from vis-OCT imaging.

Simulation using experimental data suggests bundle area is most sensitive to RGC damage

We performed a simulation using our experimental results to determine which bundle size parameter measured by vis-OCT is most sensitive to RGC damage. To do so, we modeled the change in RGC soma density as a function of time after ONC by fitting the experimental soma densities with a logistic function, as shown in **Fig. 9A**. Next, we simulated RGC soma density values normally distributed along the modeled function with the experimentally recorded standard deviation. A total of 10 density values were simulated every 0.25 days, as shown in **Fig. 9B**. Simulated density values were then used as input values for the bundle size parameter models described earlier. Simulated parameter values were normally distributed along the model for each parameter using the experimentally recorded standard deviation values. We then plotted the simulated parameter values as a function of time and used an unpaired t-test with a significance level of 0.05 to determine at which time the parameter was significantly different from the baseline. **Figures 9C-F** show example size parameter versus time plots for bundle cross-sectional area (C), width (D), height (E), and shape (F). We repeated the simulation 50 times and recorded the average p-value as a function of time for each parameter.

The simulation results for determining the most sensitive size parameter are shown in **Fig. 9G**. As indicated by the plot, RGC density reaches the significance threshold at 1.3 days, followed by bundle area at 9.6 days, width at 10.1 days, and height at 10.4 days. Unlike the other bundle size parameters, bundle shape never crosses the significance threshold, indicating that it does not have high enough sensitivity to detect a significant difference within 25 days of the ONC procedure.

The parameter floor is defined as the time point at which no further change in the parameter is detected (Bowd et al., 2017; Mwanza et al., 2015). Using our simulation, we estimated the floor value for each of the measured parameters. To do so, we used an unpaired t-test with a significance level of 0.05 to compare each simulated time point with the final time point. The time at which the p-value of the parameter crossed above the significance threshold was defined as the floor time (t_f) of the parameter. The mean of the parameter value after t_f was defined as the parameter floor.

The simulation result for determining t_f for each parameter is shown in **Fig. 9H**. As indicated by the plot, bundle width is the first to cross the significance threshold at 12.9 days, followed by height at 13.4 days, area at 13.9 days, and RGC density at 15.4 days. The bundle shape parameter did not cross the significance threshold and thus, does not have a parameter floor value within 25 days of the ONC procedure. RGC density had a floor value of 131 cells/mm^2, area had a floor value of 35.0 μm^2, width had a floor value of 6.4 μm, and height had a floor value of 7.1 μm. Together our simulation results suggest that the bundle area is a more sensitive indicator for RGC density than the bundle width and height.

Discussion

RGC axon bundle structure as a new *in vivo* biomarker for RGC damages

Glaucoma can progress without having easily identifiable symptoms until reaching an advanced stage of RGC and vision loss. Early diagnosis and intervention are thus crucial to slow down disease progression in glaucoma (Weinreb et al., 2014). Clinical OCT systems for the diagnosis and monitoring of optic neuropathies operate using NIR illumination. By shifting the illumination wavelengths to the visible light spectrum (510 nm to 610 nm), vis-OCT has an improved axial resolution of 1.3 μm in the retina compared to 4 μm in clinical NIR OCT devices (Shu et al., 2017). In addition to this, vis-OCT has greater contrast between retinal layers due to the higher backscattering properties of biological tissues in the visible light wavelength range (Shu et al., 2017). Taking advantage of this improved resolution and increased contrast sensitivity, we developed vis-OCTF for the analysis of individual RGC axon bundles in vivo. Thus far, we have demonstrated vis-OCTF in the mouse retina to visualize RGC axon bundles in vivo and validated these structures using confocal microscopy ex vivo (Miller et al., 2020). We then applied vis-OCTF to visualize changes in RGC axon bundle structure in the case of increased RGC population using BAX-/- mice and decreased RGC population using ONC mice (Grannonico et al., 2021). In the present study, we set out to develop new analytic tools for extracting RGC axon bundle size parameters from vis-OCTF images to determine which parameter is most sensitive to RGC damages.

Because every RGC extends one axon in the RNFL, we seek to examine whether directly quantifying changes of individual RGC axon bundles can be a more sensitive and accurate indicator than the bulk thickness of RNFL or GCIPL for RGC damage. Specifically, we used an acute ONC injury model to longitudinally track morphological changes in single RGC axon bundles. Taking advantage of vis-OCT's high-resolution imaging capability (Grannonico et al., 2021), we measured four bundle size parameters: (1) lateral width, (2) bundle height, (3) cross-sectional area, and (4) bundle shape. First, we found the bundle width from vis-OCTF is more sensitive to early damage compared to bundle height. The reduction of the lateral width was detected between 3-d and 6-d pONC (**Fig. 3A - 3E**), which was earlier compared to the reduction in the bundle height (6-d to 9-d pONC, **Fig. 3B - 3E**). Secondly, we introduced two novel parameters to measure and track the size and shape of single RGC axon bundles. By combining changes in both dimensions (lateral and axial), the cross-sectional area has shown to be an accurate indicator of RGC damage. At 3-d pONC, we found that 60% of all axon bundles showed a cross-sectional area increase of 30%, corresponding to about 14% increase in width and 15% increase in height (Fig. 3G). Thirdly, the bundle height measurements obtained following ONC matched the fact that RNFL thinning is not sensitive to the early neuropathic damage by ONC (Dong et al., 2017; Hou et al., 2018). We first observed thinning of the RCG axon bundle at 9-days post ONC (**Fig. 3B-E**).

Early retinal swelling has also been reported in another study (Li et al., 2020). However, changes in thickness alone do not reflect detailed changes in the GCL and the IPL. By combining width and height, we observed swelling in individual RGC axon bundles, when only 15% of RGC somas had degenerated at 3-d post ONC. Interestingly, while axons were affected early in disease, the rate of axon shrinkage was not as fast as that of the RGC somas. At 9-d pONC, we observed 68% of RGC soma degeneration while the axon bundles showed about 12% decrease in area. At 15-d pONC, most RGC somas had degenerated (85%), while a substantial amount of axon bundles remained (30% decrease in axon bundle area). This desynchronization of soma and axon suggested a compartmentalized degeneration program of the RGCs, which is in agreement with previous studies (Howell et al., 2013; Whitmore et al., 2005).

Axon beading and RGC degeneration

Dendritic and axonal dysfunction is an early event in animal glaucoma models and may precede RGC soma degeneration (Calkins, 2012; Weinreb et al., 2014). The ONH is hypothesized to be one of the most vulnerable structures to disease insult by glaucoma (Chidlow et al., 2011; Howell et al., 2007; Weinreb et al., 2014). In our study, we observed obvious axon bundle swelling at 3-d pONC (**Figs 3, 5, and 6**), an early time-point when only 15% of RGC somas have degenerated. This suggests morphological changes in axon bundles occur early in disease progression, which agrees with previous studies. In both DBA-2J mice, a genetic model of glaucoma (Howell et al., 2007), and a rat ocular hypertension model (Chidlow et al., 2011), swelling of individual axons was observed. Apart from individual axons, swelling of the RNFL (Rovere et al., 2015) and retina (Li et al., 2020) was also observed in early response to optic nerve injuries. While individual axon damage could lead to the swelling of these larger structures, other mechanisms may also contribute, including inflammatory responses such as macro and microglial proliferation (Ramírez et al., 2010; Rojas et al., 2014; Sobrado-Calvo et al., 2007).

We also show regional differences in bundle changes and RGC soma degeneration (Fig. 6). In wild type retinas, the distribution of general RGCs varies across different regions (Jeon et al., 1998; Kalesnykas et al., 2012; Sonoda, Okabe, et al., 2020). For example, the density of rbpms positive RGCs in the superior region of the retina is 24% lower than the nasal retina in control mice. This difference in the overall RGC density could affect axon bundle organization and change the way they react to disease or injury insults. Furthermore, RGC types distribute unevenly across the retina (Jeon et al., 1998; Kalesnykas et al., 2012; Sonoda, Okabe, et al., 2020), and different types of RGC respond differently to injury and disease (Chen et al., 2015; Feng, Zhao, et al., 2013; Kalesnykas et al., 2012; Puyang et al., 2015). For example, one type of RGCs, the ipRGC, is involved in circadian functions (Do, 2019) and at least one subtype, the M4 ipRGCs, has higher distribution in the superior and temporal retina (Sonoda, Okabe, et al., 2020). It has been found that ipRGC's are more resistant to chronic elevation of IOP (Gao et al., 2022) and ONC injury (Duan et al., 2015) than general RGCs. The retained circadian functions of the mice after chronic IOP elevation also suggests normal function of ipRGCs. Therefore, it is likely that ipRGC axons suffered less damage and morphological changes than other RGCs in the case of ONC injury, potentially contributing to the regional difference in axon bundle morphology changes observed in our study. More studies remain needed to investigate whether the axons of RGC are organized into axon bundles based on function or location.

We also observed the formation of axonal spheroids along the axon bundles, which were seen in a degenerating axon shortly before it became fragmented and completely disintegrated (Beirowski et al., 2005; Wang et al., 2012). As a hallmark sign of axon pathology, the spheroids can be found in various neurodegenerative conditions including Alzheimer's and Parkinson's diseases (Coleman, 2005). It has been shown that these spheroids are calcium rich and contained pro-degenerative molecules, which are released to the inter-axonal space when the spheroids ruptured, hastening axon disintegration (Yong et al., 2019). At 9-d pONC, we observed substantially more spheroids in the axon bundles than 3 days, indicating degenerating axons. Some of the spheroids have diameter of more than 3 microns and might also contribute to the swelling of axon bundles. In vis-OCT fibergrams, the spheroids could not be clearly resolved and were thus included as part of the axon bundle width and height measurements.

Taken together, we established vis-OCTF parameters to track axon bundle morphology in vivo following the acute ONC injury. Based on our findings, both experimental and simulated, we concluded RGC axon bundle cross-sectional area is most sensitive to RGC damages. Our current study presented a new possibility to characterize the morphology of RGC degeneration at the early stage of glaucoma.

Materials and Methods

Healthy adult (3-14 months) male and female wild-type C57BL/6 mice were used for this study. All animal protocols were approved by the University of Virginia institutional animal care and use committee and complied with the National Institutes of Health (NIH) guidelines.

Optic nerve crush Surgery

The ONC procedure was performed as described previously (Grannonico et al., 2021; Puyang et al., 2016). Briefly, mice were anesthetized with an intraperitoneal injection of 80 mg/kg ketamine (Kataset, Zoetis; NADA #043-304) and 4 mg/kg xylazine (AnaSed, Akorn; NADA#139-236). A small incision was made in the superior and lateral conjunctiva and the optic nerve was exposed by a gentle dissection. The optic nerve was then gently clamped with a pair of forceps approximately 1 mm behind the globe for 10 seconds. After surgery, moxifloxacin (0.5%, NDC 60505-0582-4, Apotex Corp.) was applied to the crushed eyes to prevent infection. Mice were kept on a heating pad until fully recovered.

Vis-OCT imaging

A small animal vis-OCT system (Halo 100; Opticent Health, Evanston, IL, USA) was used, as previously reported (Grannonico et al., 2021; Miller et al., 2020). In brief, four to six vis-OCT volumes (512 A-lines/B-scan, 512 B-scans/volume) were acquired from the same eye with the ONH aligned in each corner of the field of view (FOV) to cover different areas of the retina (Grannonico et al., 2021; Miller et al., 2020). For each area, we generated vis-OCT fibergrams from each vis-OCT volume (Miller et al., 2020). We used an intensity-based threshold method to detect the surface of the retina and cropped the RNFL by selecting the first ~16 μm in depth, and then calculated the mean intensity projection along the axial (z) direction to generate the fibergram image composed of RGC axon bundles and surrounding vasculature. The fibergrams were then montaged covering approximately 1.2 mm × 1.2 mm in total (Grannonico et al., 2021).

The four vis-OCT volumes surrounding the ONH were digitally resampled to generate 425 µm radius circumpapillary scans. To do so, we manually marked the ONH in the enface image and plotted an 15 µm thick arc around the ONH. The pixels were then sorted as a function of the angle measured between each sampled A-line and the nasal direction with the ONH as the vertex. Adjacent A-lines within a 0.2° sector were averaged together to reduce speckle noise while preserving spatial density.

Individual axon bundle size quantification

We used the blood vessel pattern and the ONH as reference points to identify and track individual axon bundles in each retina. We measured the axial thickness and lateral width of individual RGC axon bundles using MATLAB. Bundle width measurements were recorded as previously reported. Briefly, the center axis of each bundle was manually marked and the mean intensity profile along the center axis was plotted as shown in **Figure 1C**. The intensity profile was normalized between 0 and 1 and the bundle width was recorded as the profile width at $1/e^2$. Bundle thickness was similarly recorded by extracting the axial intensity profile of the bundle and recording the thickness value at $1/e^2$ as shown in **Figure 1D**. Blood vessels were excluded from analysis by identifying the dark shadows in the B-scan images and uniquely distinguishable branching structures compared with surrounding axon bundles in fibergram images. Measurement values were reported for individual bundles rather than the number of mice.

The shape of each bundle was approximated as an ellipse. Thus, the cross sectional area of each bundle was determined as follows:

$$A_b = \frac{\pi}{4} W_b T_b$$

where A_b is the bundle area, W_b is the bundle width, and T_b is the bundle thickness.

We developed a shape parameter to describe the width to thickness ratio of individual bundles using a dimensionless value normalized between -1 and +1. The shape parameter was calculated as follows:

$$S_b = \left(1 - \left(\frac{\min(W_b, T_b)}{\max(W_b, T_b)}\right)\right)\left(\frac{W_b - T_b}{|W_b - T_b|}\right)$$

where S_b is the shape parameter of a single RGC axon bundle. A positive S_b reflects a wider axon bundle elongated laterally, while a negative S_b reflects a thicker bundle elongated axially axis.

Immunohistochemistry and confocal imaging

After acquiring vis-OCT data, mice were euthanized with 600 mg/kg euthasol (Euthasol, Virbac ANADA, # 200-071) and perfused with 4% paraformaldehyde (PFA) (ChemCruz, sc-281692). Eye cups were dissected, post-fixed in PFA for 30 minutes, washed with phosphate buffered saline containing Triton-X detergent (PBST, 0.5% Triton X-100), and then blocked for 1 hour in blocking buffer (1% BSA and 10% normal donkey serum, 0.5% Triton X-100 (Sigma-Aldrich, St. Louis, MO, USA). Primary antibodies, diluted using blocking buffer, included rabbit anti-rbpms (Abcam, ab194213, 1:500), mouse anti-neurofilament H antibody (Bio-Rad, MCA1321GA, 1:250), mouse anti-Tuj1 (gift from Tony Spano, University of Virginia, 1:250) and rat anti-Icam-II (BD Pharmingen, 553325, 1:500). Secondary antibodies, including donkey anti-mouse immunoglobulin G conjugated to Alexa Fluor 594 dye (Invitrogen A-21203, RRID: AB_141633) and donkey anti-rabbit immunoglobulin G conjugated to Alexa Fluor 488 dye (Invitrogen A-21206, RRID: AB_2535792), were also diluted at 1:1000 in blocking buffer and incubated overnight at 4°C. After immunostaining, retinas were flat-mounted and cut into four quadrants: temporal, nasal, inferior and superior. The blood vessel pattern was used as a landmark to align vis-OCTF and confocal images of flat mounted retinas (**Suppl Figure 2**).

Confocal images were taken using a Zeiss LSM800 confocal microscope (Zeiss, Thornwood, NY). Z-stack images covering the depth of the outer nuclear layer (ONL) to the ganglion cell layer (GCL; approximately 50-80 μm) were acquired. Lower magnification (5×)

pictures were captured for the whole retina using the tiling/stitch function in Zen (Zen 3.2; Oberkochen, Germany). For cell counting, individual images were captured at 10×, covering an area of 0.408 mm^2. To show morphological changes in degenerating axons, individual z-stack images covering an area of 0.0037 mm^2 were taken using a 63× water immersion objective.

To characterize the morphological changes in high resolution, images were taken using the airy scan mode of the confocal. The Airyscan detector consists of 32 elements based on GaAsP PMT, which allows detection of the emission signal of a focal spot much smaller than the typical 1 Airy volume at a resolution of 140 nm in x and y and 400 nm along the optical axis, resulting in better rendering of fluorescently labeled samples.

RGC soma quantification

The nasal side of the eye was marked during eye dissection for orientation. To quantify RGC density, mouse retinas were immunostained with anti-rbpms antibody. For each retina, 16 en face z-stack images covering the depth of GCL were captured (roughly 30 μm of total depth). Four images were acquired for each of the four quadrants to ensure broad coverage of the entire retina (**Figure 4A**). Three rectangles covering no less than 0.03mm^2 area were randomly drawn on the images, avoiding overlaps with large blood vessels. All rbpms-positive cells within the rectangles were manually counted in Zen (Zen 3.2; Oberkochen, Germany). Cell density was calculated using total cell counts divided by area for the four quadrants in each retina. All data analyses were cross-examined by two independent observers.

Statistical Analyses

All statistical analyses were performed using MATLAB and Prism. We used a linear mixed-effects model for all height, width, and area comparisons to remove influence from individual subjects. For ONC experiments, one-way analysis of variance (ANOVA) followed by Dunnett test for multiple comparison were used for RGC loss and changes in the four axon bundle parameters A significance level of 0.05 was used and the p-values of the Dunnett tests were reported unless otherwise stated. All results were reported as mean ± standard deviation.

Table 1. Regression analysis of RGC axon bundle morphology and soma loss (see Figure 5)

Parameter	**Equation**	**R^2**	**p**	**Peak of the Curve/ tipping point**		
				RGC density (cells/mm^2)	**axon parameters**	**RGC loss (%)**
Area	$y = -1E\text{-}05x^2 + 0.076x + 9.98$	0.55	< 0.001	3780	152.9 µm^2	7.7
Width	$y = -7E\text{-}07x^2 + 0.0042x + 5.41$	0.55	< 0.001	3000	11.8 µm	26.7
Thickness	$y = -8E\text{-}07x^2 + 0.0046x + 6.33$	0.45	< 0.001	2875	12.9 µm	27.8
Shape	$y = 1E\text{-}05x - 0.11$	0.05	0.27	N/A	N/A	N/A

Table 2. Region-dependent polynomial regression Analysis of RGC axon bundle morphology and soma loss (see Figure 6)

Parameter	**Region**	**Equation**	**R^2**	**p**	**Peak of the Curve/tipping point**		
					RGC density (cells/mm^2)	**axon parameters**	**RGC loss (%)**
Area	**I**	y = -1E-05x2 + 0.061x + 21.56	0.45	< 0.001	3065	115.5 µm^2	29.5
	N	y = -1E-05x^2 + 0.073x - 2.07	0.48	< 0.001	3670	132.6 µm^2	16.04
	S	y = -2E-05x^2 + 0.082x + 21.97	0.38	<0.01	2040	105.2 µm^2	38.4
	T	y = -8E-06x^2 + 0.050x + 32.06	0.25	0.03	3094	108.6 µm^2	28.9
Width	**I**	y = -6E-07x2 + 0.0037x + 5.05	0.53	< 0.001	3083	10.8 µm	29.04
	N	y = -5E-07x^2 + 0.0034x + 5.58	0.38	<0.01	3400	11.4 µm	22.2
	S	y = -1E-06x^2 + 0.0049x + 5.87	0.39	<0.01	2450	11.9 µm	26.1
	T	y = -4E-07x^2 + 0.0025x + 7.44	0.19	0.08	3125	11.3 µm	28.1
Thickness	**I**	y = -6E-07x2 + 0.0035x + 8.13	0.24	0.04	2917	13.2 µm	32.9

	N	$y = -8E{-}07x^2 + 0.0051x + 4.60$	0.48	< 0.001	3188	12.7 µm	27.1
	S	$y = -9E{-}07x^2 + 0.0046x + 7.11$	0.26	0.03	2556	13.0 µm	22.9
	T	$y = -4E{-}07x^2 + 0.0028x + 7.11$	0.24	0.04	3500	12.0 µm	19.5
Area	**I**	y = 4E-05x - 0.25	0.25	<0.01	N/A	N/A	N/A
	N	y = 7E-06x - 0.08	0.007	0.68	N/A	N/A	N/A
	S	y = 9E-06x - 0.09	0.006	0.71	N/A	N/A	N/A
	T	y = -1E-05x + 0.02	0.01	0.57	N/A	N/A	N/A

Tables

Table 1. Regression analysis of RGC axon bundle morphology and soma loss (see Figure 5)

Parameter	Equation	R^2	p	Peak of the Curve/ tipping point		
				RGC density (cells/mm^2)	axon parameters	RGC loss (%)
Area	$y = -1E-05x^2 + 0.076x + 9.98$	0.55	< 0.001	3780	152.9 µm^2	7.7
Width	$y = -7E-07x^2 + 0.0042x + 5.41$	0.55	< 0.001	3000	11.8 µm	26.7
Thickness	$y = -8E-07x^2 + 0.0046x + 6.33$	0.45	< 0.001	2875	12.9 µm	27.8
Shape	$y = 1E-05x - 0.11$	0.05	0.27	N/A	N/A	N/A

Table 2. Region-dependent polynomial regression Analysis of RGC axon bundle morphology and soma loss (see Figure 6)

Parameter	Region	Equation	R^2	p	Peak of the Curve/tipping point		
					RGC density (cells/mm^2)	axon parameters	RGC loss (%)
Area	**I**	y = -1E-05x2 + 0.061x + 21.56	0.45	< 0.001	3065	115.5 μm^2	29.5
	N	y = -1E-05x^2 + 0.073x - 2.07	0.48	< 0.001	3670	132.6 μm^2	16.04
	S	y = -2E-05x^2 + 0.082x + 21.97	0.38	<0.01	2040	105.2 μm^2	38.4
	T	y = -8E-06x^2 + 0.050x + 32.06	0.25	0.03	3094	108.6 μm^2	28.9
Width	**I**	y = -6E-07x2 + 0.0037x + 5.05	0.53	< 0.001	3083	10.8 μm	29.04
	N	y = -5E-07x^2 + 0.0034x + 5.58	0.38	<0.01	3400	11.4 μm	22.2
	S	y = -1E-06x^2 + 0.0049x + 5.87	0.39	<0.01	2450	11.9 μm	26.1
	T	y = -4E-07x^2 + 0.0025x + 7.44	0.19	0.08	3125	11.3 μm	28.1
Thickness	**I**	y = -6E-07x2 + 0.0035x + 8.13	0.24	0.04	2917	13.2 μm	32.9
	N	y = -8E-07x^2 + 0.0051x + 4.60	0.48	< 0.001	3188	12.7 μm	27.1
	S	y = -9E-07x^2 + 0.0046x + 7.11	0.26	0.03	2556	13.0 μm	22.9
	T	y = -4E-07x^2 + 0.0028x + 7.11	0.24	0.04	3500	12.0 μm	19.5
Area	**I**	y = 4E-05x - 0.25	0.25	<0.01	N/A	N/A	N/A
	N	y = 7E-06x - 0.08	0.007	0.68	N/A	N/A	N/A
	S	y = 9E-06x - 0.09	0.006	0.71	N/A	N/A	N/A
	T	y = -1E-05x + 0.02	0.01	0.57	N/A	N/A	N/A

Figures

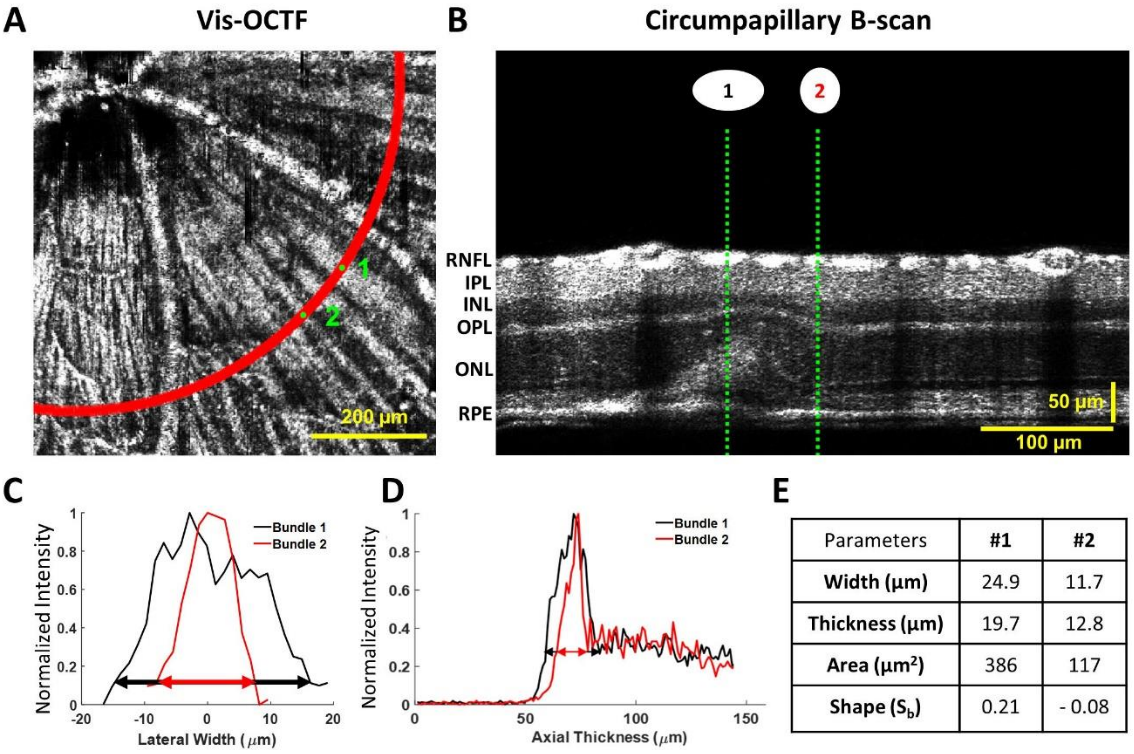

Parameters	#1	#2
Width (µm)	24.9	11.7
Thickness (µm)	19.7	12.8
Area (µm^2)	386	117
Shape (S_b)	0.21	- 0.08

Figure 1. *In vivo* identification and quantification of RGC axon bundle morphology. (A) A fibergram from a single OCT volume of a wild-type mouse. Two RGC axon bundles (1) and (2) were labeled at the radius of 425 µm from the ONH as indicated by the red arc. (B) Circumpapillary B-scan image reconstructed along the red arc in A shows the cross-sectional image of the retina. The blue arrow in A indicates the leftmost A-line in B. The green dashed lines indicate the bundles (1) and (2).. (C-D) Intensity profile of the lateral width (C) and the axial intensity (D) of the bundles (1) and (2). The width of the axon bundle is measured at 1/e2 decay, as indicated by the black (1) and red (2) arrows. (E) Table of the lateral width, axial thickness, cross-sectional area, and the shape indicators of bundles (1) and (2). RNFL: retinal nerve fiber layer; IPL: inner plexiform layer; INL: inner nuclear layer; OPL: outer plexiform layer; ONL: outer nuclear layer; RPE: retinal pigment epithelium

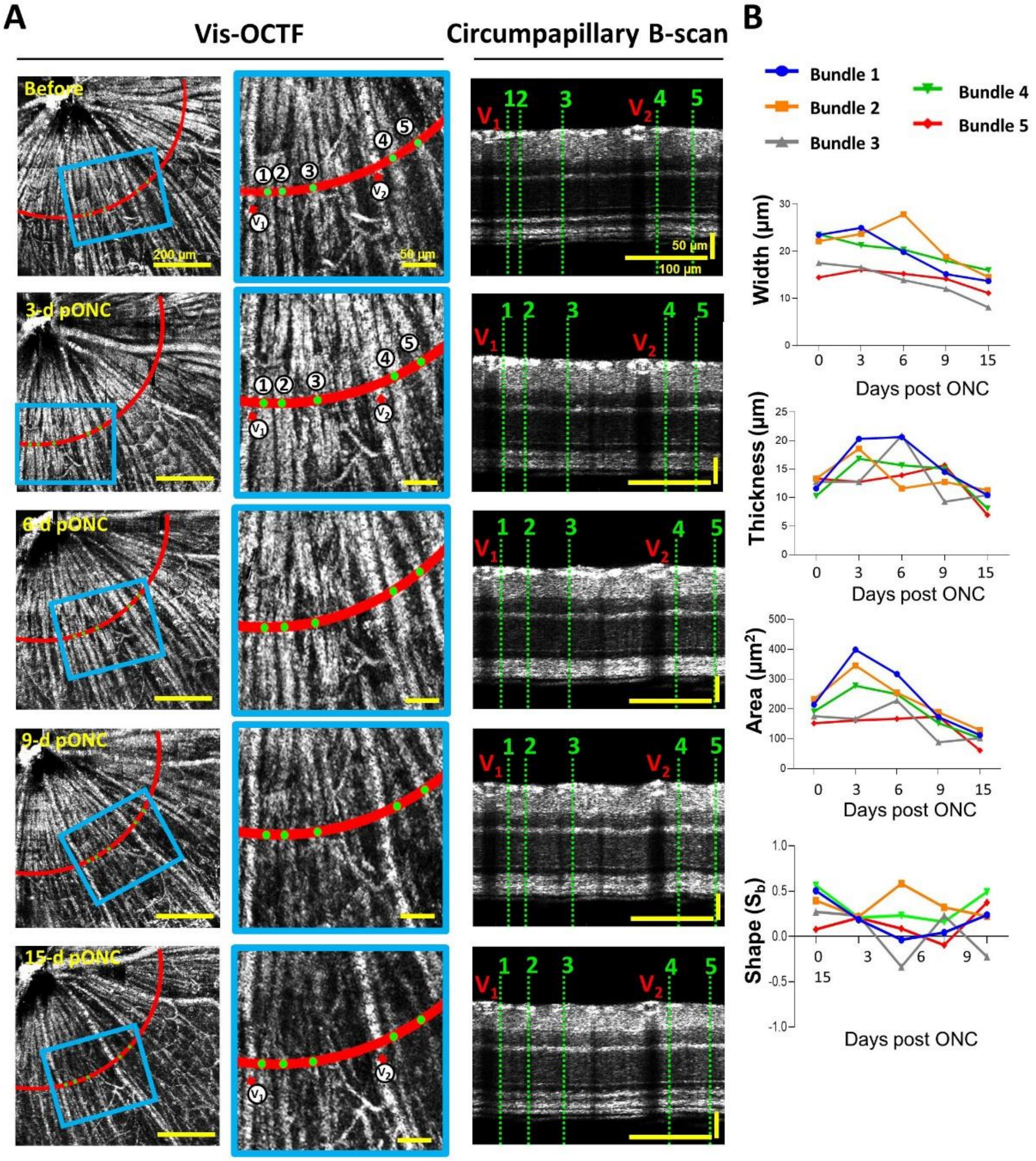

Figure 2. ***In vivo*** **tracking of individual axon bundles following the optic nerve crush (ONC) injury.** (A) In vivo fibergram image of the same retina at baseline and 3-days (d), 6-d, 9-d, and 15-d post ONC (pONC). The left two panels are the vis-OCTF images and right panel is the resampled circumpapillary B-scans at the radius of 425 µm (red arc). Middle panels show the magnified views of highlighted regions in left panels (blue boxes). The green points (1-5) indicate the same five axon bundles tracked over time. The red arrows indicate blood vessels (V1 and

V2). (B) Quantification plots of the lateral width, axial thickness, cross-sectional area, and shape (Sb) of the five tracked axon bundles over time

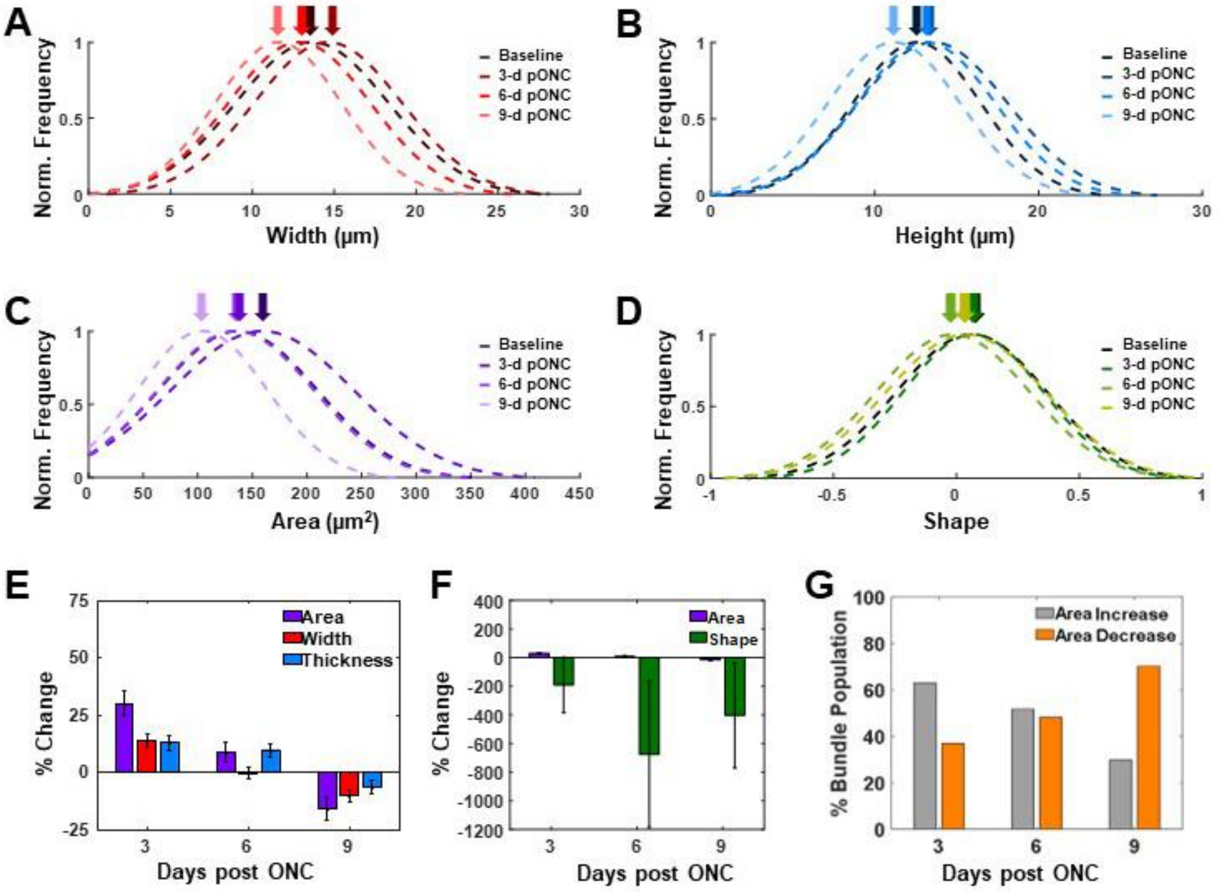

Figure 3. Distribution of the changes in RGC Axon Bundle morphology following the ONC injury. (A-D) Smoothed distributions of the lateral width (A), bundle height (B), cross-sectional area (C), and shape (D) for 141 axon bundles (n = 3 mice) following the ONC injury. Shaded arrows point to the mean value of the distribution curve. (E) Percent change of RGC axon bundle width (red), thickness (blue), and area (purple) with respect to baseline values. (F) Percentage of axon bundles exhibiting increased (gray) or decreased (orange) cross-sectional area at different times compared to baseline.

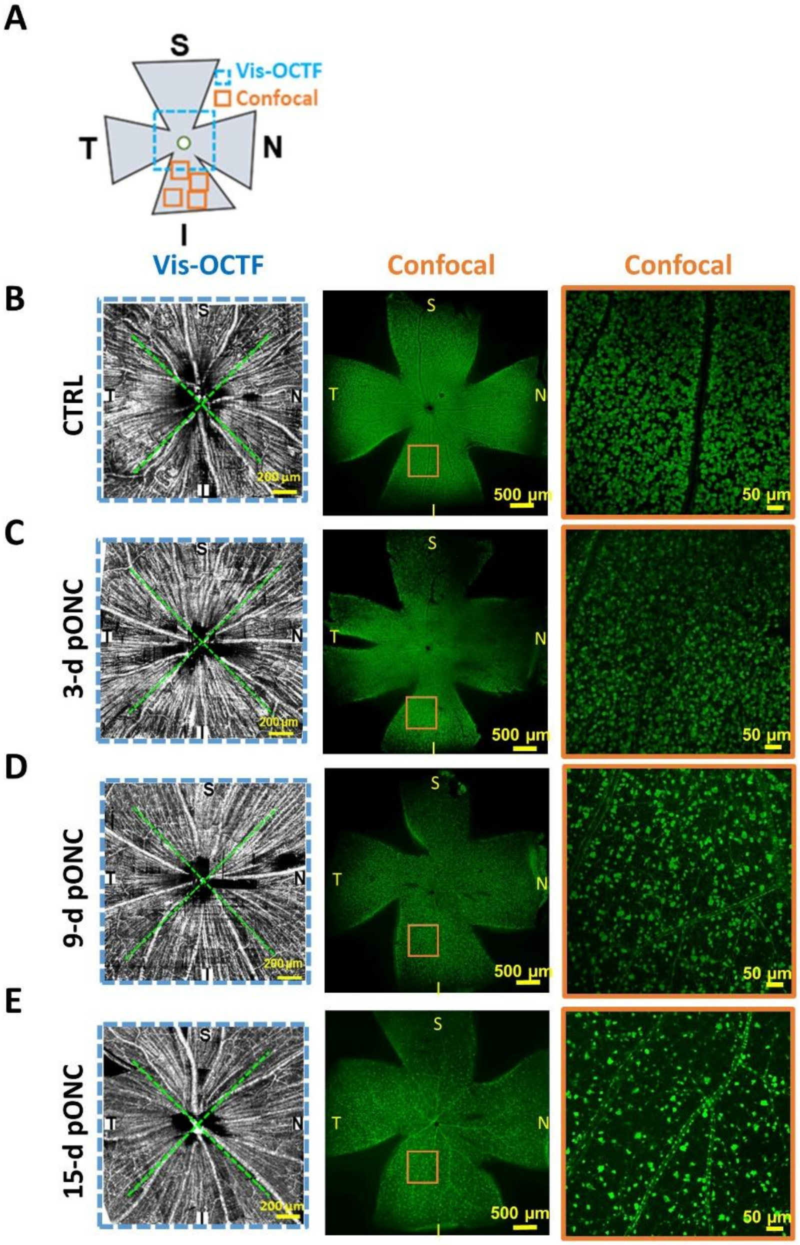

Figure 4. Confocal imaging of flat mounted retinas for quantification of RGC loss following vis-OCT imaging. (A) Schematic representation of the flat mounted retina with vis-OCT (blue box) and confocal microscopy (orange boxes) FOVs overlaid. (B-E) Vis-OCTF (left panel) followed by confocal microscopy images of RGCs labeled by rbpms for estimating RGC density in control (B), 3-d (C), 9-d (D) and 15-d € pONC eyes. Right panels show the magnified views of highlighted regions in middle panels (orange boxes). Green dashed lines in vis-OCTF divided the

field of view into 4 regions: superior (S), nasal (N), temporal (T) and inferior (I).

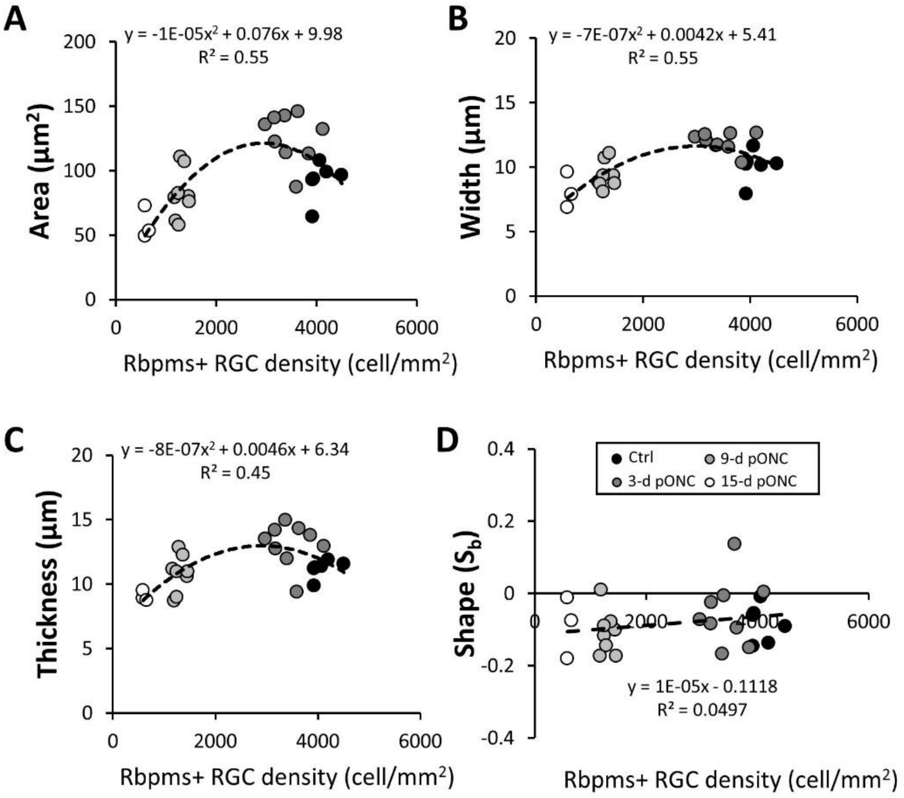

Figure 5. Correlation of RGC soma density and axon bundle size measurements. (A-D) RGC axon bundle cross-sectional area (A), width (B), thickness (C), and shape (D) plotted as a function of rbpms + RGCs density for each retina. Black, dark grey, light grey, and white dots represented data from control (N=6), 3-d (N=9), 9-d (N=8) and 15-d (N=3) pONC, respectively. Second order polynomial regression (dotted line) were fitted to the data for (A-C), and linear regression were fitter to (D). The equation and r-square values are labeled on the figure.

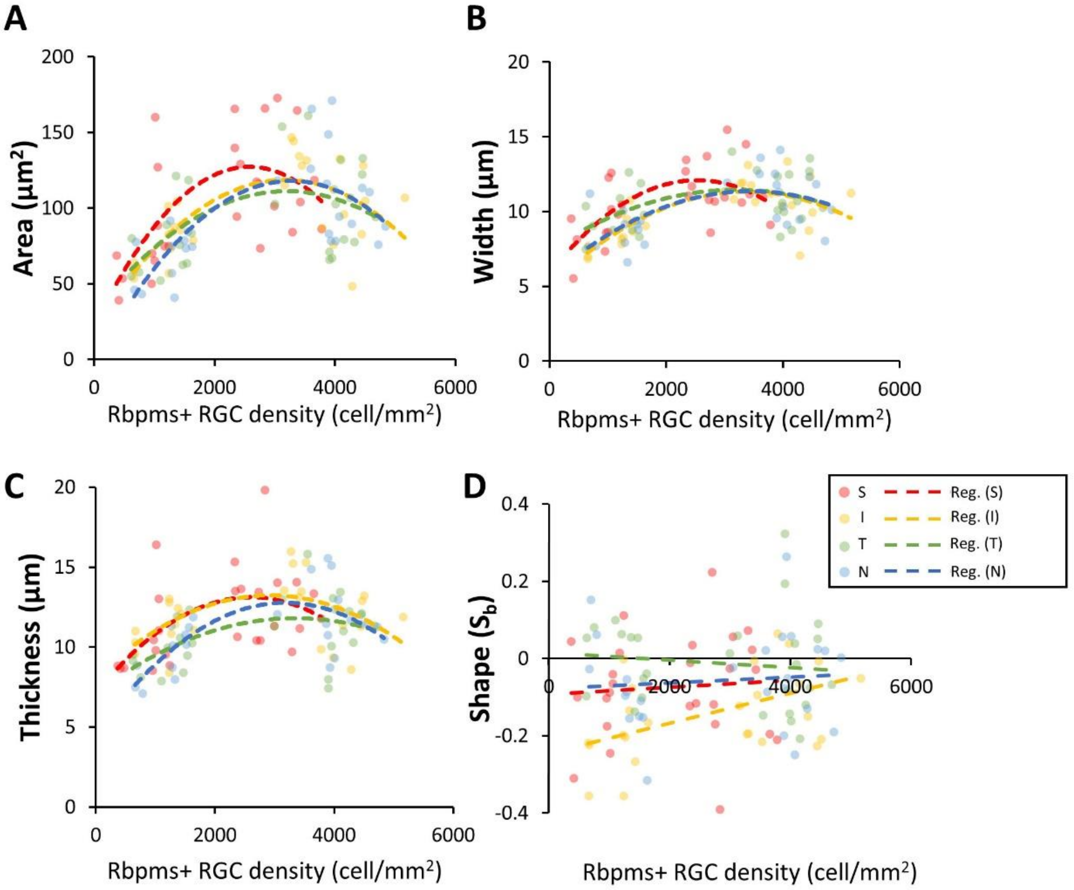

Figure 6. Regional differences were detected between RGC density and axon bundle size measurements. (A-D) RGC axon bundle cross-sectional area (A), width (B), thickness (C), and shape (D) plotted as a function of rbpms + RGCs density from each quadrant of each retina (S: superior; I: inferior; T: temporal; N:nasal). Second order polynomial regressions (dashed lines) were fitted to each region separately for (A-C), and linear regressions were fitted for (D).

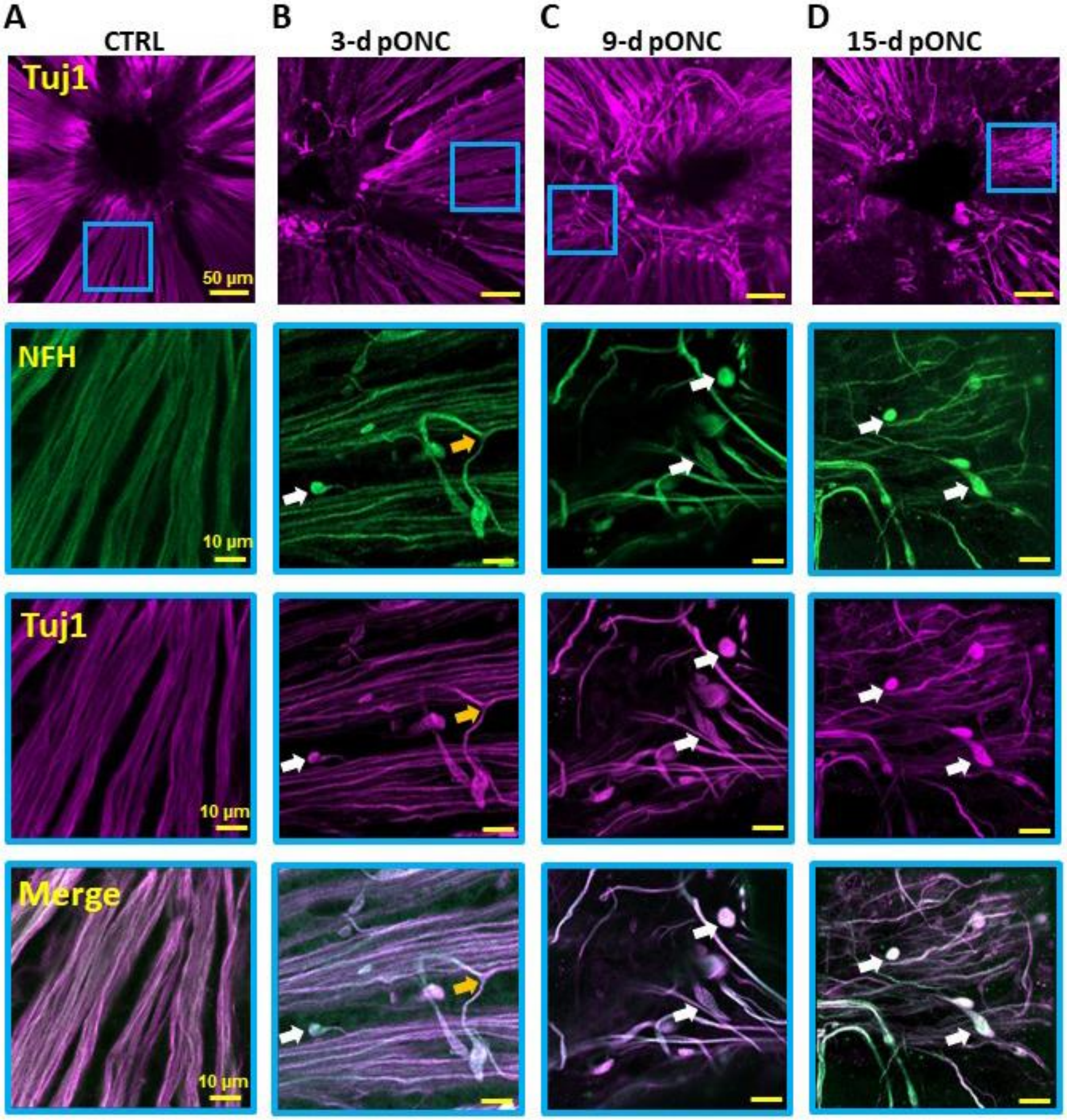

Figure 7. Confocal imaging of the morphological changes of the RGC axon bundles following the ONC injury. Images of flat mounted retinas of control (A), 3-d (B), 9-d (C) and 15-d (D) pONC were double-immunostained with Tuj-1 (purple) and NFH (green) antibodies. Low magnification images taken near the ONH (top panels). High magnification airy scan microscopy images acquired at areas indicated by blue rectangles immunostained by NFH (middle panels) and Tuj1 (bottom panels). The yellow arrow indicates a splitting axon bundle, and the white arrows

indicates retraction bulbs that formed at axon lesion sites.

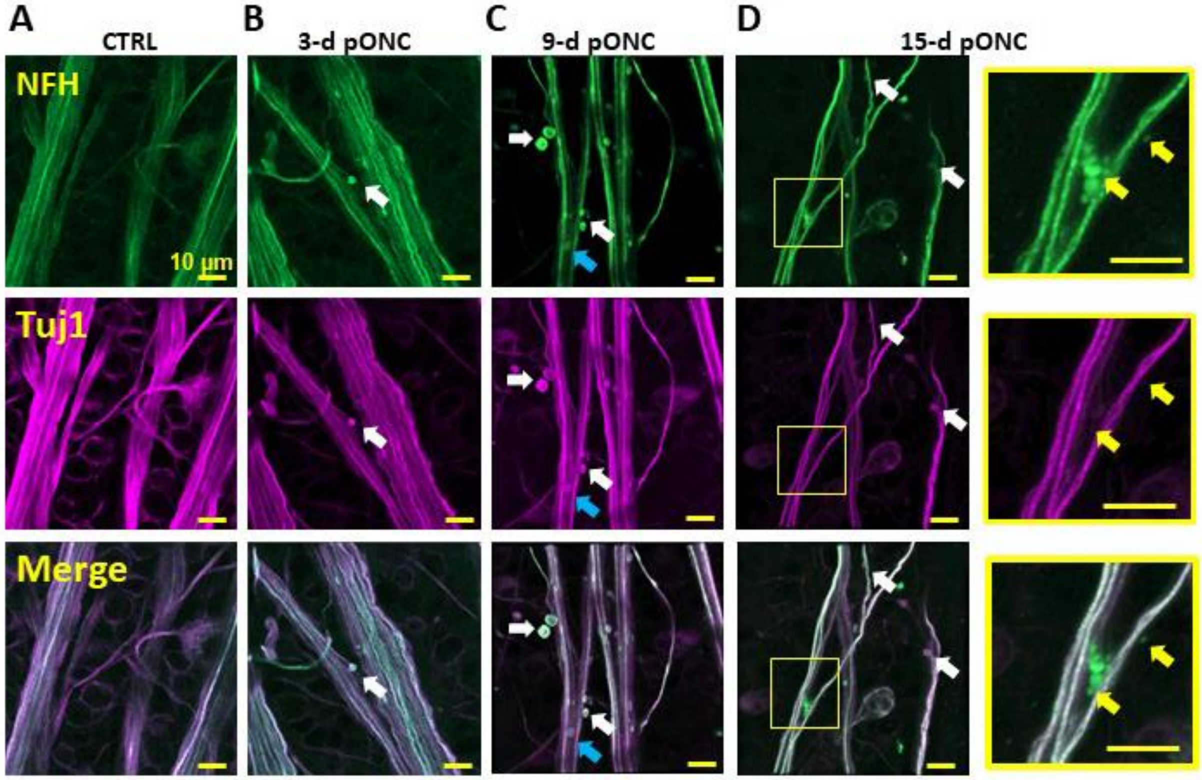

Figure 8. Confocal images of disorganized axon bundles and beaded axons following the ONC injury. Confocal airy scan microscopy images of flat mounted retinas of control (A), 3-d (B), 9-d (C) and 15-d (D) pONC double-immunostained with NFH (top panels, green) and Tuj-1 (bottom panels, purple) antibodies. (A-C) White arrows indicate axonal spheroids formed next to the axon bundles, and blue arrows indicate axonal spheroids formed inside axon bundles. (D) Magnified views of highlighted areas (yellow boxes) show vesicles that were positive for NFH, but not Tuj-1 at 15-d pONC.

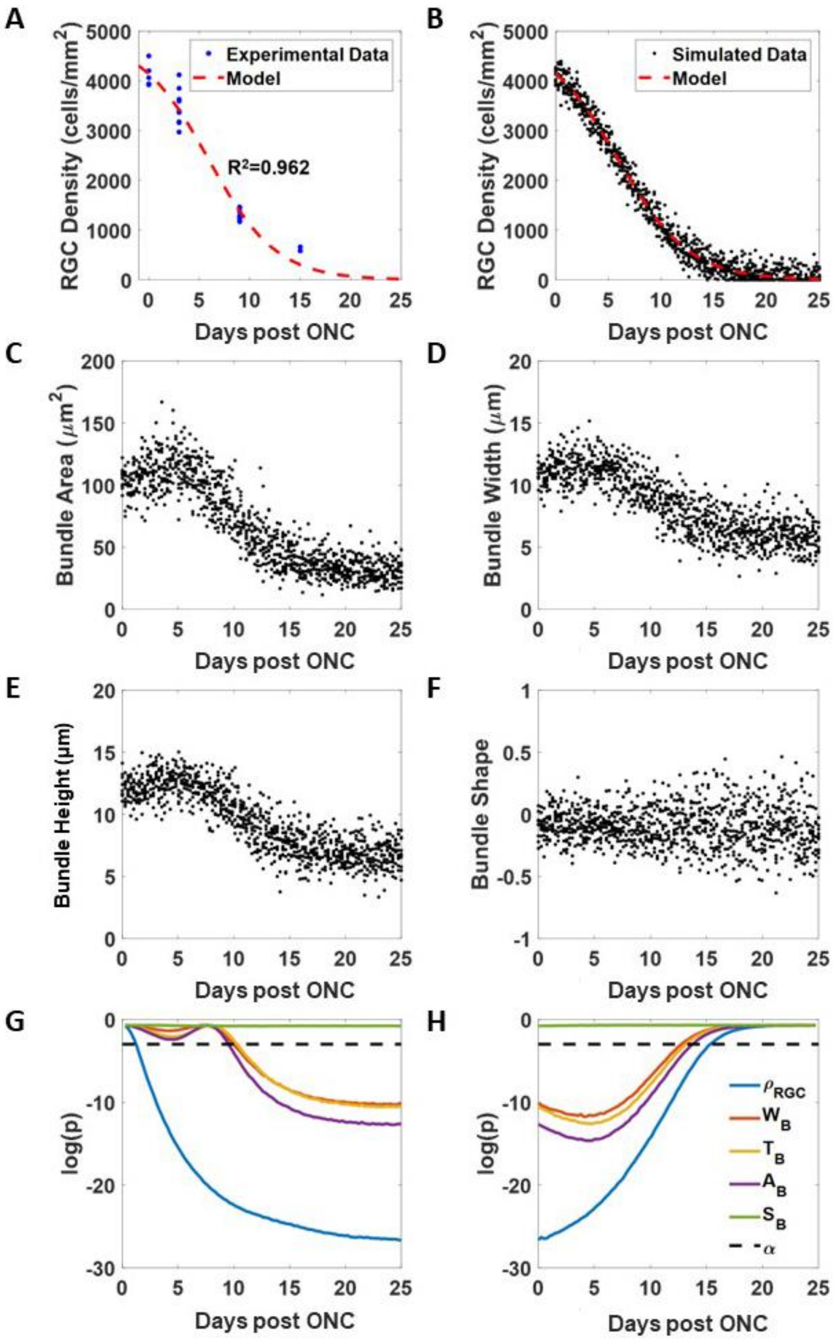

Figure 9. Simulation using experimental data to determine which RGC axon bundle size parameter is most sensitive to RGC damages and estimate parameter floor values. (A) RGC density (ρ_{RGC}, blue data points) plotted as a function of time to establish relationship modeled by a logistic function (dashed red line). (B) Example simulated RGC density values (black data points) as a function of time. (C-F) Example simulated RGC axon bundle size parameters: cross-

sectional area (A_B) (C), width (W_B) (D), thickness (T_B) (E), and shape (S_B) (F). (G) p-values as a function of time for the simulated size parameters to determine which parameters are most sensitive to RGC loss. (H) p-values as a function of time for the simulated size parameters to determine parameter floor times (t_f).

Supplementary Figures

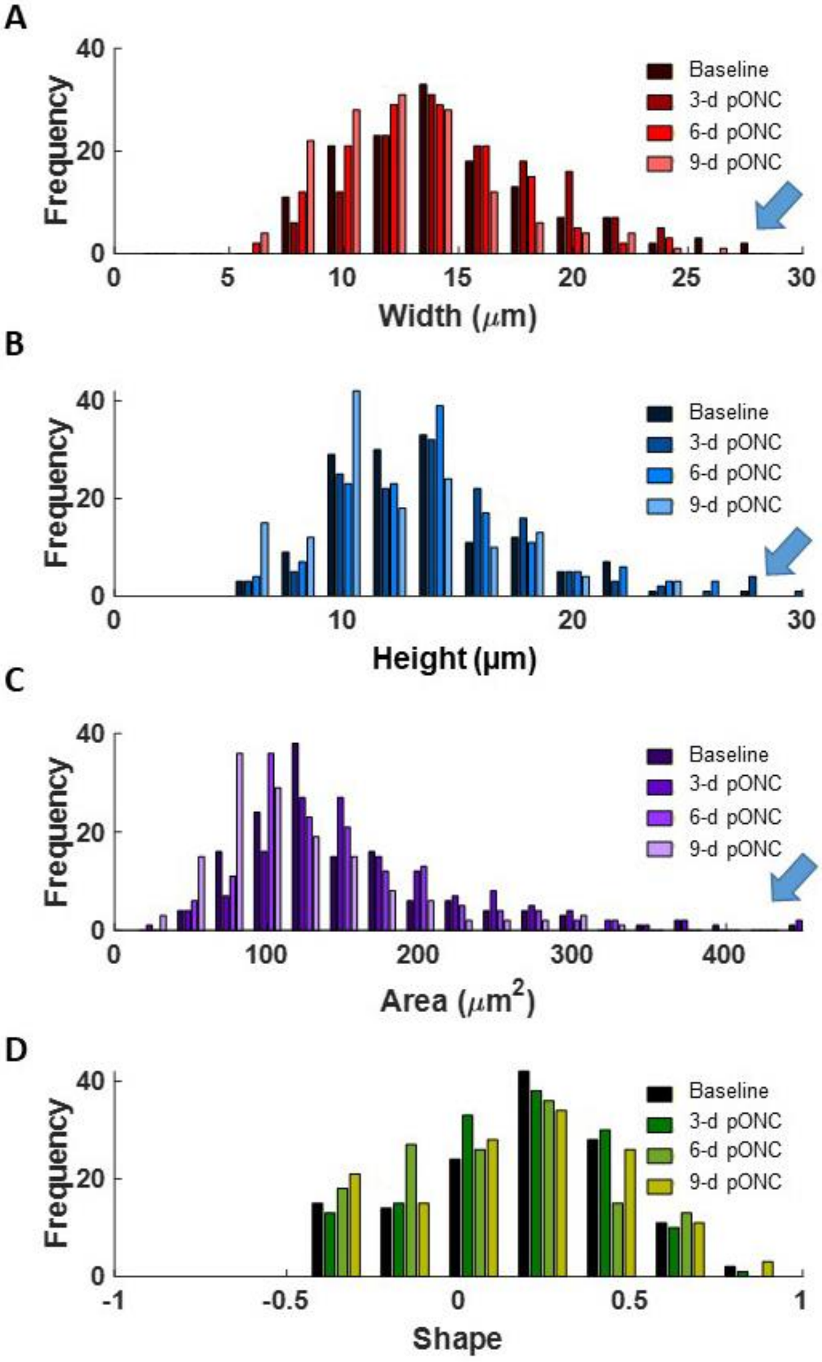

Supplementary Figure 1. Histogram of tracking of a total of 141 RGC axon bundles before ONC and 3-d, 6-d, 9-d pONC (See Figure 3). The width (A), height (B), area (C) and shape (D) were measured, and values were plotted as shown in the histograms. Blue arrows indicate large axon bundles that decrease in size with time after ONC.

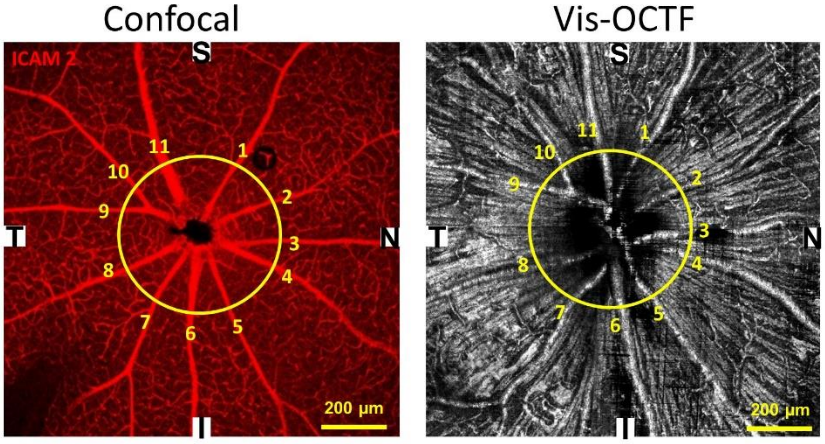

Supplementary Figure 2. The blood vessel pattern was used as a landmark to align vis-OCTF and confocal images of flat mounted retinas (See Figure 4)**.** The same blood vessels were labeled (1-11) in the *ex vivo* confocal image of flat-mounted retina immunostained for ICAM2 and *in-vivo* vis-OCT fibergram of the same retina. S: superior; N: nasal; T: temporal; I: inferior.

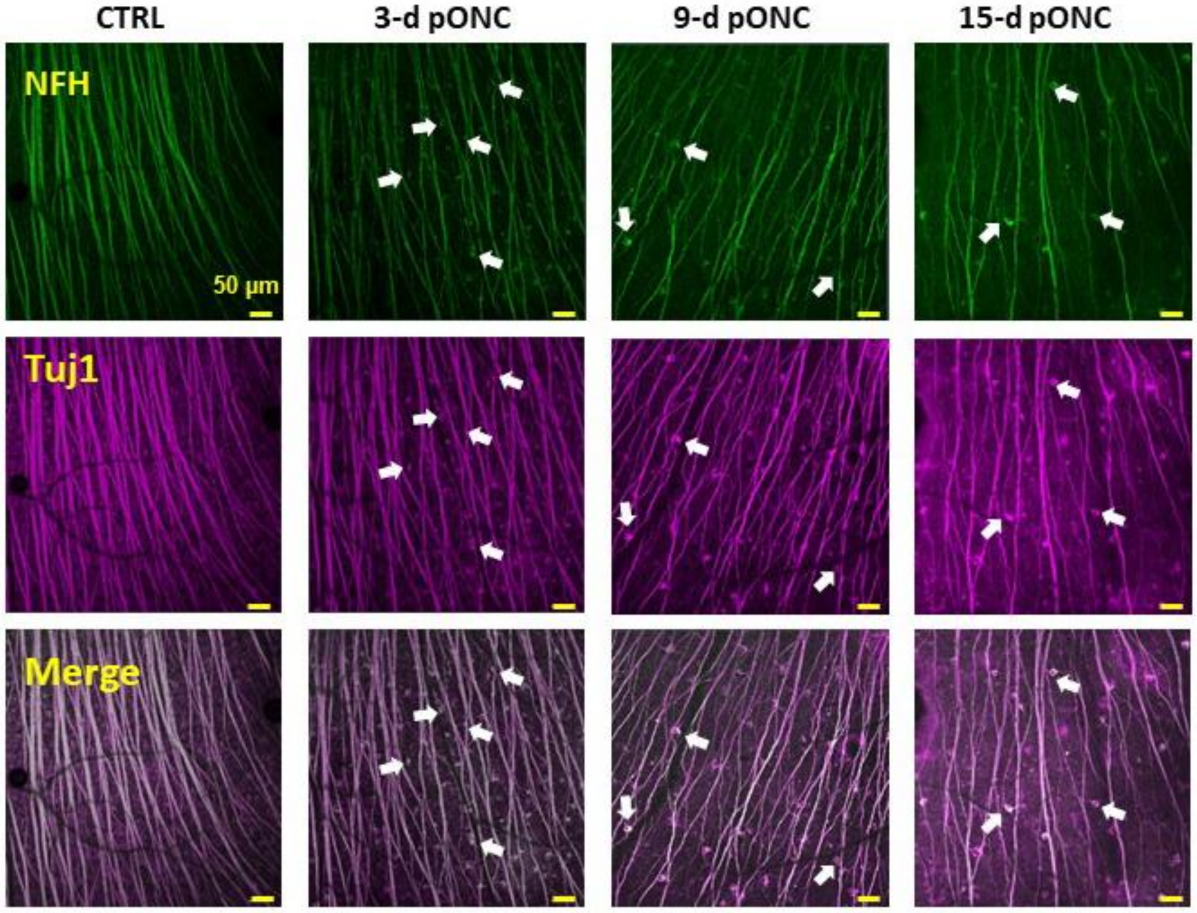

Supplementary Figure 3. Degenerating RGCs were observed post ONC. Flat mounted retinas were double immunostained with Tuj-1 (purple) and NFH (green) antibodies (see Figures 7 and 8). Confocal images were taken at the medial to peripheral retina. Tuj-1 labels axon bundles and some RGC soma membranes, while NFH antibody labels axon bundles and degenerating RGC somas (white arrows).

Chapter 4 Discussion: Rethinking glaucoma pathogenesis

Glaucoma is a group of eye diseases that affects more than 70 million people worldwide and causes 10% of them to be bilaterally blind, making it the leading cause of blindness. It is characterized by the gradual degeneration of retinal ganglion cells (RGC) (Weinreb et al., 2014). The soma of RGC is located in the retina but its axon exits the eye at optic nerve head and projects to the brain along the optic nerve (Sanes & Masland, 2015). The pathogenesis of glaucoma is poorly understood, though elevated intraocular pressure (IOP), the pressure of the eye, is associated with a high proportion of glaucoma cases. Current treatments for glaucoma include drugs and surgeries that alleviate the abnormally elevated IOP, which slows down disease progression for some patients (Weinreb et al., 2014). However, no treatment has been developed that is able to reverse or halt RGC degeneration once degeneration has begun, emphasizing the need to better understand glaucoma pathogenesis for successful disease intervention.

Glaucoma pathogenesis: IOP elevation and its direct effects on RGCs—— the primary damage

To develop more effective treatments for glaucoma patients, it is important to understand how the elevation of intraocular pressure directly affects retinal ganglion cells.

Axons vs. soma: Which is 'attacked' first?

The retinal ganglion cell can be viewed as two segmented compartments: the soma and the axon. RGC somas reside in the eyes, and their axons from bundles that aggregate as optic nerve, exit the eye through the ONH and enroute to various brain targets. In glaucoma, the degeneration of RGC is compartmentalized. While the soma degenerate by caspase dependent apoptosis (Howell et al., 2013; Quigley, 2016), the axons degenerate through Wallerian and/or dying back mechanisms (Howell et al., 2013). For example, when BAX, a proapoptotic molecule, was genetically ablated, RGC soma death was prevented in a mouse glaucoma model, though the RGC axons still suffered degeneration (Libby et al., 2005). In another study, the Wallerian degeneration slow allele (Wld^S) prevented axon damage in glaucomatous mice, but RGC soma were found to shrink in size (Howell et al., 2007). With this compartmentalized degeneration scheme, an interesting question to ask is whether there's a chronological order of events. Specifically, which one, axon or soma, are affected first in glaucoma? It is important to address this question as neuroprotection methods differ depending on the site of action. And determining the location of initial insults will promote successful early intervention for patients. I propose that elevated IOP first affects the RGC axons, and the damage is later transduced to the RGC soma eventually leading to apoptosis.

Currently, arguments supporting both 'axon first' and 'soma first' hypotheses have been presented. One of the main pieces of evidence supporting the 'soma first' hypothesis is that in late stage glaucoma, a considerable number of axons remained even after the majority of the RGCs are gone (Li et al., 2020; Rovere et al., 2015; Sánchez-Migallón et al., 2018a). Our own study (see Chapter 3) also showed that a substantial amount of nerve fibers was present when RGCs had degenerated by 80%. However, this argument has a flaw. The observation that axons remain while most RGCs have degenerated only suggests that axons degenerate at a slower rate and may take longer to disintegrate than the soma. However, it does not indicate that the initiation of axon degeneration happens later. Actually, the very idea of compartmentalized degeneration suggests that the RGC axon and soma may very well degenerate each at their own pace.

On the other hand, a number of studies have been published showing early axon damage in rodent glaucoma models (Buckingham et al., 2008; Chidlow et al., 2011; Howell et al., 2007; Levin, 2001; Vidal-Sanz et al., 2017; Whitmore et al., 2005). For example, in DBA/2J mice, decreased axon counts were seen at 13 months, together with substantial defects in axonal transport revealed by retrograde tracing from the superior colliculus using fluoro-gold. However, significant RGC soma loss was not found until a later time at 18 months(Buckingham et al., 2008). In a rat ocular hypertension model. (Chidlow et al., 2011), accumulation of proteins normally transported along the axon were found at the optic nerve head region, where axonal cytoskeletal abnormalities were seen. The downregulation of RGC specific genes Thy-1 also occurred later than axon damage(Chidlow et al., 2011). Moreover, while protection of the soma does not offer protection for axons(Libby et al., 2005), the protection of axons by the Wld^{S} allele were able to reduce soma degeneration (though the soma still suffer shrinkage) in glaucoma, suggesting that axonal damage is, at least partially, causal to subsequent soma death (Howell et al., 2007).

Though animal models of glaucoma provide great tools to study pathogenesis of glaucoma, findings from these models cannot be directly translated to human glaucoma. In animal models, substantial IOP elevation is induced that leads to rapid RGC degeneration. For many human patients, though, glaucoma is a chronic disease that develops slowly over periods of over one or two decades (Weinreb et al., 2014). This prolonged disease progression poses difficulty for chronological studies. Moreover, at the time visual deficits can be detected by visual field tests, more than 30% amount of retinal ganglion cells may have already degenerated (Harwerth et al., 2010; Kerrigan-Baumrind et al., 2000; Quigley et al., 1981), making it impossible to study early events in human glaucoma.

Though direct evidence is sparse, we can make a calculated guess based on the pattern of progression of visual field loss in glaucoma (Levin, 2001). In human, the horizontal raphe, a horizontal demarcation line in the temporal retina, divides the retina into separate superior and inferior hemispheres. The retinal nerve fibers run in opposite directions at the two sides of horizontal raphe. Due to this organization of the nerve fibers, RGC near the horizontal raphe area may send axons to either side of the hemisphere, resulting in well separated axons despite close proximity of somas. Therefore, the progression of visual field loss differs depending on whether glaucoma damage progress in a ‘axon to axon’ or ‘soma to soma’ way. Specifically, if the damage of glaucoma is perpetuated at the nerve fiber or optic disk level, the spreading of visual field loss should not cross the hemiretina. If glaucoma progresses among adjacent RGC somas, then spreading of visual field loss should not be hindered by the horizontal raphe. Indeed, in patients, glaucomatous visual field deficits spreads in an arcuate pattern in the superior and inferior visual field that usually respects the horizontal median(Åsman & Heijl, 1994; Chauhan et al., 1997), suggesting glaucomatous damage may progress in an ‘axon to axon’ manner (Levin, 2001).

Taken together, RGC axons are highly likely the structure that receive the initial ‘attack’ from elevated IOP.

RGC axons are most vulnerable at the optic nerve head region

Along the RGC axon paths, one region most vulnerable to IOP elevation is the optic nerve head where nerve fibers exit the optic globe. Specifically, the unmyelinated axon bundles aggregate at the optic disk where they turn and travel perpendicular in relation to the retinal plane and invade the lamina cribrosa. In human, the lamina cribrosa consists of a matrix of connective tissues that provide structural support to the nerve bundles(Quigley, 2016). In rodents, this is replaced by a similar structure with astrocytes ensheathing the axon bundles(Chidlow et al., 2011). In healthy eyes, the lamina provides necessary structural and nutritional support to the axons.

In animal models, disrupted axonal transport and axon swelling is seen at the ONH region(Buckingham et al., 2008; Chidlow et al., 2011; Howell et al., 2007; Levin, 2001; Vidal-Sanz et al., 2017; Whitmore et al., 2005). In human glaucoma patients, the lamina cribrosa undergoes substantial remodeling that are easily identified clinically (Anderson & Cynader, 1997; Quigley et al., 1981), but such changes are not observed in some other neurological optic atrophy. The morphological changes here may be a result of the increased circumferentially directed hoop stress result from IOP elevation. Using computer modeling of the posterior scleral shell of human eyes, the mechanical stress IOP exerted on different parts of the posterior eye were examined (Bellezza et al., 2000). The authors found that IOP related stress is the greatest at the load bearing tissue of the lamina but decreases gradually through the peripapillary and posterior scleral regions. Moreover, their model also predicts that elongated eyes and eyes with a larger ONH suffer higher IOP-related stress, which matches with the observation that people with larger ONH are at higher risk of developing open angle glaucoma despite higher RGC densities(Hoffmann et al., 2007).

A more intuitive analogy is to imagine the eye as a balloon filled with maximum amount of air without bursting. Next, we poke a small hole in the balloon representing the ONH in the eye. The balloon will naturally burst. Moreover, if we take a close look at the remains of the balloon, we likely will find a big rupture originating from the ‘ONH’, while other regions of the balloon stay relatively intact. The rupture is a result of the huge amount of pressure exerted by the air inside of the balloon to the small hole, a vulnerable point where the density of the elastic materials is different from the rest of the sphere. In glaucoma, IOP elevation exerts similar, though much less dramatic, effects to the optic nerve head region, where the inside of the eye comes into contact with other tissues.

Normal tension glaucoma (NTG) and IOP elevation

Though IOP elevation is a main risk factor for glaucoma and is seen in majority of glaucoma cases, studies have found that more than 25% glaucoma patients have IOPs lower than 22mm Hg, not substantially higher than then normal IOP seen in healthy subjects (Fechtner & Weinreb, 1994; Weinreb & Tee Khaw, 2004). Moreover, in people with elevated IOP, some never develop glaucoma (Weinreb & Tee Khaw, 2004). One explanation of these observations is that glaucoma is not a heterogeneous disease. In some cases, the initial insults may not come from mechanical damage at the optic nerve head, but from other mechanisms such as inflammation(Gramlich et al., 2015; Luo et al., 2010; Wei et al., 2019), dysregulation of glutamate receptor(Naskar et al., 2000), etc. However, these hypothesis may not offer a conclusive explanation for normal tension glaucoma, as similar morphological changes in optic nerve head can still be observed in these patients compared to those with IOP elevation(Killer & Pircher, 2018).

In fact, when the eye is not viewed as an isolated structure, it is easy to see that intraocular pressure is not the only force directed to the optic nerve head. Post lamina cribrosa, the optic nerve enters the retrobulbar space, a subarachnoid space continuous with the CNS and maintained by the cerebrospinal fluid (CSF). The cerebrospinal fluid pressure acts in the opposite direction against the pressure generated by IOP, creating a translaminar gradient between the two. In many glaucoma cases, IOP elevation results from blockage of the drainage pathways of vitreous humor (Weinreb et al., 2014), a local defect. As a result, the translaminar gradient cannot be held constant and the overall force at the optic nerve head may exceed what it can handle, leading to axon damage.

In normal tension glaucoma, though the IOP is not elevated, the translaminar gradient may change if the cerebrospinal fluid pressure decreases. Indeed, Landi et al (2019) estimated the cerebrospinal fluid pressure (CSFP) using BMI, age and diastolic pressure from POAG patients and healthy subjects. The difference between the IOP and CSFP (TLCPD) were calculated. They found that CSFP was significantly lower and the TLCPD was significantly higher in glaucoma patients compared with healthy subjects. In another study (Siaudvytyte et al., 2016), the intracranial pressure and the neuroretinal rim area (a small rim area generally indicates more severe glaucomatous damage) was measured in patients with normal tension glaucoma. They found that NTG patients have a lower intracranial pressure compared with controls. Moreover, there’s a positive relationship between the intracranial pressure and neuroretinal rim area.

Apart from the lowered CSFP, some patients may develop normal tension glaucoma because of their sensitivity to IOP fluctuations. As explained earlier, Computer modeling of the posterior eye predicted that at a given IOP, eyes with a larger ONH suffer higher stress at the lamina region (Bellezza et al., 2000). Therefore, a small IOP elevation that normally wouldn’t lead to damage may illicit injury for people with larger discs at the ONH. In fact, studies have suggested that NTG patients have larger discs and deeper cups compared with high pressure-induced glaucoma patients(Adlina et al., 2014; Kiriyama et al., 2003).

In summary, axonal damage at the OHN regions may be an early pathological events in normal tension glaucoma despite the lack of substantial IOP elevation. Moreover, the pathogenesis of NTG offers insights to treatments methods. It is known that reducing IOP through drug or surgery does not halt glaucoma disease progression, but merely slows it down. Moreover, some patients do not respond to these treatments. The failure to stop disease progression may be partly due to the inability to balance IOP reduction with CSFP. It is known that both IOP(Maeda et al., 2006) and CSFP(Jasien et al., 2020) are subject to circadian changes. Though the exact regulation mechanism and pattern of change of those pressures is yet to be determined, it is likely that they correlate with each other in order to maintain a constant translaminar gradient (Jasien et al., 2020). However, the administration of IOP reduction drugs does not take this into consideration and may tip the balance at various timepoints, despite an overall IOP reduction. This may account for further damage that cannot be rescued. More studies on this aspect of the disease are needed in order to develop more precise and efficient treatments.

Axonal damage at the OHN: result of direct mechanical insult?

With elevated IOP and/or elevated TLCPD, substantial amount of pressure is forced at the lamina region. It is intuitive to think that the mechanical force directly acts on axons, leading to axon damage. Indeed, when pressure was applied to the motor fibers of the rabbit vagus nerve, axonal transport was significantly inhibited (Hahnenberger, 1980). Moreover, there are many similarities shared among the glaucoma model and the optic nerve crush model that’s generated by applying forces directly at the optic nerve(McKinnon et al., 2009; Yang et al., 2007). This suggests at least partially convergent pathological mechanisms exist between the two.

However, the direct mechanical force acting on the RGC axons might be limited, since axons in run longitudinally to the pressure gradient at the lamina. Let’s consider the balloon analogy again. This time, instead of poking at it with a needle, the OHN will be represented by the mouth of balloon. If we untie the mouth, air will flow out from the mouth in the direction of the neck. If we attach strings at the mouth to represent the axons, the strings will be floating in the direction extending along the neck as air releases which resembles the natural path the axons take. Therefore, the mechanical force is unlikely to greatly distort the axon itself. Instead, the structure that suffer big distortion at the OHN should be the connective tissues matrix(Quigley, 2016) and the astrocytes ensheathing the axon bundles(Dai et al., 2012), as they run orthogonally across the pressure gradient.

Indeed, changes in astrocyte morphology and metabolism have been shown post IOP elevation(Burgoyne, 2011). A descriptive study looked at the changes at ONH in a rat ocular hypertension model(Dai et al., 2012). They found a special type of astrocytes fortified by dense cytoskeletal filaments arranged in a radial array anchored to the thick vascular outer sheath at the OHN in healthy eyes. These astrocytes surround axons passing through the ONH. Shortly after IOP elevation, the dorsal processes of these astrocytes were torn away from the sheath. After the IOP returned to baseline level, the damage continued and eventually led to complete loss of the fortified astrocytes. The axons gradually degenerated following the death of astrocytes, but a small percentage of axons remained when astrocytes were all lost. Moreover, during the whole process, the axons remained at the right angles and their course was not distorted, suggesting they did not suffer great mechanical force.

Under normal conditions, the ONH astrocytes offer important metabolic support for axons. They maintain the extracellular environment, removing potassium and excess glutamate(Burgoyne, 2011). Especially, as the astrocytes have direct contact with the vasculature, it may directly transfer nutrients to the axons at the ONH, which have an extremely high energy demand (Minckler et al., 1976), as the axon hillock generating action potential is located here. As astrocytes degenerate, the metabolic support for the axons is disrupted, leading to subsequent axon degeneration. Indeed, upon IOP elevation, change in mitochondria dynamics and morphology were observed(Abe & Cavalli, 2008; Howell et al., 2013). Moreover, mitochondria accumulated at the OHN in glaucoma(Gaasterland et al., 1978), which may reflect a compensatory effect to restore energy supply.

In conclusion, I propose that apart from the mechanical force, dysfunctional astrocytes and an altered metabolism also contribute, maybe even more, to axon degeneration after IOP elevation.

In vivo monitoring of axon bundles and early diagnosis of glaucoma

Early intervention in glaucoma is important since glaucomatous damage is irreversible. However, glaucoma can progress without having easily identifiable symptoms until reaching an advanced stage. The loss of axons and remodeling of connective tissue produce a characteristic excavated optic nerve head that are often used for diagnosis, but identification of optic disc damage may not be subjective as grading varies between observers (Jampel et al., 2009). Another important test for glaucoma diagnosis is the visual field test. However, more than 30% of RGCs may be lost before visual field defects can be seen (Harwerth et al., 2010; Kerrigan-Baumrind et al., 2000; Quigley et al., 1981). More recent developments in glaucoma diagnosis turn to morphological changes of nerve fibers as increasing evidence point to RGC axons as initial sites of damage in glaucoma. Imaging techniques such as infrared-OCT and confocal scanning laser ophthalmoscopy have made it possible to observe changes in the overall retinal nerve fiber layer (RNFL) thickness (Chauhan et al., 2013; Medeiros et al., 2008). However, they still fail to identify early glaucomatous damages (Alasil et al., 2014; Yi et al., 2016) as RNFL also contain blood vessels and glial cells that may not be affected in glaucoma, which can blanket subtle changes in nerve fibers.

Taking advantage of vis-OCT's high resolution imaging capability(Grannonico et al., 2021), we were able to directly monitor individual axon bundles (see Chapter 3) changes in mice optic nerve crush models. Especially, we detected significant axon bundle swollen at 3-days post ONC across the entire retina, when only 15% of RGCs had degenerated. This swollen of the axon bundles may be caused by swelling of individual axons due to accumulation of organelles and proteins when axonal transport is impeded(Chidlow et al., 2011; Coleman, 2005). Such axon swelling is also observed in the DBA-2J mice(Howell et al., 2007), rat ocular hypertension model(Chidlow et al., 2011), and various other CNS axonopathies(Galvin et al., 1999;

Kerschensteiner et al., 2005). Apart from this, the formation of axonal spheroids may also contribute to the axon bundle swelling, which is observed in our ONC mice model and in various neurodegenerative diseases (Beirowski et al., 2005; Coleman, 2005; Tsai et al., 2004; Wang et al., 2012). Interestingly, as an early mark of axon degeneration(Coleman, 2005; Yong et al., 2019), the formation of spheroids may regress following immunotherapy in a mice model of Alzheimer(Brendza et al., 2005). Therefore, identifying morphological changes and early events in degenerating axons may provide a window for intervention in early glaucoma that can reverse disease progression. Moreover, glaucomatous damage does not manifest all at once across the whole retina and early damages may be only present at local regions. In vivo imaging techniques that can track local or individual axon bundle changes is essential for early diagnosis.

Together, our results confirmed that morphological changes in axon bundles occurred early in ONC model and presented a possibility to characterize early glaucomatous damage.

Are ipRGCs resistant to axonal damage?

All RGCs axons pass through the ONH and are therefore subject to damage when IOP raises. However, not all RGCs degenerate at the same rate in glaucoma. Specifically, we have shown that, ipRGCs, especially the M1 subtypes, seem to preferentially survive in mice OHT model compared with Brn3a positive RGC types (see Chapter 2). It is interesting to ask if this resistance to OHT partly comes from the axons.

Indeed, resistant to glaucomatous damage is different across RGC axons. This differential resistance may depends on the location of the axon bundles, as visual field deficits generally develops in a non-homogenous pattern in glaucoma(Levin, 2001; Weinreb et al., 2014). The morphology and/or type of axons may also contribute. Studies have found degeneration of large diameter axons occurred early in mouse glaucoma model (Grozdanic et al., 2003), primate glaucoma model(Glovinsky et al., 1991) and in human patients(Quigley et al., 1988).

However, study investigating the resistance of ipRGC axons in glaucoma is sparse. In our own study(Gao et al., 2022), the double lasered OHT mice seemed to retain relatively intact circadian function as no delay in circadian re-entrainment was found, while the visual acuity and contrast sensitivity were significantly reduced, likely suggesting preservation of functional axons for the M1s compared to other RGCs (see Chapter 2). One factor that may contribute to M1s' axons resistance to damage is the shorter distance it needs to travel compared with other RGC axons. While majority of the vision formation RGCs innervate the superior colliculus(Sanes & Masland, 2015), the Brn3b negative M1 cells innervate the master circadian clock, SCN, a region a lot less distant from the optic nerve head(Baver et al., 2008; Chen et al., 2011). In various axonopathies where axons degenerate in a dying back mechanisms, longer axons tend to suffer more damage or die quicker than shorter ones, possibly due to higher metabolic demands(Stassart et al., 2018). As dying back mechanism is responsible for some axon degeneration in glaucoma, the shorter routes of the M1 axons may be protective. Apart from this, M1s are also known to send axon collaterals to regions inside of the retina such as the ciliary marginal zone (Semo et al., 2014) and the nerve fiber layer(Joo et al., 2013). These collaterals may provide protection for the M1 cells, as in mice spinal injury, a surviving intact branch of axon suppresses retrograde degeneration of the injured branch (Lorenzana et al., 2015).

In conclusion, ipRGC axons, especially those of M1s, may be more resistance to glaucomatous damage compared to other RGCs due to a shorter route to brain target and surviving axon collaterals. However, we still lack direct observations confirming M1s resistance to axonal damage at the ONH. Future studies can utilize genetic labeling methods to investigate cell type dependent axonal damage in glaucoma, as this may offer insights for effective glaucoma treatments.

Glaucoma pathogenesis: RGC apoptosis and secondary damages

Though the pressure imbalance at the OHN may not directly affects the RGC somas, indirect mechanisms, such as the lack of trophic support and metabolic stress due to halted axonal transport and ischemia, as well as secondary neuroinflammation mediated by glia cells, eventually lead to the loss of RGC somas. A comprehensive understanding of the molecular pathways associated these processes using the 'omic' technologies and will enable development of neuroprotective treatments.

Loss of Neurotrophic factors and RGC apoptosis

Neurotrophic factors are small, diffusible molecules that exert a survival effect on CNS neurons mediated by the tropomyosin related kinase (Trk) receptors and the p75 receptors ($p75^{NTR}$), which are expressed in RGCs. RGCs receive neurotrophic factors (NTFs) from two sources: 1) target-derived factors secreted from higher brain centers where RGC axons innervate and 2) local trophic factors that are produced by retinal neurons and glia cells in the eye. It is known that target derived trophic factors are transported along the RGC axon retrogradely. In development, NTF play important roles in neural pruning, where excess RGCs are eliminated if their axons fail to reach brain targets and receive no target derived neurotrophic factors(Ito & Enomoto, 2016). Post development, target derived NTFs may continue to support the survival of mature RGCs, though there may be a shift to endogenously produced NTFs(Whitmore et al., 2005), as ablating RGC target neurons result in little or much delayed RGC cell death in adult rodents compared to neonates(Harvey & Robertson, 1992; Yang et al., 2013).

It has been proposed that deprivation of target derived NTFs as a result of hindered axonal transport contribute to the apoptosis of RGC soma in glaucoma. In a rodent glaucoma model, accumulation of the radioactively labeled brain derived neurotrophic factor (BDNF), one most intensively studied NTFs, was found at the optic nerve head regions, and its transport to RGC soma was significantly diminished(Quigley et al., 2000). In human patients, decreased level of BDNF was also seen in aqueous humor of the eye(Ghaffariyeh et al., 2011). As NTFs may exert survival effects on RGC, researchers have investigated their neuroprotective effects in various animal glaucoma models. Indeed, upon administration of BDNF, RGC degeneration was significantly reduced in various animal glaucoma model, though this pro-survival effect was often temporary(Claes et al., 2019). Despite BDNF, the neuroprotective effects of other NTFs are controversial. For example, while some studies showed a moderate neuroprotective effect of nerve growth factors (NGF) in animal glaucoma models, others failed to observe it(Almasieh et al., 2011). In fact, NGF could be both pro-survival and pro-apoptotic depending on the type of receptors it binds to(Gupta et al., 2013). Clinical trials of NTFs also yielded contradictory results, while some studies reported application of NTFs reduced RGC loss in glaucoma patients, many failed to demonstrate such an effect or only showed a temporary neuroprotective effects(Lambiase et al., 2009; Osborne, 2009).

The temporary effect can be explained by the desensitization of the NTF receptors. Specifically, excess amount of NTFs may lead to downregulation of receptors(Frank et al., 1996), making subsequent NTF stimulation ineffective. Therefore, instead of supplying NTFs, better neuroprotective treatments may be developed if we shift the focus to downstream actuators in MTF signaling pathways. However, this is a daunting task as NTFs are linked to diverse, intertwining signaling pathways involved in broad cellular responses, including the pro-apoptotic c-Jun N-terminal kinase (JNK) kinase pathway, JAK/STAT pathway, the MAPK/ERK pathway, and many more(Almasieh et al., 2011; Levkovitch-Verbin, 2015; Tezel et al., 2004). Moreover, we still lack a complete description of the spectrum of NTFs present in the retina and most of the current understanding comes from a small number of NTFs investigated in in vitro setups. With this complexity, it is extremely hard to locate key molecules to target to offer effective neuroprotection. In fact, signaling pathways linked to NTFs have been found to up- or downregulated in animal glaucoma models(Levkovitch-Verbin, 2015).

The contradictory results may arise from the many variations along each step of the NTF signaling pathways, which intersect and crosstalk to modulate biological outcomes. Most studies fail to take into account of this complexity as they only look at one or few molecules along a specific pathway by examining phosphorylation states of these molecules via Western blot. Therefore, to truly embark on NTF based therapies, technologies allowing researchers to track multiple pathways simultaneously is required.

Unique trophic support may contribute to ipRGCs resistance to apoptosis

Though little is known whether ipRGCs, especially M1s, suffer less axonal damage in glaucoma, it is well established that their somas preferentially survive in glaucoma and other retinal diseases (see Chapter 1 and 2). As pathways such as JAK/STAT and PIK/Akt play important roles in neuronal survival and can be activated by NTF signaling. Could part of ipRGCs' unique resistance to damage come from difference in trophic support of compared to other RGCs?

Indeed, ipRGCs may have alternative trophic supply compared to other RGCs in injury. It is known that M1s have axon collaterals that terminates within the retina(Joo et al., 2013; Semo et al., 2014) and are thus able to receive target derived trophic support within the retina. Though other RGCs may also receive endogenously produced trophic support, the mode of action of these support may differ. While the target derived trophic factors are endocytosed, retrogradely transported to the soma and activate downstream pathways within the cells through receptor-containing signaling endosomes(Ito & Enomoto, 2016), endogenous NTFs directly bind to receptors at the RGC plasma membrane(Johnson et al., 2009). These difference modes of action are known to induce distinct signaling pathways and produce varying biological outcomes(Segal, 2003). In fact, endogenous NTFs may only offer short term protection to RGCs following damage, while long term protection requires target derived NTFs. Following optic nerve injury, the application of BDNF both to the eye and brain showed long term protection of cat RGCs, while application to the eye only temporarily rescued RGCs(Weber et al., 2010). These observations also match with the dynamic of ipRGC degeneration. Following axotomy, optic nerve crush and acute ocular hypertension, Brn3a positive general RGCs showed two stage of degeneration: an initial stage of rapid cell degeneration followed by a slower and prolonged linear degeneration stage. The ipRGCs, though, only showed an initial reduction in cell density after which no further cell loss was observed(Vidal-Sanz et al., 2017). In a chronic OHT model, ipRGCs also remained stable from 1 to 15 months of injury (Nadal-Nicolás et al., 2015). These observations could be explained by the long term protection effects of continued target derived trophic support.

Apart from sustained target derived trophic support, ipRGCs may also benefit from a better endogenous trophic support in glaucomatous injuries. Unlike other RGCs, the intrinsic photosensitivity of ipRGCs allow them to initiate neuronal activity without receiving inputs from retinal interneurons. Compared with artificial supplementation of NTFs, neuronal activity may induce a more physiologically relevant NTF expression in the neurons and thus avoids the desensitization problem(Corredor & Goldberg, 2009). In glaucoma, dendrites of RGCs tend to shrink in size and complexity(Feng, Zhao, et al., 2013; Puyang et al., 2015; Weinreb et al., 2014), indicating a reduction in inputs and a less robust neuronal activity. IpRGCs, however, may retain robust intrinsic activity with light stimulation. Moreover, study has found that ipRGC dendrites may not suffer from reduction in ocular hypertension (Li et al., 2006). Rather, in aging dystrophic rat retina, ipRGC processes may undergo remodeling and expansion (Vugler et al., 2008). Together, ipRGCs may retain robust neuronal activity and thus sustain a pro-survival NTF profile.

Moreover, ipRGCs' close contact with Muller cells may also provide them with a pro-survival environment. Muller cell is a resident glial cell of retina that provides metabolic, structural, and trophic support to retinal neurons(Pfeiffer et al., 2020). It is known that they secrete several

NTFs such as BDNF, ciliary neurotrophic factors (CNTF) and insulin like growth factor (IGF) that are upregulated upon electrical stimulation of cultured retina(Manthey et al., 2017; Sato et al., 2008). They traverse the retina and their end feed surround RGCs somas, a position that allows them to directly ‘feed’ NTFs to RGCs. Interestingly, injection of tracer virus in one eye labeled ipRGCs in the contralateral eyes shortly after, together with Muller glia and a few amacrine cells, but not other cells. Moreover, immunostaining showed Muller cells were in close proximity with ipRGCs(Viney et al., 2007). These results suggest that Muller cells make specialized contacts with ipRGCs and may provide extra trophic and metabolic support to them.

Taken together, the unique trophic support may contribute to the resistance to apoptosis of ipRGCs. This cell type dependent trophic support and the underlying mechanisms may provide great insights for future NTF based treatments. Though some of the unique structural properties of ipRGCs, such as axon collaterals and Muller cell contacts are hard to apply to other RGCs, modulating the downstream effectors of the unique NTF action modes of ipRGCs may be possible with more comprehensive understanding of the pathways associated.

Glia cells and neuroinflammation cause secondary damage in glaucoma

In glaucoma, IOP elevation, or the imbalance of translaminar pressure, induce axonal damage at the OHN, which eventually leads to the degeneration of the RGC somas. Therefore, restoring the translaminar pressure should be able to save remaining RGCs that are not yet committed to apoptosis and prolonged RGC cell loss should be minimal. However, in animal models of glaucoma, even after the IOP was restored to the baseline level, RGC degeneration progressed, suggesting mechanisms other than axonal damage may lead to secondary damage in glaucoma. Such mechanisms may also explain why treatments reducing IOP is not enough to stop disease progression in glaucoma patients.

One possible candidate is the detrimental effect of neuroinflammation. Neuroinflammation is a defense mechanism that may offer initial protective effects in the CNS, removing pathogens and debris through activation of glial cells such as microglia and astrocytes(Kwon & Koh, 2020). However, sustained neuroinflammation and expanded immune response may cause damage and lead to neural loss. It is implicated in multiple neurodegenerative diseases such as Alzheimer’s disease (AD), Parkinson’s disease (PD), and amyotrophic lateral sclerosis (ALS) (Jiang et al., 2020). Interestingly, glaucoma shares many features with these neurodegenerative diseases. Deposits of amyloid β protein, synuclein, and pTau, a marker of Alzheimer disease, can be seen in glaucomatous retina. The vitreous humor of glaucoma patients also has over a hundred proteins regulation common the pathophysiology of Alzheimer disease(Mélik Parsadaniantz et al., 2020). For example, activation of the complement cascades, a pathway involved in innate immunity, is seen both in Alzheimer and glaucoma(Howell et al., 2011). These similarities suggest neuroinflammation may also play important roles in glaucoma pathogenesis.

Three main types of glial cells reside in the retina: microglia, astrocytes, and Muller cells. After IOP elevation, all three undergo substantial changes, transforming into more reactive types. Astrocytes reside near ONH and may be the first glial cells responding. Increase of astrocytes reactivity shown by higher vimentin level is observed in experimental rat glaucoma model and DBA/2J mice (Son et al., 2010). Microglia cells also become active and transform to more motile amoeba morphology while upregulating secretion of pro-inflammatory cytokines and reactive species and downregulating trophic factor secretion(Bosco et al., 2011; Ebneter et al., 2010; Rashid et al., 2019; Sobrado-Calvo et al., 2007; Son et al., 2010). Similarly, Muller cells upregulate expression of GFAP and Bcl-2, proteins that are found in reactive gliosis in glaucoma (Woldemussie et al., 2004). These activated glial cells with altered functions can no longer provide proper metabolic and trophic support and secrete molecules that are toxic to neurons, leading to RGC damage and degeneration(Rashid et al., 2019).

Moreover, retina as part of the central nervous system, has immune privilege, where the blood-retina barrier and blood-aqueous barrier prevent entrance of pathogens and immune cells into the retina. This feature, together with local production of anti-inflammatory cytokines, prevent heighted immune response in healthy eyes(Jiang et al., 2020). Immune privilege is believed to protect the retina as it has limited self-repair abilities. However, this also suggest, unlike what happens in peripheral inflammation, the retina may lack the mechanism to revert neuroinflammation once it is initiated, causing subsequent RGC loss even after the IOP has returned to baseline level. In glaucoma, IOP elevation cause astrocyte dysregulation, which increased vascular and endothelial permeability. It is shown in mice that a transient elevation of IOP is sufficient to induce infiltration of T-cells and inflammation in retina. The damage of neuroinflammation is reflected by prolonged RGC loss long after IOP dropped(Chen et al., 2018).

Such damage can also be directly examined through transfer experiments. When the aqueous humor or splenocytes cells of glaucomatous mice were transferred to healthy eyes, RGC degeneration is found in the recipient eyes even though IOP elevation was never induced. This process is mediated partly by the cell-cell interaction between transferred T-cells and resident microglia. Such effect was not seen when splenocytes from immune deficient glaucomatous was used in transfer though(Gramlich et al., 2015). Without experimental transfer of immune cells, neuroinflammation can also spread from the glaucomatous eye to the contralateral eye autonomously. In rodents, activated microglia and GFAP upregulation of Muller cells were found in the contralateral retina to the experimental eye in glaucoma(Ramírez et al., 2010; Rojas et al., 2014) and optic nerve crush(Sobrado-Calvo et al., 2007) model. However, without IOP elevation and primary axonal damage, the contralateral eye general show very small RGC damage degeneration, suggesting neuroinflammation alone may not initiate significant glaucomatous damage without axonal damage and vascular remodeling.

Interestingly, different types of RGCs may not be affected equally by neuroinflammation. As discussed in previous section, ipRGCs seem to be resistant to prolonged degeneration compared with other RGCs(Nadal-Nicolás et al., 2015; Vidal-Sanz et al., 2017), suggesting they may not suffer secondary damage caused by neuroinflammation. It is known ipRGCs form specific contacts with Muller glia(Viney et al., 2007), though how this interaction is mediated and how it changes in glaucoma is not known. This type dependent interaction of RGCs with glial cells and other immune cells is worth exploring and a comprehensive understanding may help building better treatment strategies for glaucoma patients. Tools that allow the simultaneous examination of multiple cell types and molecules will be needed.

Single cell omic technologies can accelerate understanding of glaucoma pathogenesis

Attempts have been made to locate molecular targets for neuroprotection in glaucoma. However, contradictory results were often found, and we are yet able to stop or reverse neurodegeneration in glaucoma. Much of that is due to the lack of understanding of the complex molecular pathways involved in RGC degeneration, as successful treatments may require targeting multiple pathways in multiple cell types, a tremendous task to complete with traditional methodologies that only allow researchers to examine a few molecules at a time. With the emergence of single cell omic technologies, though, the field may be at the beginning of establishing a complete understanding of the spectrum of underlying molecules in glaucoma.

Single cell RNA sequencing allows unbiased cell classification and identification of differentially expressed genes. It is well suited tool for compiling comprehensive molecular atlas of retinal cells in glaucoma. In a recent study, single cell RNA-seq was performed on dissociated RGCs of mice retina before and post optic nerve crush (Tran et al., 2019). Using clustering algorithms, they successfully identified 46 RGC subtypes, some of which were not identified previously. They also validated novel molecular markers of these cells, which suggest RGC subtypes can be relatively reliably classified by several novel markers. Especially, many of the novel markers were previously unidentified, a result impossible to achieve with an ‘candidate’ approach. At 14 days post optic nerve crush, some RGCs, such as ipRGCs, were preferentially spared from degeneration, while others suffered more cell loss. Moreover, they were able to identify genes correlated with resistance and vulnerability, which were up or down regulated in in a subtype dependent manner. They expressed the some of the resistant in mice retina and found it increased survival of some susceptible RGCs but not others after optic nerve crush, suggesting neuroprotective strategies need to be designed to particular neuronal populations. This study only focused on RGCs, but not other retinal cells that also contribute to RGC degeneration, such as glial cells. Future studies looking into the change in gene expression profiles of the other retinal cells, especially on the expression of neurotrophic factors and its downstream effects should be performed to search for novel targets for treatment.

Though single cell transcriptomic studies allow unbiased characterization of expression profile changes in glaucoma progression, the findings may not be directly translated to clinical interventions due to ethic and safety issues related to gene therapies. The key is to look at next-step products of the mRNAs, the proteins, as most drugs in use target proteins. Though transcriptomic studies implicitly assume that changes in mRNA expression mediate corresponding changes in the protein products, it is not always the case. In fact, mRNA expression level may only explain less than half of the variations observed in protein levels(Vogel & Marcotte, 2012), as other levels of regulation exist between transcript and protein products. Moreover, in signaling pathways, modifications such as phosphorylation have important biological meanings, which cannot be characterized by transcriptomic studies. Therefore, it is important to investigate protein level changes.

One of the tools that allow the characterization of multiple protein molecules at single cell level is Mass cytometry, a flow cytometry variant that employs time of flight mass spectrometry (TOF-MS) to detect up to 50 heavy metal ions presented in single cells(Bandura et al., 2009). By attaching antibodies to these specific metals, CyToF can detect the relative abundance of 50 distinct antibodies per cell. It is a high throughput method that can measure up to 2 million cells per hour (Spitzer & Nolan, 2016). These properties make CyToF a suitable technology to examine the identity and molecular pathway changes of single cells in a high throughput manner (Bendall et al., 2011; Bodenmiller et al., 2012). Specifically, tissue is dissected and dissociated to single cells and stained with an antibodies conjugated with specific rare earth metals not found in living organisms. Cells are labeled with metal conjugated antibodies using standard immunochemistry method. After introduced into the mass cytometer, stained single cells are nebulized into droplets and passed through 7500K flame. Each cell, together with the conjugated antibody, is ionized. The presence and quantity of ion types present for each cell are then resolved based on the mass and kinetic energy by TOF detector and can be correlated with protein expression profiles. A high parameter dataset for each set will be generated for analysis. Using various statistical methods, the high dimensional data can be visualized to classify cell populations(Van Der Maaten & Hinton, 2008) as well as characterizing progressions of molecular phenotype changes overtime(Zunder et al., 2015). Taken together, these features of the CyToF technology makes it an ideal tool to study changes in NTF related pathways in different RGC subtypes and other retinal cells.

However, CyToF suffer one drawback when in use: Though it allows the examination of over 50 antibodies, it is not truly an unbiased method like single cell RNA-seq. Therefore, it is not an ideal tool to search for completely unknown molecular mechanisms or provide comprehensive description of molecular profiles. With limited ‘spots’ available, the antibody panel need to be carefully designed that allow separation of cell populations and tracking of key molecules in pathways of interests. Therefore, it is important to combine CyToF with other unbiased tools, such as single cell RNA-seq and mass spectrometry. While the other tools can be used to locate interesting pathways and key molecules in disease progression, CyToF may subsequently verify and characterize those changes and allow the identification of high potential clinical targets.

Reference

Abe, N., & Cavalli, V. (2008). Nerve injury signalling. *Current Opinion in Neurobiology*, *18*(3), 276. https://doi.org/10.1016/J.CONB.2008.06.005

Abrahamson, E. E., & Moore, R. Y. (2001). Suprachiasmatic nucleus in the mouse: Retinal innervation, intrinsic organization and efferent projections. *Brain Research*, *916*, 172–191. https://doi.org/10.1016/S0006-8993(01)02890-6

Adlina, A. R., Alisa-Victoria, K., Shatriah, I., Liza-Sharmini, A. T., & Ahmad, M. S. (2014). Optic disc topography in Malay patients with normal-tension glaucoma and primary open-angle glaucoma. *Clinical Ophthalmology (Auckland, N.Z.)*, *8*, 2533. https://doi.org/10.2147/OPTH.S71136

Ahmadi, H., Lund-Andersen, H., Kolko, M., Bach-Holm, D., Alberti, M., & Ba-Ali, S. (2020). Melanopsin-mediated pupillary light reflex and sleep quality in patients with normal tension glaucoma. *Acta Ophthalmologica*, *98*(1), 65–73. https://doi.org/10.1111/AOS.14133

Alasil, T., Wang, K., Yu, F., Field, M. G., Lee, H., Baniasadi, N., De Boer, J. F., Coleman, A. L., & Chen, T. C. (2014). Correlation of Retinal Nerve Fiber Layer Thickness and Visual Fields in Glaucoma: A broken stick model. *Am J Ophthalmol*, *157*(5), 953–959. https://doi.org/10.1016/j.ajo.2014.01.014

Allen, A. E., Martial, F. P., & Lucas, R. J. (2019). Form vision from melanopsin in humans. *Nature Communications*, *10*, 2274. https://doi.org/10.1038/s41467-019-10113-3

Almasieh, M., Wilson, A. M., Morquette, B., Cueva Vargas, J. L., & Di Polo, A. (2011). The molecular basis of retinal ganglion cell death in glaucoma. *Progress in Retinal and Eye Research*, *31*(2), 152–181. https://doi.org/10.1016/j.preteyeres.2011.11.002

An, K., Zhao, H., Miao, Y., Xu, Q., Li, Y.-F., Ma, Y.-Q., Shi, Y.-M., Shen, J.-W., Meng, J.-J., Yao, Y.-G., Zhang, Z., Chen, J.-T., Bao, J., Zhang, M., & Xue, T. (2020). A circadian rhythm-gated subcortical pathway for nighttime-light-induced depressive-like behaviors in mice. *Nature Neuroscience*, *23*, 869–880. https://doi.org/10.1038/s41593-020-0640-8

An, S., Harang, R., Meeker, K., Granados-Fuentes, D., Tsai, C. A., Mazuski, C., Kim, J., Doyle, F. J., Petzold, L. R., & Herzog, E. D. (2013). A neuropeptide speeds circadian entrainment by reducing intercellular synchrony. *Proceedings of the National Academy of Sciences of the United States of America*, *110*(46), e4355-4361. https://doi.org/10.1073/PNAS.1307088110/-/DCSUPPLEMENTAL

Anderson, D. R., & Cynader, M. S. (1997). Glaucomatous optic nerve cupping as an optic neuropathy. *Clinical Neuroscience*, *4*(5), 274–278.

Antle, M. C., & Silver, R. (2005). Orchestrating time: Arrangements of the brain circadian clock. *Trends in Neurosciences*, *28*(3), 145–151. https://doi.org/10.1016/j.tins.2005.01.003

Anton, A., Zangwill, L., Emdadi, A., & Weinreb, R. N. (1997). Nerve Fiber Layer Measurements With Scanning Laser Polarimetry in Ocular Hypertension. *Archives of Ophthalmology*, *115*(3), 331–334. https://doi.org/10.1001/ARCHOPHT.1997.01100150333004

Åsman, P., & Heijl, A. (1994). Diffuse visual field loss and glaucoma. *Acta Ophthalmologica*, *72*(3), 303–308. https://doi.org/10.1111/J.1755-3768.1994.TB02763.X

Ayaki, M., Shiba, D., Negishi, K., & Tsubota, K. (2016). Depressed visual field and mood are associated with sleep disorder in glaucoma patients. *Scientific Reports*, *6*(1), 25699. https://doi.org/10.1038/srep25699

Baden, T., Berens, P., Franke, K., Román Rosón, M., Bethge, M., & Euler, T. (2016a). The functional diversity of retinal ganglion cells in the mouse. *Nature*, *529*, 345–350. https://doi.org/10.1038/nature16468

Baden, T., Berens, P., Franke, K., Román Rosón, M., Bethge, M., & Euler, T. (2016b). The functional diversity of retinal ganglion cells in the mouse. *Nature*, *529*(7586), 345–350. https://doi.org/10.1038/nature16468

Baird, A. L., Coogan, A. N., Siddiqui, A., Donev, R. M., & Thome, J. (2011). Adult attention-deficit hyperactivity disorder is associated with alterations in circadian rhythms at the behavioural, endocrine and molecular levels. *Molecular Psychiatry*, *17*(10), 988–995. https://doi.org/10.1038/mp.2011.149

Bandura, D. R., Baranov, V. I., Ornatsky, O. I., Antonov, A., Kinach, R., Lou, X., Pavlov, S., Vorobiev, S., Dick, J. E., & Tanner, S. D. (2009). Mass Cytometry: Technique for Real Time Single Cell Multitarget Immunoassay Based on Inductively Coupled Plasma Time-of-Flight Mass Spectrometry. *Analytical Chemistry*, *81*(16), 6813–6822. https://doi.org/10.1021/AC901049W

Baver, S. B., Pickard, G. E., Sollars, P. J., & Pickard, G. E. (2008). Two types of melanopsin retinal ganglion cell differentially innervate the hypothalamic suprachiasmatic nucleus and the olivary pretectal nucleus. *European Journal of Neuroscience*, *27*(7), 1763–1770. https://doi.org/10.1111/j.1460-9568.2008.06149.x

Beirowski, B., Adalbert, R., Wagner, D., Grumme, D. S., Addicks, K., Ribchester, R. R., & Coleman, M. P. (2005). The progressive nature of Wallerian degeneration in wild-type and slow Wallerian degeneration (WldS) nerves. *BMC Neuroscience*, *6*, 6. https://doi.org/10.1186/1471-2202-6-6

Bellezza, A. J., Hart, R. T., & Burgoyne, C. F. (2000). The optic nerve head as a biomechanical structure: Initial finite element modeling. *Investigative Ophthalmology and Visual Science*, *41*(10), 2991–3000.

Bendall, S. C., Simonds, E. F., Qiu, P., Amir, E. A. D., Krutzik, P. O., Finck, R., Bruggner, R. V., Melamed, R., Trejo, A., Ornatsky, O. I., Balderas, R. S., Plevritis, S. K., Sachs, K., Pe'er, D., Tanner, S. D., & Nolan, G. P. (2011). Single-Cell Mass Cytometry of Differential Immune and Drug Responses Across a Human Hematopoietic Continuum. *Science*, *332*, 687–696. https://doi.org/10.1126/SCIENCE.1198704

Berson, D. M., Castrucci, A. M., & Provencio, I. (2010). Morphology and mosaics of melanopsin-expressing retinal ganglion cell types in mice. *Journal of Comparative Neurology*, *518*(13), 2405–2422. https://doi.org/10.1016/j.biotechadv.2011.08.021.Secreted

Berson, D. M., Dunn, F. A., & Takao, M. (2002). Phototransduction by retinal ganglion cells that set the circadian clock. *Science*, *295*(5557), 1070–1073. https://doi.org/10.1126/science.1067262

Bleckert, A., Schwartz, G. W., Turner, M. H., Rieke, F., & Wong, R. O. L. (2014). Visual Space Is Represented by Nonmatching Topographies of Distinct Mouse Retinal Ganglion Cell Types. *Current Biology*, *24*(3), 310–315. https://doi.org/10.1016/J.CUB.2013.12.020

Bodenmiller, B., Zunder, E. R., Finck, R., Chen, T. J., Savig, E. S., Bruggner, R. V., Simonds, E. F., Bendall, S. C., Sachs, K., Krutzik, P. O., & Nolan, G. P. (2012). Multiplexed mass cytometry profiling of cellular states perturbed by small-molecule regulators. *Nature Biotechnology*, *30*(9), 858–867. https://doi.org/10.1038/NBT.2317

Bosco, A., Steele, M. R., & Vetter, M. L. (2011). Early microglia activation in a mouse model of chronic glaucoma. *The Journal of Comparative Neurology*, *519*(4), 599–620. https://doi.org/10.1002/CNE.22516

Bowd, C., Zangwill, L. M., Weinreb, R. N., Medeiros, F. A., & Belghith, A. (2017). Estimating OCT Structural Measurement Floors to Improve Detection of Progression In Advanced Glaucoma. *American Journal of Ophthalmology*, *175*, 37. https://doi.org/10.1016/J.AJO.2016.11.010

Brendza, R. P., Bacskai, B. J., Cirrito, J. R., Simmons, K. A., Skoch, J. M., Klunk, W. E., Mathis, C. A., Bales, K. R., Paul, S. M., Hyman, B. T., & Holtzman, D. M. (2005). Anti-Aβ antibody treatment promotes the rapid recovery of amyloid-associated neuritic dystrophy in PDAPP transgenic mice. *Journal of Clinical Investigation*, *115*(2), 428–433. https://doi.org/10.1172/JCI23269

Buckingham, B. P., Inman, D. M., Lambert, W., Oglesby, E., Calkins, D. J., Steele, M. R., Vetter, M. L., Marsh-Armstrong, N., & Horner, P. J. (2008). Neurobiology of Disease Progressive Ganglion Cell Degeneration Precedes Neuronal Loss in a Mouse Model of Glaucoma. *The Journal of Neuroscience*, *28*(11), 2735–2744. https://doi.org/10.1523/JNEUROSCI.4443-07.2008

Burgoyne, C. F. (2011). A Biomechanical Paradigm for Axonal Insult Within the Optic Nerve Head. *Experimental Eye Research*, *93*(2), 120–132. https://doi.org/10.1016/J.EXER.2010.09.005

Burgoyne, C. F. (2015). The Non-Human Primate Experimental Glaucoma Model. *Experimental Eye Research*, *141*, 57–73. https://doi.org/10.1016/J.EXER.2015.06.005

Calkins, D. J. (2012). Critical Pathogenic Events Underlying Progression of Neurodegenration in Glaucoma. *Progress in Retinal and Eye Research*, *31*(6), 702–719. https://doi.org/10.1016/j.pain.2013.06.005.Re-Thinking

Cang, J., Savier, E., Barchini, J., & Liu, X. (2018). Visual Function, Organization, and Development of the Mouse Superior Colliculus. *Annual Review of Vision Science*, *4*, 3.1-3.24.

Chauhan, B. C., LeBlanc, R. P., Shaw, A. M., Chan, A. B., & McCormick, T. A. (1997). Repeatable diffuse visual field loss in open-angle glaucoma. *Ophthalmology*, *104*(3), 532–538. https://doi.org/10.1016/S0161-6420(97)30279-6

Chen, H., Cho, K. S., Vu, T. H. K., Shen, C. H., Kaur, M., Chen, G., Mathew, R., McHam, M. L., Fazelat, A., Lashkari, K., Au, N. P. B., Tse, J. K. Y., Li, Y., Yu, H., Yang, L., Stein-Streilein, J., Ma, C. H. E., Woolf, C. J., Whary, M. T., … Chen, D. F. (2018). Commensal microflora-induced T cell responses mediate progressive neurodegeneration in glaucoma. *Nature Communications*, *9*, 3209. https://doi.org/10.1038/s41467-018-05681-9

Chen, H., Liu, X., & Tian, N. (2014). Subtype-dependent postnatal development of direction- and orientation-selective retinal ganglion cells in mice. *Journal of Neurophysiology*, *112*(9), 2092–2101. https://doi.org/10.1152/jn.00320.2014

Chen, H., Zhao, Y., Liu, M., Feng, L., Zhen, P., Yi, J., Liang, P., Zhang, H. F., Cang, J., Troy, J. B., & Liu, X. (2015). Progressive degeneration of retinal and superior collicular functions in mice with sustained ocular hypertension. *Investigative Ophthalmology and Visual Science*, *56*, 1971–1984. https://doi.org/10.1167/iovs.14-15691

Chen, S. K., Badea, T. C., & Hattar, S. (2011). Photoentrainment and pupillary light reflex are mediated by distinct populations of ipRGCs. *Nature*, *476*, 92–96. https://doi.org/10.1038/nature10206

Chidlow, G., Ebneter, A., Wood, J. P. M., & Casson, R. J. (2011). The optic nerve head is the site of axonal transport disruption, axonal cytoskeleton damage and putative axonal regeneration failure in a rat model of glaucoma. *Acta Neuropathologica*, *121*(6), 737–751. https://doi.org/10.1007/S00401-011-0807-1

Ciulla, L., Moorthy, M., Mathew, S., Siesky, B., Vercellin, A. C., Price, D., Januleviciere, I., & Harris, A. (2019). Circadian rhythm and glaucoma: what do we know. *Journal of Glaucoma*, *29*(2), 127–132. https://doi.org/10.1017/CBO9781107415324.004

Claes, M., De Groef, L., & Moons, L. (2019). Target-Derived Neurotrophic Factor Deprivation Puts Retinal Ganglion Cells on Death Row: Cold Hard Evidence and Caveats. *International Journal of Molecular Sciences*, *20*(17), 4314. https://doi.org/10.3390/IJMS20174314

Coleman, M. (2005). Axon degeneration mechanisms: commonality amid diversity. *Nature Reviews. Neuroscience*, *6*(11), 889–898. https://doi.org/10.1038/NRN1788

Coogan, A. N., Baird, A. L., Popa-Wagner, A., & Thome, J. (2016). Circadian rhythms and attention deficit hyperactivity disorder: The what, the when and the why. *Progress in Neuro-Psychopharmacology & Biological Psychiatry*, *67*, 74–81. https://doi.org/10.1016/j.pnpbp.2016.01.006

Corredor, R. G., & Goldberg, J. L. (2009). Electrical activity enhances neuronal survival and regeneration. *Journal of Neural Engineering*, *6*(5), 055001. https://doi.org/10.1088/1741-2560/6/5/055001

Cui, Q., Ren, C., Sollars, P. J., Pickard, G. E., & So, K.-F. (2015). the Injury Resistant Ability of Melanopsin- Expressing Intrinsically Photosensitive Retinal Ganglion Cells. *Neuroscience*, *284*, 845–853. https://doi.org/10.1016/j.neuroscience.2014.11.002. THE

Da Pozzo, S., Marchesan, R., & Ravalico, G. (2009). Scanning laser polarimetry – a review. *Clinical & Experimental Ophthalmology*, *37*(1), 68–80. https://doi.org/10.1111/J.1442-9071.2008.01891.X

Dai, C., Khaw, P. T., Yin, Z. Q., Li, D., Raisman, G., & Li, Y. (2012). Structural basis of glaucoma: the fortified astrocytes of the optic nerve head are the target of raised intraocular pressure. *Glia*, *60*(1), 13–28. https://doi.org/10.1002/GLIA.21242

De Sevilla Müller, L. P., Sargoy, A., Rodriguez, A. R., & Brecha, N. C. (2014). Melanopsin Ganglion Cells Are the Most Resistant Retinal Ganglion Cell Type to Axonal Injury in the Rat Retina. *PLOS ONE*, *9*(3), e93274. https://doi.org/10.1371/JOURNAL.PONE.0093274

De Zavalía, N., Plano, S. A., Fernandez, D. C., Lanzani, M. F., Salido, E., Belforte, N., Sarmiento, M. I. K., Golombek, D. A., & Rosenstein, R. E. (2011). Effect of experimental glaucoma on the non-image forming visual system. *Journal of Neurochemistry*, *117*(5), 904–914. https://doi.org/10.1111/J.1471-4159.2011.07260.X

Della Santina, L., & Ou, Y. (2017). Who's lost first? Susceptibility of retinal ganglion cell types in experimental glaucoma. *Experimental Eye Research*, *158*, 43–50. https://doi.org/10.1016/J.EXER.2016.06.006

Do, M. T. H. (2019). Melanopsin and the Intrinsically Photosensitive Retinal Ganglion Cells: Biophysics to Behavior. *Neuron*, *104*(2), 205–226. https://doi.org/10.1016/j.neuron.2019.07.016

Dong, Z. M., Wollstein, G., Wang, B., & Schuman, J. S. (2017). Adaptive Optics Optical Coherence Tomography in Glaucoma. *Progress in Retinal and Eye Research*, *57*, 76–88. https://doi.org/10.1016/J.PRETEYERES.2016.11.001

Douglas, R. M., Alam, N. M., Silver, B. D., Mcgill, T. J., Tschetter, W. W., & Peusky, G. T. (2005). Independent visual threshold measurements in the two eyes of freely moving rats and mice using a virtual-reality optokinetic system. *Visual Neuroscience*, *22*(5), 677–684. https://doi.org/10.1017/S0952523805225166

Drouyer, E., Dkhissi-Benyahya, O., Chiquet, C., WoldeMussie, E., Ruiz, G., Wheeler, L. A., Denis, P., & Cooper, H. M. (2008). Glaucoma alters the circadian timing system. *PLoS ONE*, *3*(12), e3931. https://doi.org/10.1371/journal.pone.0003931

Duan, X., Qiao, M., Bei, F., Kim, I., He, Z., & Sanes, J. R. (2015). Subtype-specific regeneration of retinal ganglion cells following axotomy:effects of osteopontin and mtor signaling. *Neuron*, *85*(6), 1244–1256. https://doi.org/10.1016/j.neuron.2015.02.017.SUBTYPE-SPECIFIC

Duda, M., Domagalik, A., Orlowska-Feuer, P., Krzysztynska-Kuleta, O., Beldzik, E., Smyk, M. K., Stachurska, A., Oginska, H., Jeczmien-Lazur, J. S., Fafrowicz, M., Marek, T., Lewandowski, M. H., & Sarna, T. (2020). Melanopsin: From a small molecule to brain functions. *Neuroscience and Biobehavioral Reviews*, *113*, 190–203. https://doi.org/10.1016/j.neubiorev.2020.03.012

Ebneter, A., Casson, R. J., Wood, J. P. M., & Chidlow, G. (2010). Microglial activation in the visual pathway in experimental glaucoma: spatiotemporal characterization and correlation with axonal injury. *Investigative Ophthalmology & Visual Science*, *51*(12), 6448–6460. https://doi.org/10.1167/IOVS.10-5284

Ecker, J. L., Dumitrescu, O. N., Wong, K. Y., Alam, N. M., Chen, S.-K., Legates, T., Renna, J. M., Prusky, G. T., Berson, D. M., & Hattar, S. (2010). Melanopsin-expressing retinal ganglion-cell photoreceptors: cellular diversity and role in pattern vision. *Neuron*, *67*, 49–60. https://doi.org/10.1016/j.neuron.2010.05.023

El-Danaf, R. N., & Huberman, A. D. (2015). Characteristic Patterns of Dendritic Remodeling in Early-Stage Glaucoma: Evidence from Genetically Identified Retinal Ganglion Cell Types. *Journal of Neuroscience*, *35*(6), 2329–2343. https://doi.org/10.1523/JNEUROSCI.1419-14.2015

Emanuel, A. J., Kapur, K., & Do, M. T. H. (2017). Biophysical variation within the M1 type of ganglion cell photoreceptor. *Cell Reports*, *21*(4), 1048–1062. https://doi.org/10.1002/cncr.27633.Percutaneous

Ertürk, A., Hellal, F., Enes, J., & Bradke, F. (2007). Disorganized microtubules underlie the formation of retraction bulbs and the failure of axonal regeneration. *The Journal of Neuroscience*, *27*(34), 9169–9180. https://doi.org/10.1523/JNEUROSCI.0612-07.2007

Esquiva, G., Lax, P., Pérez-Santonja, J. J., García-Fernández, J. M., & Cuenca, N. (2017). Loss of Melanopsin-Expressing Ganglion Cell Subtypes and Dendritic Degeneration in the Aging Human Retina. *Frontiers in Aging Neuroscience*, *9*, 79. https://doi.org/10.3389/FNAGI.2017.00079

Estevez, M. E., Fogerson, P. M., Ilardi, M., Borghuis, B. G., Chan, E., Wen, S., Auferkorte, O. N., Demb,

J. B., & Berson, D. M. (2012). Form and function of the M4 cell, an intrinsically photosensitive retinal ganglion cell type contributing to geniculocortical vision. *Journal of Neuroscience*, *32*(39), 13608–13620. https://doi.org/10.1523/JNEUROSCI.1422-12.2012.Form

Fan, B. J., & Wiggs, J. L. (2010). Glaucoma: genes, phenotypes, and new directions for therapy. *The Journal of Clinical Investigation*, *120*(9), 3064–3072. https://doi.org/10.1172/JCI43085

Fechtner, R. D., & Weinreb, R. N. (1994). Mechanisms of optic nerve damage in primary open angle glaucoma. *Survey of Ophthalmology*, *39*(1), 23–42. https://doi.org/10.1016/S0039-6257(05)80042-6

Feigl, B., Mattes, D., Thomas, R., & Zele, A. J. (2011). Intrinsically Photosensitive (Melanopsin) Retinal Ganglion Cell Function in Glaucoma. *Investigative Ophthalmology & Visual Science*, *52*(7), 4362–4367. https://doi.org/10.1167/IOVS.10-7069

Feigl, B., & Zele, A. J. (2014). Melanopsin-expressing intrinsically photosensitive retinal ganglion cells in retinal disease. *Optometry and Vision Science*, *91*(8), 894–903. https://doi.org/10.1097/OPX.0000000000000284

Feng, L., Chen, H., Suyeoka, G., & Liu, X. (2013). A laser-induced mouse model of chronic ocular hypertension to characterize visual defects. *Journal of Visualized Experiments*, *78*, e50440. https://doi.org/10.3791/50440

Feng, L., Zhao, Y., Yoshida, M., Chen, H., Yang, J. F., Kim, T. S., Cang, J., Troy, J. B., & Liu, X. (2013). Sustained ocular hypertension induces dendritic degeneration of mouse retinal ganglion cells that depends on cell type and location. *Investigative Ophthalmology and Visual Science*, *54*, 1106–1117. https://doi.org/10.1167/iovs.12-10791

Frank, L., Ventimiglia, R., Anderson, K., Lindsay, R. M., & Rudge, J. S. (1996). BDN F Down-regulates Neurotrophin Responsiveness, TrkB Protein and TrkB mRNA Levels in Cultured Rat Hippocampal Neurons. *European Journal of Neuroscience*, *8*(6), 1220–1230. https://doi.org/10.1111/J.1460-9568.1996.TB01290.X

Gaasterland, D., Tanishima, T., & Kuwabara, T. (1978). Axoplasmic flow during chronic experimental glaucoma. 1. Light and electron microscopic studies of the monkey optic nervehead during development of glaucomatous cupping. *Investigative Ophthalmology & Visual Science*, *17*(9), 838–846. https://iovs.arvojournals.org/article.aspx?articleid=2158986

Galvin, J. E., Uryu, K., Lee, V. M. Y., & Trojanowski, J. Q. (1999). Axon pathology in Parkinson’s disease and Lewy body dementia hippocampus contains α-, β-, and γ-synuclein. *Proceedings of the National Academy of Sciences of the United States of America*, *96*(23), 13450–13455. https://doi.org/10.1073/PNAS.96.23.13450

Gao, J., Griner, E. M., Liu, M., Moy, J., Provencio, I., & Liu, X. (2022). Differential effects of experimental glaucoma on intrinsically photosensitive retinal ganglion cells in mice. *Journal of Comparative Neurology*, *530*(9), 1494–1506. https://doi.org/10.1002/CNE.25293

Geevarghese, A., Wollstein, G., Ishikawa, H., & Schuman, J. S. (2021). Optical Coherence Tomography and Glaucoma. *Annual Review of Vision Science*, *7*, 693–726. https://doi.org/10.1146/ANNUREV-VISION-100419-111350

Ghaffariyeh, A., Honarpisheh, N., Heidari, M. H., Puyan, S., & Abasov, F. (2011). Brain-derived neurotrophic factor as a biomarker in primary open-angle glaucoma. *Optometry and Vision Science*, *88*(1), 80–85. https://doi.org/10.1097/OPX.0B013E3181FC329F

Glickman, G., Hanifin, J. P., Rollag, M. D., Wang, J., Cooper, H., & Brainard, G. C. (2003). Inferior Retinal Light Exposure Is More Effective than Superior Retinal Exposure in Suppressing Melatonin in Humans. *Journal of Biological Rhythms*, *18*(1), 71–79. https://doi.org/10.1177/0748730402239678

Glovinsky, Y., Quigley, H. A., & Dunkelbergert, G. R. (1991). Retinal Ganglion Cell Loss Is Size Dependent in Experimental Glaucoma. *Investigative Ophthalmology and Visual Science*, *32*(3), 484–490.

Golombek, D. A., & Rosenstein, R. E. (2010). Physiology of circadian entrainment. *Physiological Reviews*, *90*(3), 1063–1102. https://doi.org/10.1152/physrev.00009.2009

Gracitelli, C. P. B., Abe, R. Y., Tatham, A. J., Rosen, P. N., Zangwill, L. M., Boer, E. R., Weinreb, R. N., & Medeiros, F. A. (2015). Association Between Progressive Retinal Nerve Fiber Layer Loss and Longitudinal Change in Quality of Life in Glaucoma. *JAMA Ophthalmology*, *133*(4), 384–390. https://doi.org/10.1001/JAMAOPHTHALMOL.2014.5319

Gracitelli, C. P. B., Duque-Chica, G. L., Moura, A. L., Nagy, B. V., de Melo, G. R., Roizenblatt, M., Borba, P. D., Teixeira, S. H., Ventura, D. F., & Paranhos, A. (2014). A Positive Association Between Intrinsically Photosensitive Retinal Ganglion Cells and Retinal Nerve Fiber Layer Thinning in Glaucoma. *Investigative Ophthalmology & Visual Science*, *55*(12), 7997–8005. https://doi.org/10.1167/IOVS.14-15146

Gracitelli, C. P. B., Duque-Chica, G. L., Roizenblatt, M., Moura, A. L. D. A., Nagy, B. V., Ragot De Melo, G., Borba, P. D., Teixeira, S. H., Tufik, S., Ventura, D. F., & Paranhos, A. (2015). Intrinsically Photosensitive Retinal Ganglion Cell Activity Is Associated with Decreased Sleep Quality in Patients with Glaucoma. *Ophthalmology*, *122*(6), 1139–1148. https://doi.org/10.1016/J.OPHTHA.2015.02.030

Gramlich, O. W., Ding, Q. J., Zhu, W., Cook, A., Anderson, M. G., & Kuehn, M. H. (2015). Adoptive transfer of immune cells from glaucomatous mice provokes retinal ganglion cell loss in recipients. *Acta Neuropathologica Communications*, *3*(1), 56. https://doi.org/10.1186/S40478-015-0234-Y/FIGURES/5

Grannonico, M., Miller, D. A., Liu, M., Norat, P., Deppmann, C. D., Netland, P. A., Zhang, H. F., & Liu, X. (2021). Global and Regional Damages in Retinal Ganglion Cell Axon Bundles Monitored Non-Invasively by Visible-Light Optical Coherence Tomography Fibergraphy. *The Journal of Neuroscience*, *41*(49), 10179–10193. https://doi.org/10.1523/JNEUROSCI.0844-21.2021

Grippo, R. M., Purohit, A. M., Zhang, Q., Zweifel, L. S., & Güler, A. D. (2017). Direct Midbrain Dopamine Input to the Suprachiasmatic Nucleus Accelerates Circadian Entrainment. *Current Biology*, *27*(16), 2465-2475.e3. https://doi.org/10.1016/j.cub.2017.06.084

Grozdanic, S. D., Betts, D. M., Sakaguchi, D. S., Allbaugh, R. A., Kwon, Y. H., & Kardon, R. H. (2003). Laser-induced mouse model of chronic ocular hypertension. *Investigative Ophthalmology and Visual Science*, *44*(10), 4337–4346. https://doi.org/10.1167/iovs.03-0015

Gupta, V. K., You, Y., Li, J. C., Klistorner, A., & Graham, S. L. (2013). Protective effects of 7,8-dihydroxyflavone on retinal ganglion and rgc-5 cells against excitotoxic and oxidative stress. *Journal of Molecular Neuroscience*, *49*(1), 96–104. https://doi.org/10.1007/S12031-012-9899-X/FIGURES/8

Hahnenberger, R. W. (1980). Inhibition of fast anterograde axoplasmic transport by a pressure barrier. The effect of pressure gradient and maximal pressure. *Acta Physiologica Scandinavica*, *109*(2), 117–121. https://doi.org/10.1111/J.1748-1716.1980.TB06575.X

Hanna, L., Walmsley, L., Pienaar, A., Howarth, M., & Brown, T. M. (2017). Geniculohypothalamic GABAergic projections gate suprachiasmatic nucleus responses to retinal input. *The Journal of Physiology*, *595*(11), 3621–3649. https://doi.org/10.1113/JP273850

Hannibal, J., Christiansen, A. T., Heegaard, S., Fahrenkrug, J., & Kiilgaard, J. F. (2017). Melanopsin expressing human retinal ganglion cells: Subtypes, distribution, and intraretinal connectivity. *Journal of Comparative Neurology*, *525*(8), 1934–1961. https://doi.org/10.1002/cne.24181

Hannibal, J., Kankipati, L., Strang, C. E., Peterson, B. B., Dacey, D., & Gamlin, P. D. (2014). Central projections of intrinsically photosensitive retinal ganglion cells in the macaque monkey. *Journal of Comparative Neurology*, *522*(10), Spc1. https://doi.org/10.1002/cne.23588

Harvey, A. R., & Robertson, D. (1992). Time-course and extent of retinal ganglion cell death following ablation of the superior colliculus in neonatal rats. *Journal of Comparative Neurology*, *325*(1), 83–94. https://doi.org/10.1002/CNE.903250108

Harwerth, R. S., Wheat, J. L., Fredette, M. J., & Anderson, D. R. (2010). Linking Structure and Function in Glaucoma. *Progress in Retinal and Eye Research*, *29*(4), 249–271. https://doi.org/10.1016/J.PRETEYERES.2010.02.001

Hattar, S., Kumar, M., Park, A., Tong, P., Tung, J., Yau, K.-W., & Berson, D. M. (2006). Central projections of melanopsin-expressing retinal ganglion cells in the mouse. *The Journal of Comparative Neurology*, *497*(3), 326–349. https://doi.org/10.1002/cne.20970

Hattar, S., Liao, H.-W., Takao, M., Berson, D. M., & Yau, K.-W. (2002). Melanopsin-Containing Retinal Ganglion Cells: Architecture, Projections, and Intrinsic Photosensitivity. *Science*, *295*(5557), 1065–1070. https://doi.org/10.1126/science.1069609.Melanopsin-Containing

Hoffmann, E. M., Zangwill, L. M., Crowston, J. G., & Weinreb, R. N. (2007). Optic Disk Size and Glaucoma. *Survey of Ophthalmology*, *52*(1), 32–49. https://doi.org/10.1016/J.SURVOPHTHAL.2006.10.002

Honda, S., Namekata, K., Kimura, A., Guo, X., Harada, C., Murakami, A., Matsuda, A., & Harada, T. (2019). Survival of Alpha and Intrinsically Photosensitive Retinal Ganglion Cells in NMDA-Induced Neurotoxicity and a Mouse Model of Normal Tension Glaucoma. *Investigative Ophthalmology & Visual Science*, *60*(12), 3696–3707. https://doi.org/10.1167/IOVS.19-27145

Hou, H. W., Lin, C., & Leung, C. K. S. (2018). Integrating Macular Ganglion Cell Inner Plexiform Layer and Parapapillary Retinal Nerve Fiber Layer Measurements to Detect Glaucoma Progression. *Ophthalmology*, *125*(6), 822–831. https://doi.org/10.1016/J.OPHTHA.2017.12.027

Howell, G. R., Libby, R. T., Jakobs, T. C., Smith, R. S., Phalan, F. C., Barter, J. W., Barbay, J. M., Marchant, J. K., Mahesh, N., Porciatti, V., Whitmore, A. V., Masland, R. H., & John, S. W. M. (2007). Axons of retinal ganglion cells are insulted in the optic nerve early in DBA/2J glaucoma. *Journal of Cell Biology*, *179*(7), 1523–1537. https://doi.org/10.1083/jcb.200706181

Howell, G. R., Macalinao, D. G., Sousa, G. L., Walden, M., Soto, I., Kneeland, S. C., Barbay, J. M., King, B. L., Marchant, J. K., Hibbs, M., Stevens, B., Barres, B. A., Clark, A. F., Libby, R. T., & John, S. W. M. (2011). Molecular clustering identifies complement and endothelin induction as early events in a mouse model of glaucoma. *The Journal of Clinical Investigation*, *121*(4), 1429–1444. https://doi.org/10.1172/JCI44646

Howell, G. R., Soto, I., Libby, R. T., & John, S. W. M. (2013). Intrinsic axonal degeneration pathways are critical for glaucomatous damage. *Experimental Neurology*, *246*, 54–61. https://doi.org/10.1016/J.EXPNEUROL.2012.01.014

Hu, C., Hill, D. D., & Wong, K. Y. (2013). Intrinsic physiological properties of the five types of mouse ganglion-cell photoreceptors. *Journal of Neurophysiology*, *109*(7), 1876–1889. https://doi.org/10.1152/jn.00579.2012

Hughes, S., Watson, T. S., Foster, R. G., Peirson, S. N., & Hankins, M. W. (2013). Nonuniform Distribution and Spectral Tuning of Photosensitive Retinal Ganglion Cells of the Mouse Retina. *Current Biology*, *23*(17), 1696–1701. https://doi.org/10.1016/J.CUB.2013.07.010

Ito, K., & Enomoto, H. (2016). Retrograde transport of neurotrophic factor signaling: implications in neuronal development and pathogenesis. *Journal of Biochemistry*, *160*(2), 77–85. https://doi.org/10.1093/JB/MVW037

Jain, V., Ravindran, E., & Dhingra, N. K. (2012). Differential expression of Brn3 transcription factors in intrinsically photosensitive retinal ganglion cells in mouse. *Journal of Comparative Neurology*, *520*(4), 742–755. https://doi.org/10.1002/CNE.22765

Jampel, H. D., Friedman, D., Quigley, H., Vitale, S., Miller, R., Knezevich, F., & Ding, Y. (2009). Agreement among glaucoma specialists in assessing progressive disc changes from photographs in open-angle glaucoma patients. *American Journal of Ophthalmology*, *147*(1), 39–44. https://doi.org/10.1016/J.AJO.2008.07.023

Jasien, J. V., Samuels, B. C., Johnston, J. M., & Downs, J. C. (2020). Diurnal Cycle of Translaminar Pressure in Nonhuman Primates Quantified With Continuous Wireless Telemetry. *Investigative Ophthalmology & Visual Science*, *61*(2), 37. https://doi.org/10.1167/IOVS.61.2.37

Jeon, C.-J., Strettoi, E., & Masland, R. H. (1998). The Major Cell Populations of the Mouse Retina. *The Journal of Neuroscience*, *18*(21), 8936–8946. https://doi.org/10.1523/jneurosci.18-21-08936.1998

Jiang, S., Kametani, M., & Chen, D. F. (2020). Adaptive Immunity: New Aspects of Pathogenesis

Underlying Neurodegeneration in Glaucoma and Optic Neuropathy. *Frontiers in Immunology*, *11*, 65. https://doi.org/10.3389/fimmu.2020.00065

Johnson, E. C., Guo, Y., Cepurna, W. O., & Morrison, J. C. (2009). NEUROTROPHIN ROLES IN RETINAL GANGLION CELL SURVIVAL: LESSONS FROM RAT GLAUCOMA MODELS. *Experimental Eye Research*, *88*(4), 808–815. https://doi.org/10.1016/J.EXER.2009.02.004

Johnson, E. N., Westbrook, T., Shayesteh, R., Chen, E. L., Schumacher, J. W., Fitzpatrick, D., & Field, G. D. (2019). Distribution and diversity of intrinsically photosensitive retinal ganglion cells in tree shrew. *Journal of Comparative Neurology*, *527*(1), 328–344. https://doi.org/10.1016/j.physbeh.2017.03.040

Jones, J. R., Tackenberg, M. C., & Mcmahon, D. G. (2015). Manipulating circadian clock neuron firing rate resets molecular circadian rhythms and behavior. *Nature Neuroscience*, *18*(3), 373–377. https://doi.org/10.1038/nn.3937

Joo, H. R., Peterson, B. B., Dacey, D. M., Hattar, S., & Chen, S. K. (2013). Recurrent axon collaterals of intrinsically photosensitive retinal ganglion cells. *Visual Neuroscience*, *30*(4), 175–182. https://doi.org/10.1017/S0952523813000199

Kalesnykas, G., Oglesby, E. N., Zack, D. J., Cone, F. E., Steinhart, M. R., Tian, J., Pease, M. E., & Quigley, H. A. (2012). Retinal Ganglion Cell Morphology after Optic Nerve Crush and Experimental Glaucoma. *Investigative Ophthalmology & Visual Science*, *53*(7), 3847–3857. https://doi.org/10.1167/IOVS.12-9712

Kankipati, L., Girkin, C. A., & Gamlin, P. D. (2011). The Post-Illumination Pupil Response Is Reduced in Glaucoma Patients. *Investigative Ophthalmology & Visual Science*, *52*(5), 2287–2292. https://doi.org/10.1167/IOVS.10-6023

Kawasaki, A., Collomb, S., Léon, L., & Münch, M. (2014). Pupil responses derived from outer and inner retinal photoreception are normal in patients with hereditary optic neuropathy. *Experimental Eye Research*, *120*, 161–166. https://doi.org/10.1016/J.EXER.2013.11.005

Kelbsch, C., Maeda, F., Strasser, T., Blumenstock, G., Wilhelm, B., Wilhelm, H., & Peters, T. (2016). Pupillary responses driven by ipRGCs and classical photoreceptors are impaired in glaucoma. *Graefe's Archive for Clinical and Experimental Ophthalmology*, *254*(7), 1361–1370. https://doi.org/10.1007/S00417-016-3351-9/FIGURES/6

Kerrigan-Baumrind, L. A., Quigley, H. A., Pease, M. E., Kerrigan, D. F., & Mitchell, R. S. (2000). Number of ganglion cells in glaucoma eyes compared with threshold visual field tests in the same persons. *Investigative Ophthalmology and Visual Science*, *41*(3), 741–748.

Kerschensteiner, M., Schwab, M. E., Lichtman, J. W., & Misgeld, T. (2005). In vivo imaging of axonal degeneration and regeneration in the injured spinal cord. *Nature Medicine*, *11*(5), 572–577. https://doi.org/10.1038/nm1229

Khani, M. H., & Gollisch, T. (2017). Diversity in spatial scope of contrast adaptation among mouse retinal ganglion cells. *Journal of Neurophysiology*, *118*(6), 3024–3043. https://doi.org/10.1152/JN.00529.2017

Killer, H. E., & Pircher, • A. (2018). Normal tension glaucoma: review of current understanding and mechanisms of the pathogenesis. *Eye*, *32*, 924–930. https://doi.org/10.1038/s41433-018-0042-2

Kiriyama, N., Ando, Ak., Fukui, C., Nambu, H., Nishikawa, M., Terauchi, H., Kuwahara, A., & Matsumura, M. (2003). A comparison of optic disc topographic parameters in patients with primary open angle glaucoma, normal tension glaucoma, and other hypertension. *Graefe's Archive for Clinical and Experimental Ophthalmology*, *241*(7), 541–545. https://doi.org/10.1007/S00417-003-0702-0/FIGURES/1

Kuze, M., Morita, T., Fukuda, Y., Kondo, M., Tsubota, K., & Ayaki, M. (2017). Electrophysiological responses from intrinsically photosensitive retinal ganglion cells are diminished in glaucoma patients. *Journal of Optometry*, *10*(4), 226–231. https://doi.org/10.1016/J.OPTOM.2016.07.004

Kwon, H. S., & Koh, S. H. (2020). Neuroinflammation in neurodegenerative disorders: the roles of microglia and astrocytes. *Translational Neurodegeneration*, *9*(1), 42.

https://doi.org/10.1186/S40035-020-00221-2

La Morgia, C., Ross-Cisneros, F. N., Sadun, A. A., Hannibal, J., Munarini, A., Mantovani, V., Barboni, P., Cantalupo, G., Tozer, K. R., Sancisi, E., Salomao, S. R., Moraes, M. N., Moraes-Filho, M. N., Heegaard, S., Milea, D., Kjer, P., Montagna, P., & Carelli, V. (2010). Melanopsin retinal ganglion cells are resistant to neurodegeneration in mitochondrial optic neuropathies. *Brain*, *133*(8), 2426–2438. https://doi.org/10.1093/BRAIN/AWQ155

Lambiase, A., Aloe, L., Centofanti, M., Parisi, V., Mantelli, F., Colafrancesco, V., Manni, G. L., Bucci, M. G., Bonini, S., & Levi-Montalcini, R. (2009). Experimental and clinical evidence of neuroprotection by nerve growth factor eye drops: Implications for glaucoma. *Proceedings of the National Academy of Sciences of the United States of America*, *106*(32), 13469–13474. https://doi.org/10.1073/PNAS.0906678106

Lanzani, M. F., De Zavalía, N., Fontana, H., Sarmiento, M. I. K., Golombek, D., & Rosenstein, R. E. (2012). Alterations of locomotor activity rhythm and sleep parameters in patients with advanced glaucoma. *Chronobiology International*, *29*(7), 911–919. https://doi.org/10.3109/07420528.2012.691146

Levin, L. A. (2001). Relevance of the site of injury of glaucoma to neuroprotective strategies. *Survey of Ophthalmology*, *45*, S243-249. https://doi.org/10.1016/S0039-6257(01)00197-7

Levkovitch-Verbin, H. (2015). Retinal ganglion cell apoptotic pathway in glaucoma: Initiating and downstream mechanisms. *Progress in Brain Research*, *220*, 37–57. https://doi.org/10.1016/BS.PBR.2015.05.005

Li, L., Huang, H., Fang, F., Liu, L., Sun, Y., & Hu, Y. (2020). Longitudinal Morphological and Functional Assessment of RGC Neurodegeneration After Optic Nerve Crush in Mouse. *Frontiers in Cellular Neuroscience*, *14*, 109. https://doi.org/10.3389/FNCEL.2020.00109/BIBTEX

Li, R. S., Chen, B. Y., Tay, D. K., Chan, H. H. L., Pu, M. L., & So, K. F. (2006). Melanopsin-expressing retinal ganglion cells are more injury-resistant in a chronic ocular hypertension model. *Investigative Ophthalmology and Visual Science*, *47*(7), 2951–2958. https://doi.org/10.1167/iovs.05-1295

Li, S., Yang, C., Zhang, L., Gao, X., Wang, X., Liu, W., Wang, Y., Jiang, S., Wong, Y. H., Zhang, Y., & Liu, K. (2016). Promoting axon regeneration in the adult CNS by modulation of the melanopsin/GPCR signaling. *Proceedings of the National Academy of Sciences of the United States of America*, *113*(7), 1937–1942. https://doi.org/10.1073/PNAS.1523645113/SUPPL_FILE/PNAS.201523645SI.PDF

Li, X., Tham, Y.-C., Cheng, C.-Y., Quigley, H. A., Aung, T., & Wong, T. Y. (2014). Global Prevalence of Glaucoma and Projections of Glaucoma Burden through 2040. *Ophthalmology*, *121*(11), 2081–2090. https://doi.org/10.1016/j.ophtha.2014.05.013

Liao, H. W., Ren, X., Peterson, B. B., Marshak, D. W., Yau, K. W., Gamlin, P. D., & Dacey, D. M. (2016). Melanopsin-expressing ganglion cells on macaque and human retinas form two morphologically distinct populations. *The Journal of Comparative Neurology*, *524*(14), 2845–2872. https://doi.org/10.1002/CNE.23995

Libby, R. T., Li, Y., Savinova, O. V., Barter, J., Smith, R. S., Nickells, R. W., & John, S. W. M. (2005). Susceptibility to neurodegeneration in a glaucoma is modified by Bax gene dosage. *PLoS Genetics*, *1*(1), 0017–0026. https://doi.org/10.1371/JOURNAL.PGEN.0010004

Lorenzana, A. O., Lee, J. K., Mui, M., Chang, A., & Zheng, B. (2015). A Surviving Intact Branch Stabilizes Remaining Axon Architecture after Injury as Revealed by In Vivo Imaging in the Mouse Spinal Cord. *Neuron*, *86*(4), 947–954. https://doi.org/10.1016/J.NEURON.2015.03.061

Lucas, R. J., Allen, A. E., Milosavljevic, N., Storchi, R., & Woelders, T. (2020). Can We See with Melanopsin? *Annual Review of Vision Science*, *15*(6), 453–468. https://doi.org/10.1146/annurev-vision-030320

Lucas, R. J., Hattar, S., Takao, M., Berson, D. M., Foster, R. G., & Yau, K. W. (2003). Diminished pupillary light reflex at high irradiances in melanopsin-knockout mice. *Science*, *299*(5604), 245–247. https://doi.org/10.1126/SCIENCE.1077293/SUPPL_FILE/LUCAS.SOM.PDF.PDF

Luo, C., Yang, X., Kain, A. D., Powell, D. W., Kuehn, M. H., & Tezel, G. (2010). Glaucomatous tissue stress and the regulation of immune response through glial toll-like receptor signaling. *Investigative Ophthalmology and Visual Science*, *51*(11), 5697–5707. https://doi.org/10.1167/iovs.10-5407

Ma, X. P., Shen, M. Y., Shen, G. L., Qi, Q. R., & Sun, X. H. (2018). Melatonin concentrations in serum of primary glaucoma patients. *International Journal of Ophthalmology*, *11*(8), 1337–1341. https://doi.org/10.18240/IJO.2018.08.14

Maeda, A., Tsujiya, S., Higashide, T., Toida, K., Todo, T., Ueyama, T., Okamura, H., & Sugiyama, K. (2006). Circadian intraocular pressure rhythm is generated by clock genes. *Investigative Ophthalmology and Visual Science*, *47*(9), 4050–4052. https://doi.org/10.1167/iovs.06-0183

Manthey, A. L., Liu, W., Jiang, Z. X., Kong Lee, M. H., Ji, J., So, K. F., Ming Lai, J. S., Hong Lee, V. W., & Chiu, K. (2017). Using Electrical Stimulation to Enhance the Efficacy of Cell Transplantation Therapies for Neurodegenerative Retinal Diseases: Concepts, Challenges, and Future Perspectives. *Cell Transplantation*, *26*(6), 949–965. https://doi.org/10.3727/096368917X694877

Maruani, J., & Geoffroy, P. A. (2022). Multi-Level Processes and Retina–Brain Pathways of Photic Regulation of Mood. *Journal of Clinical Medicine*, *11*(2), 448. https://doi.org/10.3390/JCM11020448

McKinnon, S. J., Schlamp, C. L., & Nickells, R. W. (2009). Mouse models of retinal ganglion cell death and glaucoma. *Experimental Eye Research*, *88*(4), 816–824. https://doi.org/10.1016/j.exer.2008.12.002

Mélik Parsadaniantz, S., Réaux-le Goazigo, A., Sapienza, A., Habas, C., & Baudouin, C. (2020). Glaucoma: A Degenerative Optic Neuropathy Related to Neuroinflammation? *Cells*, *9*(3), 535. https://doi.org/10.3390/cells9030535

Miller, D. A., Grannonico, M., Liu, M., Kuranov, R. V., Netland, P. A., Liu, X., & Zhang, H. F. (2020). Visible-Light Optical Coherence Tomography Fibergraphy for Quantitative Imaging of Retinal Ganglion Cell Axon Bundles. *Translational Vision Science & Technology*, *9*(11), 11. https://doi.org/10.1167/TVST.9.11.11

Minckler, D. S., McLean, I. W., & Tso, M. O. M. (1976). Distribution of Axonal And Glial Elements in the Rhesus Optic Nerve Head Studied by Electron Microscopy. *American Journal of Ophthalmology*, *82*(2), 179–187. https://doi.org/10.1016/0002-9394(76)90416-5

Morgia, C. La, di Vito, L., Carelli, V., & Carbonelli, M. (2017). Patterns of Retinal Ganglion Cell Damage in Neurodegenerative Disorders: Parvocellular vs Magnocellular Degeneration in Optical Coherence Tomography Studies. *Frontiers in Neurology*, *8*, 710. https://doi.org/10.3389/FNEUR.2017.00710

Morin, L. P. (2013). Neuroanatomy of the Extended Circadian Rhythm System. *Experimental Neurology*, *243*, 4–20. https://doi.org/10.1016/J.EXPNEUROL.2012.06.026

Morin, L. P., & Studholme, K. M. (2014). Retinofugal Projections in the Mouse Lawrence. *Journal of Comparative Neurology*, *522*(16), 3733–3753. https://doi.org/10.1158/0008-5472.CAN-10-4002.BONE

Mure, L. S., Vinberg, F., Hanneken, A., & Panda, S. (2019). Functional diversity of human intrinsically photosensitive retinal ganglion cells. *Science*, *366*(6470), 1251–1255. https://doi.org/10.1126/science.aaz0898

Mwanza, J. C., Kim, H. Y., Budenz, D. L., Warren, J. L., Margolis, M., Lawrence, S. D., Jani, P. D., Thompson, G. S., & Lee, R. K. (2015). Residual and Dynamic Range of Retinal Nerve Fiber Layer Thickness in Glaucoma: Comparison of Three OCT Platforms. *Investigative Ophthalmology & Visual Science*, *56*(11), 6344–6351. https://doi.org/10.1167/IOVS.15-17248

Nadal-Nicolás, F. M., Madeira, M. H., Salinas-Navarro, M., Jiménez-López, M., Galindo-Romero, C., Ortín-Martínez, A., Santiago, A. R., Vidal-Sanz, M., & Agudo-Barriuso, M. (2015). Transient Downregulation of Melanopsin Expression After Retrograde Tracing or Optic Nerve Injury in Adult Rats. *Investigative Ophthalmology & Visual Science*, *56*(8), 4309–4323. https://doi.org/10.1167/IOVS.15-16963

Nasir-Ahmad, S., Lee, S. C. S., Martin, P. R., & Grünert, U. (2019). Melanopsin-expressing ganglion cells in human retina: Morphology, distribution, and synaptic connections. *Journal of Comparative Neurology*, *527*(1), 312–327. https://doi.org/10.1002/CNE.24176

Naskar, R., Vorwerk, C. K., & Dreyer, E. B. (2000). Concurrent downregulation of a glutamate transporter and receptor in glaucoma. *Investigative Ophthalmology and Visual Science*, *41*(7), 1940–1944.

Nissen, C., Sander, B., Milea, D., Kolko, M., Herbst, K., Hamard, P., & Lund-Andersen, H. (2014). Monochromatic pupillometry in unilateral glaucoma discloses no adaptive changes subserved by the ipRGCs. *Frontiers in Neurology*, *5*, 15. https://doi.org/10.3389/FNEUR.2014.00015/BIBTEX

Obara, E. A., Hannibal, J., Heegaard, S., & Fahrenkrug, J. (2016). Loss of Melanopsin-Expressing Retinal Ganglion Cells in Severely Staged Glaucoma Patients. *Investigative Ophthalmology & Visual Science*, *57*(11), 4661–4667. https://doi.org/10.1167/IOVS.16-19997

Osborne, N. N. (2009). Recent clinical findings with memantine should not mean that the idea of neuroprotection in glaucoma is abandoned. *Acta Ophthalmologica*, *87*(4), 450–454. https://doi.org/10.1111/J.1755-3768.2008.01459.X

Ou, Y., Jo, R. E., Ullian, E. M., Wong, R. O. L., & Della Santina, L. (2016). Selective Vulnerability of Specific Retinal Ganglion Cell Types and Synapses after Transient Ocular Hypertension. *The Journal of Neuroscience*, *36*(35), 9240–9252. https://doi.org/10.1523/JNEUROSCI.0940-16.2016

Panda, S., Provencio, I., Tu, D. C., Pires, S. S., Rollag, M. D., Castrucci, A. M., Pletcher, M. T., Sato, T. K., Wiltshire, T., Andahazy, M., Kay, S. A., Van Gelder, R. N., & Hogenesch, J. B. (2003). Melanopsin is required for non-image-forming photic responses in blind mice. *Science*, *301*(5632), 525–527. https://doi.org/10.1126/SCIENCE.1086179/SUPPL_FILE/PANDA.SOM.PDF

Panda, S., Sato, T. K., Castrucci, A. M., Rollag, M. D., DeGrip, W. J., Hogenesch, J. B., Provencio, I., & Kay, S. A. (2002). Melanopsin (Opn4) requirement for normal light-induced circadian phase shifting. *Science*, *298*, 2213–2216. https://doi.org/10.1126/science.1076848

Paul, K. N., Saafir, T. B., & Tosini, G. (2009). The role of retinal photoreceptors in the regulation of circadian rhythms. *Reviews in Endocrine and Metabolic Disorders*, *10*(4), 271–278. https://doi.org/10.1007/s11154-009-9120-x

Pérez-Rico, C., de la Villa, P., Arribas-Gómez, I., & Blanco, R. (2010). Evaluation of functional integrity of the retinohypothalamic tract in advanced glaucoma using multifocal electroretinography and light-induced melatonin suppression. *Experimental Eye Research*, *91*(5), 578–583. https://doi.org/10.1016/J.EXER.2010.07.012

Pfeiffer, R. L., Marc, R. E., & Jones, B. W. (2020). Müller Cell Metabolic Signatures: Evolutionary Conservation and Disruption in Disease. *Trends in Endocrinology and Metabolism*, *31*(4), 320–329. https://doi.org/10.1016/j.tem.2020.01.005

Provencio, I., Jiang, G., De Grip, W. J., Pär Hayes, W., & Rollag, M. D. (1998). Melanopsin: An opsin in melanophores, brain, and eye. *Proceedings of the National Academy of Sciences of the United States of America*, *95*(1), 340–345. https://doi.org/10.1073/PNAS.95.1.340

Provencio, I., Rodriguez, I. R., Jiang, G., Hayes, W. P., Moreira, E. F., & Rollag, M. D. (2000). A Novel Human Opsin in the Inner Retina. *Journal of Neuroscience*, *20*(2), 600–605. https://doi.org/10.1523/JNEUROSCI.20-02-00600.2000

Provencio, I., Rollag, M. D., & Castrucci, A. M. (2002). Photoreceptive net in the mammalian retina. *Nature*, *415*, 493–494. https://doi.org/10.1038/415493a

Prusky, G. T., Alam, N. M., Beekman, S., & Douglas, R. M. (2004). Rapid quantification of adult and developing mouse spatial vision using a virtual optomotor system. *Investigative Ophthalmology and Visual Science*, *45*(12), 4611–4616. https://doi.org/10.1167/iovs.04-0541

Puyang, Z., Chen, H., & Liu, X. (2015). Subtype-dependent Morphological and Functional Degeneration of Retinal Ganglion Cells in Mouse Models of Experimental Glaucoma. *Journal of Nature and Science*, *1*(5), e103. https://doi.org/10.3791/50440.14.

Puyang, Z., Feng, L., Chen, H., Liang, P., Troy, J. B., & Liu, X. (2016). Retinal Ganglion Cell Loss is Delayed Following Optic Nerve Crush in NLRP3 Knockout Mice. *Scientific Reports*, *6*, 20998.

https://doi.org/10.1038/SREP20998

Quaranta, L., Riva, I., Gerardi, C., Oddone, F., Floriano, I., & Konstas, A. G. P. (2016). Quality of Life in Glaucoma: A Review of the Literature. *Advances in Therapy*, *33*(6), 959–981. https://doi.org/10.1007/S12325-016-0333-6

Quattrochi, L. E., Stabio, M. E., Kim, I., Ilardi, M. C., Fogerson, P. M., Leyrer, M. L., & Berson, D. M. (2019). The M6 cell: A small-field bistratified photosensitive retinal ganglion cell. *Journal of Comparative Neurology*, *527*(1), 297–311. https://doi.org/110.1002/cne.24556

Quigley, H. A. (2016). Understanding Glaucomatous Optic Neuropathy: The Synergy Between Clinical Observation and Investigation. *Annual Review of Vision Science*, *2*, 235–254. https://doi.org/10.1146/annurev-vision-111815-114417

Quigley, H. A., Addicks, E. M., Green, W. R., & Maumenee, A. E. (1981). Optic Nerve Damage in Human Glaucoma: II. The Site of Injury and Susceptibility to Damage. *Archives of Ophthalmology*, *99*(4), 635–649. https://doi.org/10.1001/ARCHOPHT.1981.03930010635009

Quigley, H. A., Dunkelberger, G. R., & Green, W. R. (1988). Chronic human glaucoma causing selectively greater loss of large optic nerve fibers. *Ophthalmology*, *95*(3), 357–363.

Quigley, H. A., McKinnon, S. J., Zack, D. J., Pease, M. E., Kerrigan-Baumrind, L. A., Kerrigan, D. F., & Mitchell, R. S. (2000). Retrograde axonal transport of BDNF in retinal ganglion cells is blocked by acute IOP elevation in rats. *Investigative Ophthalmology and Visual Science*, *41*(11), 3460–3466.

Quigley, H., & Broman, A. T. (2006). The number of people with glaucoma worldwide in 2010 and 2020. *British Journal of Ophthalmology*, *90*(3), 262–267. https://doi.org/10.1136/BJO.2005.081224

Ramírez, A. I., Salazar, J. J., de Hoz, R., Rojas, B., Gallego, B. I., Salinas-Navarro, M., Alarcón-Martínez, L., Ortín-Martínez, A., Avilés-Trigueros, M., Vidal-Sanz, M., Triviño, A., & Ramírez, J. M. (2010). Quantification of the Effect of Different Levels of IOP in the Astroglia of the Rat Retina Ipsilateral and Contralateral to Experimental Glaucoma. *Investigative Ophthalmology & Visual Science*, *51*(11), 5690–5696. https://doi.org/10.1167/IOVS.10-5248

Rangarajan, K. V., Lawhn-Heath, C., Feng, L., Kim, T. S., Cang, J., & Liu, X. (2011). Detection of visual deficits in aging DBA/2J mice by two behavioral assays. *Current Eye Research*, *36*(5), 481–491. https://doi.org/10.3109/02713683.2010.549600

Rashid, K., Akhtar-Schaefer, I., & Langmann, T. (2019). Microglia in retinal degeneration. *Frontiers in Immunology*, *10*, 1975. https://doi.org/10.3389/fimmu.2019.01975

Robinson, G. A., & Madison, R. D. (2004). Axotomized mouse retinal ganglion cells containing melanopsin show enhanced survival, but not enhanced axon regrowth into a peripheral nerve graft. *Vision Research*, *44*(23), 2667–2674. https://doi.org/10.1016/J.VISRES.2004.06.010

Rodriguez, A. R., de Sevilla Müller, L. P., & Brecha, N. C. (2014). The RNA binding protein RBPMS is a selective marker of ganglion cells in the mammalian retina. *The Journal of Comparative Neurology*, *522*(6), 1411–1443. https://doi.org/10.1002/CNE.23521

Rojas, B., Gallego, B. I., Ramírez, A. I., Salazar, J. J., de Hoz, R., Valiente-Soriano, F. J., Avilés-Trigueros, M., Villegas-Perez, M. P., Vidal-Sanz, M., Triviño, A., & Ramírez, J. M. (2014). Microglia in mouse retina contralateral to experimental glaucoma exhibit multiple signs of activation in all retinal layers. *Journal of Neuroinflammation*, *11*(1), 133. https://doi.org/10.1186/1742-2094-11-133

Rovere, G., Nadal-Nicolás, F. M., Agudo-Barriuso, M., Sobrado-Calvo, P., Nieto-López, L., Nucci, C., Villegas-Pérez, M. P., & Vidal-Sanz, M. (2015). Comparison of Retinal Nerve Fiber Layer Thinning and Retinal Ganglion Cell Loss After Optic Nerve Transection in Adult Albino Rats. *Investigative Ophthalmology & Visual Science*, *56*(8), 4487–4498. https://doi.org/10.1167/IOVS.15-17145

Ruby, N. F., Brennan, T. J., Xie, X., Cao, V., Franken, P., Heller, H. C., & O'Hara, B. F. (2002). Role of melanopsin in circadian responses to light. *Science*, *298*(5601), 2211–2213. https://doi.org/10.1126/SCIENCE.1076701/SUPPL_FILE/RUBY.SOM.PDF

Rüger, M., Gordijn, M. C. M., Beersma, D. G. M., de Vries, B., & Daan, S. (2005). Nasal versus temporal illumination of the human retina: effects on core body temperature, melatonin, and circadian phase.

Journal of Biological Rhythms, *20*(1), 60–70. https://doi.org/10.1177/0748730404270539

Rupp, A. C., Ren, M., Altimus, C. M., Fernandez, D. C., Richardson, M., Turek, F., Hattar, S., & Schmidt, T. M. (2019). Distinct ipRGC subpopulations mediate light's acute and circadian effects on body temperature and sleep. *ELife*, *8*, e44358. https://doi.org/10.7554/ELIFE.44358

Ruzafa, N., Pereiro, X., & Vecino, E. (2022). Immunohistochemical Characterisation of the Whale Retina. *Frontiers in Neuroanatomy*, *16*, 813369. https://doi.org/10.3389/FNANA.2022.813369/FULL

Samuels, B. C., Siegwart, J. T., Zhan, W., Hethcox, L., Chimento, M., Whitley, R., Downs, J. C., & Girkin, C. A. (2018). A Novel Tree Shrew (Tupaia belangeri) Model of Glaucoma. *Investigative Ophthalmology & Visual Science*, *59*(7), 3136–3143. https://doi.org/10.1167/IOVS.18-24261

Sánchez-Migallón, M. C., Valiente-Soriano, F. J., Salinas-Navarro, M., Nadal-Nicolás, F. M., Jiménez-López, M., Vidal-Sanz, M., & Agudo-Barriuso, M. (2018a). Nerve fibre layer degeneration and retinal ganglion cell loss long term after optic nerve crush or transection in adult mice. *Experimental Eye Research*, *170*, 40–50. https://doi.org/10.1016/j.exer.2018.02.010

Sánchez-Migallón, M. C., Valiente-Soriano, F. J., Salinas-Navarro, M., Nadal-Nicolás, F. M., Jiménez-López, M., Vidal-Sanz, M., & Agudo-Barriuso, M. (2018b). Nerve fibre layer degeneration and retinal ganglion cell loss long term after optic nerve crush or transection in adult mice. *Experimental Eye Research*, *170*, 40–50. https://doi.org/10.1016/J.EXER.2018.02.010

Sanes, J. R., & Masland, R. H. (2015). The Types of Retinal Ganglion Cells: Current Status and Implications for Neuronal Classification. *Annual Review of Neuroscience*, *38*, 221–246. https://doi.org/10.1146/annurev-neuro-071714-034120

Sappington, R. M., Carlson, B. J., Crish, S. D., & Calkins, D. J. (2010). The Microbead Occlusion Model: A Paradigm for Induced Ocular Hypertension in Rats and Mice. *Investigative Ophthalmology & Visual Science*, *51*(1), 207–216. https://doi.org/10.1167/IOVS.09-3947

Sato, T., Fujikado, T., Lee, T. S., & Tano, Y. (2008). Direct Effect of Electrical Stimulation on Induction of Brain-Derived Neurotrophic Factor from Cultured Retinal Müller Cells. *Investigative Ophthalmology & Visual Science*, *49*(10), 4641–4646. https://doi.org/10.1167/IOVS.08-2049

Schmidt, T. M., Alam, N. M., Chen, S., Kofuji, P., Li, W., Prusky, G. T., & Hattar, S. (2014). A role for melanopsin in alpha retinal ganglion cells and contrast detection. *Neuron*, *82*, 781–788. https://doi.org/10.1016/j.neuron.2014.03.022

Schmidt, T. M., Do, M. T. H., Dacey, D. M., Lucas, R. J., Hattar, S., & Matynia, A. (2011). Melanopsin-positive intrinsically photosensitive retinal ganglion cells : From Form To Function. *Journal of Neuroscience*, *31*(45), 16094–16101. https://doi.org/10.1523/JNEUROSCI.4132-11.2011.MELANOPSIN-POSITIVE

Schuman, J. S., Kostanyan, T., & Bussel, I. (2020). Review of Longitudinal Glaucoma Progression: 5 Years after the Shaffer Lecture. *Ophthalmology. Glaucoma*, *3*(2), 158–166. https://doi.org/10.1016/J.OGLA.2019.11.012

Segal, R. A. (2003). SELECTIVITY IN NEUROTROPHIN SIGNALING: Theme and Variations. *Annual Review of Neuroscience*, *26*, 299–330. https://doi.org/10.1146/ANNUREV.NEURO.26.041002.131421

Semo, M., Gias, C., Ahmado, A., & Vugler, A. (2014). A role for the ciliary marginal zone in the melanopsin-dependent intrinsic pupillary light reflex. *Experimental Eye Research*, *119*, 8–18. https://doi.org/10.1016/j.exer.2013.11.013

Shin, J. W., Sung, K. R., Lee, G. C., Durbin, M. K., & Cheng, D. (2017). Ganglion Cell–Inner Plexiform Layer Change Detected by Optical Coherence Tomography Indicates Progression in Advanced Glaucoma. *Ophthalmology*, *124*(10), 1466–1474. https://doi.org/10.1016/J.OPHTHA.2017.04.023

Shu, X., Beckmann, L., & Zhang, H. F. (2017). Visible-light optical coherence tomography: a review. *Journal of Biomedical Optics*, *22*(12), 121707. https://doi.org/10.1117/1.JBO.22.12.121707

Siaudvytyte, L., Januleviciene, I., Daveckaite, A., Ragauskas, A., Siesky, B., & Harris, A. (2016). Neuroretinal rim area and ocular haemodynamic parameters in patients with normal-tension glaucoma with differing intracranial pressures. *The British Journal of Ophthalmology*, *100*(8), 1134–1138. https://doi.org/10.1136/BJOPHTHALMOL-2015-307570

Smith, C. A., Vianna, J. R., & Chauhan, B. C. (2017). Assessing retinal ganglion cell damage. *Eye*, *31*(2), 209–217. https://doi.org/10.1038/eye.2016.295

Snyder, P. J., Alber, J., Alt, C., Bain, L. J., Bouma, B. E., Bouwman, F. H., DeBuc, D. C., Campbell, M. C. W., Carrillo, M. C., Chew, E. Y., Cordeiro, M. F., Dueñas, M. R., Fernández, B. M., Koronyo-Hamaoui, M., La Morgia, C., Carare, R. O., Sadda, S. R., van Wijngaarden, P., & Snyder, H. M. (2021). Retinal imaging in Alzheimer's and neurodegenerative diseases. *Alzheimer's & Dementia*, *17*(1), 103–111. https://doi.org/10.1002/ALZ.12179

Sobrado-Calvo, P., Vidal-Sanz, M., & Villegas-Pérez, M. P. (2007). Rat retinal microglial cells under normal conditions, after optic nerve section, and after optic nerve section and intravitreal injection of trophic factors or macrophage inhibitory factor. *Journal of Comparative Neurology*, *501*(6), 866–878. https://doi.org/10.1002/CNE.21279

Somasundaram, P., Wyrick, G. R., Carlos Fernandez, D., Ghahari, A., Pinhal, C. M., Richardson, M. S., Rupp, A. C., Cui, L., Wu, Z., Brown, R. L., Constantin Badea, T., Hattar, S., & Robinson, P. R. (2017). C-terminal phosphorylation regulates the kinetics of a subset of melanopsin-mediated behaviors in mice. *Proceedings of the National Academy of Sciences*, *114*(10), 2741–2746 NEUROSCIENCE. https://doi.org/10.1073/pnas.1611893114

Son, J. L., Soto, I., Oglesby, E., Lopez-Roca, T., Pease, M. E., Quigley, H. A., & Marsh-Armstrong, N. (2010). Glaucomatous optic nerve injury involves early astrocyte reactivity and late oligodendrocyte loss. *Glia*, *58*, 780–789. https://doi.org/10.1002/glia.20962

Sondereker, K. B., Stabio, M. E., & Renna, J. M. (2020). Crosstalk: The diversity of melanopsin ganglion cell types has begun to challenge the canonical divide between image-forming and non-image-forming vision Running. *Journal of Comparative Neurology*, *528*(12), 2044–2067. https://doi.org/10.1002/cne.24873

Sonoda, T., Li, J. Y., Hayes, N. W., Chan, J. C., Okabe, Y., Belin, S., Nawabi, H., & Schmidt, T. M. (2020). A noncanonical inhibitory circuit dampens behavioral sensitivity to light. *Science*, *368*, 527–531. https://doi.org/10.1126/science.aay3152

Sonoda, T., Okabe, Y., & Schmidt, T. M. (2020). Overlapping morphological and functional properties between M4 and M5 intrinsically photosensitive retinal ganglion cells. *Journal of Comparative Neurology*, *528*, 1028–1040. https://doi.org/10.1002/cne.24806

Spitzer, M. H., & Nolan, G. P. (2016). Mass Cytometry: Single Cells, Many Features. *Cell*, *165*(4), 780–791. https://doi.org/10.1016/J.CELL.2016.04.019

Stabio, M. E., Sabbah, S., Quattrochi, L. E., Ilardi, M. C., Fogerson, P. M., Leyrer, M. L., Kim, M. T., Kim, I., Schiel, M., Renna, J. M., Briggman, K. L., & Berson, D. M. (2018). The M5 Cell: A Color-Opponent Intrinsically Photosensitive Retinal Ganglion Cell. *Neuron*, *97*(1), 150–163. https://doi.org/10.1016/j.neuron.2017.11.030

Stassart, R. M., Möbius, W., Nave, K. A., & Edgar, J. M. (2018). The Axon-Myelin unit in development and degenerative disease. *Frontiers in Neuroscience*, *12*, 467. https://doi.org/10.3389/FNINS.2018.00467/BIBTEX

Stein, J. D., Khawaja, A. P., & Weizer, J. S. (2021). Glaucoma in Adults—Screening, Diagnosis, and Management: A Review. *JAMA*, *325*(2), 164–174. https://doi.org/10.1001/JAMA.2020.21899

Stinchcombe, A. R., Hu, C., Walch, O. J., Faught, S. D., Wong, K. Y., & Forger, D. B. (2021). M1-Type, but Not M4-Type, Melanopsin Ganglion Cells Are Physiologically Tuned to the Central Circadian Clock. *Frontiers in Neuroscience*, *15*, 652996. https://doi.org/10.3389/FNINS.2021.652996

Tatham, A. J., & Medeiros, F. A. (2017). Detecting structural progression in glaucoma with optical coherence tomography. *Ophthalmology*, *124*, S57. https://doi.org/10.1016/J.OPHTHA.2017.07.015

Tezel, G., Yang, X., Yang, J., & Wax, M. B. (2004). Role of tumor necrosis factor receptor-1 in the death of retinal ganglion cells following optic nerve crush injury in mice. *Brain Research*, *996*(2), 202–212.

https://doi.org/10.1016/j.brainres.2003.10.029

Thomson, B. R., Grannonico, M., Liu, F., Liu, M., Mendapara, P., Xu, Y., Liu, X., & Quaggin, S. E. (2020). Angiopoietin-1 Knockout Mice as a Genetic Model of Open-Angle Glaucoma. *Translational Vision Science & Technology*, *9*(4), 16. https://doi.org/10.1167/tvst.9.4.16

Tran, N. M., Shekhar, K., Whitney, I. E., Jacobi, A., Benhar, I., Hong, G., Yan, W., Adiconis, X., Arnold, M. E., Lee, J. M., Levin, J. Z., Lin, D., Wang, C., Lieber, C. M., Regev, A., He, Z., & Sanes, J. R. (2019). Single-Cell Profiles of Retinal Ganglion Cells Differing in Resilience to Injury Reveal Neuroprotective Genes. *Neuron*, *104*(6), 1039-1055.e12. https://doi.org/10.1016/j.neuron.2019.11.006

Tsai, J., Grutzendler, J., Duff, K., & Gan, W. B. (2004). Fibrillar amyloid deposition leads to local synaptic abnormalities and breakage of neuronal branches. *Nature Neuroscience*, *7*(11), 1181–1183. https://doi.org/10.1038/nn1335

Vadnie, C. A., & McClung, C. A. (2017). Circadian Rhythm Disturbances in Mood Disorders: Insights into the Role of the Suprachiasmatic Nucleus. *Neural Plasticity*, *2017*, 1504507. https://doi.org/10.1155/2017/1504507

Valiente-Soriano, F. J., García-Ayuso, D., Ortín-Martínez, A., Jiménez-López, M., Galindo-Romero, C., Paz Villegas-Pérez, M., Agudo-Barriuso, M., Vugler, A. A., Vidal-Sanz, M., Li, Y.-Q., Garcia-Fernandez, J. M., Hannibal, J., & Hospital, B. (2014). Distribution of melanopsin positive neurons in pigmented and albino mice: evidence for melanopsin interneurons in the mouse retina. *Frontiers in Neuroanatomy*, *8*, 131. https://doi.org/10.3389/fnana.2014.00131

Valiente-Soriano, F. J., Nadal-Nicolás, F. M., Salinas-Navarro, M., Jiménez-López, M., Bernal-Garro, J. M., Villegas-Pérez, M. P., Agudo-Barriuso, M., & Vidal-Sanz, M. (2015). BDNF Rescues RGCs But Not Intrinsically Photosensitive RGCs in Ocular Hypertensive Albino Rat Retinas. *Investigative Ophthalmology & Visual Science*, *56*(3), 1924–1936. https://doi.org/10.1167/IOVS.15-16454

Valiente-Soriano, F. J., Salinas-Navarro, M., Jiménez-López, M., Alarcón-Martínez, L., Ortín-Martínez, A., Bernal-Garro, J. M., Avilés-Trigueros, M., Agudo-Barriuso, M., Villegas-Pérez, M. P., & Vidal-Sanz, M. (2015). Effects of Ocular Hypertension in the Visual System of Pigmented Mice. *PLOS ONE*, *10*(3), e0121134. https://doi.org/10.1371/JOURNAL.PONE.0121134

Van Der Maaten, L., & Hinton, G. (2008). Visualizing Data using t-SNE. *Journal of Machine Learning Research*, *9*, 2579–2605.

Van Hooser, S. D., Roy, A., Rhodes, H. J., Culp, J. H., & Fitzpatrick, D. (2013). Transformation of Receptive Field Properties from Lateral Geniculate Nucleus to Superficial V1 in the Tree Shrew. *The Journal of Neuroscience*, *33*(28), 11494–11505. https://doi.org/10.1523/JNEUROSCI.1464-13.2013

Vidal-Sanz, M., Galindo-Romero, C., Valiente-Soriano, F. J., Nadal-Nicolás, F. M., Ortin-Martinez, A., Rovere, G., Salinas-Navarro, M., Lucas-Ruiz, F., Sanchez-Migallon, M. C., Sobrado-Calvo, P., Aviles-Trigueros, M., Villegas-Pérez, M. P., & Agudo-Barriuso, M. (2017). Shared and Differential Retinal Responses against Optic Nerve Injury and Ocular Hypertension. *Frontiers in Neuroscience*, *11*, 235. https://doi.org/10.3389/FNINS.2017.00235

Viney, T. J., Balint, K., Hillier, D., Siegert, S., Boldogkoi, Z., Enquist, L. W., Meister, M., Cepko, C. L., & Roska, B. (2007). Local Retinal Circuits of Melanopsin-Containing Ganglion Cells Identified by Transsynaptic Viral Tracing. *Current Biology*, *17*(11), 981–988. https://doi.org/10.1016/j.cub.2007.04.058

Vogel, C., & Marcotte, E. M. (2012). Insights into the regulation of protein abundance from proteomic and transcriptomic analyses. *Nature Reviews Genetics*, *13*(4), 227–232. https://doi.org/10.1038/nrg3185

Voinescu, P. E., Kay, J. N., & Sanes, J. R. (2009). Birthdays of retinal amacrine cell subtypes are systematically related to their molecular identity and soma position. *Journal of Comparative Neurology*, *517*(5), 737. https://doi.org/10.1002/cne.22200.

Vugler, A. A., Semo, A., Joseph, A., & Jeffery, G. (2008). Survival and remodeling of melanopsin cells during retinal dystrophy. *Visual Neuroscience*, *25*, 125–138. https://doi.org/10.1017/S0952523808080309

Wang, H., Deng, Y., Wan, L., & Huang, L. (2020). A comprehensive map of disease networks and molecular drug discoveries for glaucoma. *Scientific Reports*, *10*, 9719. https://doi.org/10.1038/s41598-020-66350-w

Wang, H., Zhang, Y., Ding, J., & Wang, N. (2013). Changes in the Circadian Rhythm in Patients with Primary Glaucoma. *PLoS ONE*, *8*(4), e62841. https://doi.org/10.1371/journal.pone.0062841

Wang, J. T., Medress, Z. A., & Barres, B. A. (2012). Axon degeneration: Molecular mechanisms of a self-destruction pathway. *The Journal of Cell Biology*, *196*(1), 7. https://doi.org/10.1083/JCB.201108111

Wang, Y., Yang, W., Zhang, P., Ding, Z., Wang, L., & Cheng, J. (2022). Effects of light on the sleep-wakefulness cycle of mice mediated by intrinsically photosensitive retinal ganglion cells. *Biochemical and Biophysical Research Communications*, *592*, 93–98. https://doi.org/10.1016/J.BBRC.2022.01.023

Weber, A. J., Viswanáthan, S., Ramanathan, C., & Harman, C. D. (2010). Combined Application of BDNF to the Eye and Brain Enhances Ganglion Cell Survival and Function in the Cat after Optic Nerve Injury. *Investigative Ophthalmology & Visual Science*, *51*(1), 327–334. https://doi.org/10.1167/IOVS.09-3740

Wei, X., Cho, K. S., Thee, E. F., Jager, M. J., & Chen, D. F. (2019). Neuroinflammation and microglia in glaucoma: time for a paradigm shift. *Journal of Neuroscience Research*, *97*(1), 70–76. https://doi.org/10.1002/jnr.24256

Weinreb, R. N., Aung, T., & Medeiros, F. A. (2014). The pathophysiology and treatment of glaucoma: A review. *Journal of the American Medical Association*, *311*(18), 1901–1911. https://doi.org/10.1001/jama.2014.3192

Weinreb, R. N., & Tee Khaw, P. (2004). Primary open-angle glaucoma. *The Lancet*, *363*(9422), 1711–1720. https://doi.org/10.1016/S0140-6736(04)16257-0

Welp, A., RB, W., MA, M., & SM, T. (2016). *Making Eye Health a Population Health Imperative: Vision for Tomorrow*. National Academies Press. https://doi.org/10.17226/23471

Welsh, D. K., Takahashi, J. S., & Kay, S. A. (2010). Suprachiasmatic nucleus: Cell autonomy and network properties. *Annual Review of Physiology*, *72*, 551–577. https://doi.org/10.1146/annurev-physiol-021909-135919

Whitmore, A. V., Libby, R. T., & John, S. W. M. (2005). Glaucoma: Thinking in new ways—a rôle for autonomous axonal self-destruction and other compartmentalised processes? *Progress in Retinal and Eye Research*, *24*(6), 639–662. https://doi.org/10.1016/J.PRETEYERES.2005.04.004

Woldemussie, E., Wijono, M., & Ruiz, G. (2004). Müller cell response to laser-induced increase in intraocular pressure in rats. *Glia*, *47*(2), 109–119. https://doi.org/10.1002/GLIA.20000

Wollstein, G., Garway-Heath, D. F., Fontana, L., & Hitchings, R. A. (2000). Identifying early glaucomatous changes: Comparison between expert clinical assessment of optic disc photographs and confocal scanning ophthalmoscopy. *Ophthalmology*, *107*(12), 2272–2277. https://doi.org/10.1016/S0161-6420(00)00363-8

Wollstein, G., Garway-Heath, D. F., & Hitchings, R. A. (1998). Identification of early glaucoma cases with the scanning laser ophthalmoscope. *Ophthalmology*, *105*(8), 1557–1563. https://doi.org/10.1016/S0161-6420(98)98047-2

Wollstein, G., Kagemann, L., Bilonick, R. A., Ishikawa, H., Folio, L. S., Gabriele, M. L., Ungar, A. K., Duker, J. S., Fujimoto, J. G., & Schuman, J. S. (2012). Retinal nerve fibre layer and visual function loss in glaucoma: the tipping point. *The British Journal of Ophthalmology*, *96*(1), 47–52. https://doi.org/10.1136/BJO.2010.196907

Xiang, M., Zhou, L., Macke, J. P., Yoshioka, T., Hendry, S. H. C., Eddy, R. L., Shows, T. B., & Nathans, J. (1995). The Brn-3 family of POU-domain factors: primary structure, binding specificity, and expression in subsets of retinal ganglion cells and somatosensory neurons. *Journal of Neuroscience*, *15*(7), 4762–4785. https://doi.org/10.1523/JNEUROSCI.15-07-04762.1995

Yang, X., Chou, T.-H., Ruggeri, M., Porciatti, V., & Eye, B. P. (2013). A New Mouse Model of Inducible, Chronic Retinal Ganglion Cell Dysfunction Not Associated with Cell Death. *Investigative Ophthalmology & Visual Science*, *54*(3), 1898–1904. https://doi.org/10.1167/iovs.12-11375

Yang, Z., Quigley, H. A., Pease, M. E., Yang, Y., Qian, J., Valenta, D., & Zack, D. J. (2007). Changes in gene expression in experimental glaucoma and optic nerve transection: The equilibrium between protective and detrimental mechanisms. *Investigative Ophthalmology and Visual Science*, *48*(12), 5539–5548. https://doi.org/10.1167/iovs.07-0542

Yang, Z., Tatham, A. J., Zangwill, L. M., Weinreb, R. N., Zhang, C., & Medeiros, F. A. (2015). Diagnostic ability of retinal nerve fiber layer imaging by swept source optical coherence tomography in glaucoma. *American Journal of Ophthalmology*, *159*(1), 193–201. https://doi.org/10.1016/J.AJO.2014.10.019

Yi, J., Puyang, Z., Feng, L., Duan, L., Liang, P., Backman, V., Liu, X., & Zhang, H. F. (2016). Optical Detection of Early Damage in Retinal Ganglion Cells in a Mouse Model of Partial Optic Nerve Crush Injury. *Investigative Ophthalmology & Visual Science*, *57*(13), 5665–5671. https://doi.org/10.1167/IOVS.16-19955

Yong, Y., Gamage, K., Cheng, I., Barford, K., Spano, A., Winckler, B., & Deppmann, C. (2019). p75NTR and DR6 Regulate Distinct Phases of Axon Degeneration Demarcated by Spheroid Rupture. *The Journal of Neuroscience*, *39*(48), 9503–9520. https://doi.org/10.1523/JNEUROSCI.1867-19.2019

Yoshikawa, T., Obayashi, K., Miyata, K., Saeki, K., & Ogata, N. (2020). Decreased melatonin secretion in patients with glaucoma: quantitative association with glaucoma severity in the LIGHT study. *Journal of Pineal Research*, *69*(2), e12662. https://doi.org/10.1111/jpi.12662

Yuan, X.-S., Wei, H.-H., Xu, W., Wang, L., Qu, W.-M., Li, R.-X., & Huang, Z.-L. (2018). Whole-Brain Monosynaptic Afferent Projections to the Cholecystokinin Neurons of the Suprachiasmatic Nucleus. *Frontiers in Neuroscience*, *12*, 807. https://doi.org/10.3389/fnins.2018.00807

Zhang, Q., Vuong, H., Huang, X., Wang, Y. L., Brecha, N. C., Pu, M. L., & Gao, J. (2013). Melanopsin-expressing retinal ganglion cell loss and behavioral analysis in the Thy1-CFP-DBA/2J mouse model of glaucoma. *Science China. Life Sciences*, *56*(8), 720–730. https://doi.org/10.1007/S11427-013-4493-1

Zhang, Z., Beier, C., Weil, T., & Hattar, S. (2021). The retinal ipRGC-preoptic circuit mediates the acute effect of light on sleep. *Nature Communications*, *12*, 5115. https://doi.org/10.1038/s41467-021-25378-w

Zhao, X., Stafford, B. K., Godin, A. L., King, W. M., Wong, K. Y., & Wong, K. Y. (2014). Photoresponse diversity among the five types of intrinsically photosensitive retinal ganglion cells. *The Journal of Physiology*, *592*(7), 1619–1636. https://doi.org/10.1113/jphysiol.2013.262782

Zhou, X., Sun, F., Xu, S., Yang, G., & Li, M. (2015). The position of tree shrews in the mammalian tree: Comparing multi-gene analyses with phylogenomic results leaves monophyly of Euarchonta doubtful. *Integrative Zoology*, *10*(2), 186–198. https://doi.org/10.1111/1749-4877.12116

Zhou, Y., Davis, A. S., Spitze, A., & Lee, A. G. (2014). Maintenance of pupillary response in a Glaucoma patient with no light perception due to persistence of melanopsin ganglion cells. *Canadian Journal of Ophthalmology/Journal Canadien d'ophtalmologie*, *49*, e20–e21. https://doi.org/10.1016/j.jcjo.2013.10.008

Zunder, E. R., Lujan, E., Goltsev, Y., Wernig, M., & Nolan, G. P. (2015). A Continuous Molecular Roadmap to iPSC Reprogramming through Progression Analysis of Single-Cell Mass Cytometry. *Cell Stem Cell*, *16*(3), 323–337. https://doi.org/10.1016/J.STEM.2015.01.015